Efficient Mid-Infrared Single-Photon Counting Kinetic Inductance Detectors

The Design and Experimental Evaluation of Lens-Absorber Coupled KIDs for 10 and 18.5 Microns

P.C.J.A. van Zweeden

Delft University of Technology

TU Delft

SRON

Efficient Mid-Infrared Single-Photon Counting Kinetic Inductance Detectors

The Design and Experimental Evaluation of Lens-Absorber Coupled KIDs for 10 and 18.5 Microns

by

P.C.J.A. van Zweeden

to obtain the degree of Master of Science in Applied Physics,

at the Delft University of Technology,

to be defended publicly on Thursday May 8, 2025 at 15:45 PM.

Student number:	5134714	
Project duration:	August 26, 2024 – April 18, 2025	
Thesis committee:	Prof. dr. ir. J. J. A. Baselmans ,	TU Delft/SRON, supervisor
	Dr. ir. P. J. de Visser,	TU Delft/SRON, daily supervisor
	Dr. ir. K. Kouwenhoven,	TU Delft/SRON, daily supervisor
	Dr. I. Esmaeil Zadeh	TU Delft

Cover image: A meandering line absorber designed in this thesis, illuminated by an Airy diffraction pattern.

An electronic version of this thesis is available at http://repository.tudelft.nl/.

TU Delft

SRON

Abstract

The search for extraterrestrial life is currently one of the main topics of astronomical research. One of the methods for this is to look for the spectral lines of molecules needed for life, called biosignatures, in the atmosphere. The Large Interferometer for Exoplanets (LIFE) mission will explore the mid-IR in the search for biosignatures. This mission is a spectrometer that uses nulling interferometry to cancel the signal from the nearby star. A spectrometer then splits the remaining planet signal to find biosignatures. The wavelength band of LIFE is 4-$18.5\,\mu\mathrm{m}$. LIFE places a strict requirement on the dark current: $I_D \leq 10^{-2}$ counts/sec. Kinetic Inductance Detectors (KIDs) are a type of superconducting detectors that are single-photon counting, with inherent energy-resolving power, for wavelengths down to $25\,\mu\mathrm{m}$. KIDs do not have a dark current and, therefore, meet the detector requirements for LIFE. This absence of dark current makes KIDs ideal for other low-light level applications in the mid-IR.

In this work, we present the design of lens-absorber coupled single-photon counting KIDs for two wavelengths within the band of LIFE: $10\,\mu\mathrm{m}$ and $18.5\,\mu\mathrm{m}$. The absorber consists of two meandering 23 nm thick Al lines ($\rho = 2.4 \times 10^{-8}\,\Omega\,\mathrm{m}$) with widths of 250 nm and 200 nm for $18.5\,\mu\mathrm{m}$ and $10\,\mu\mathrm{m}$, respectively. The absorber is simulated using the Floquet theorem in CST. The absorber is divided into unit cells simulated with periodic boundary conditions. These unit cells must be smaller than $0.8\lambda_d$ to avoid crosstalk between absorbers. The simulation is performed for all angles from broadside incidence up to the subtended angle of the lens. These simulations show absorption efficiencies for the TE and TM fundamental Floquet modes of up to 81% and 65% for the $18.5\,\mu\mathrm{m}$ design and the $10\,\mu\mathrm{m}$ design, respectively. The absorber acts dominantly as an inductor and is coupled to a coplanar waveguide (CPW) to tune the resonance frequency of the KIDs.

We measured one of the designed chips: a chip with $18.5\,\mu\mathrm{m}$ lens-absorber coupled KIDs on a substrate. We performed power-integrating measurements to estimate the optical coupling of these devices. For these KIDs, we expect a total optical coupling of 1.77. This coupling is calculated with respect to a single mode and 1 polarization. Our absorber can couple to 2 polarizations and multiple modes, resulting in a coupling of larger than 1. The measurements show a reasonable match between the expected and measured optical coupling.

We also performed single-photon counting experiments. The KIDs showed a low resolving power, making distinguishing the source's photons from noise and cosmic rays impossible. Phonon losses due to the substrate were assumed to cause this. Therefore, another chip was measured with $25\,\mu\mathrm{m}$ lens-absorber coupled KIDs on a membrane. The two chips share identical design and fabrication processes, differing only in foundation: one is built on a membrane, the other on a substrate. The KIDs on the membrane showed a relatively high resolving power of approximately 4. This confirmed the hypothesis that phonon losses were the cause of the low resolving power for the KIDs on a substrate.

Future work should focus on redesigning the absorbers and KIDs for use on a membrane and adding a quarter-wavelength backing reflector and matching layer to increase the optical efficiencies of the devices.

Contents

1

Introduction

Search for extraterrestrial life has been one of the main scientific goals of space research. For a planet to be inhabited it must meet several conditions. One of the conditions of life is the presence of CO_2, H_2O and N_2O in the atmosphere. By analyzing the spectra of planets, one can determine the presence of the molecules. Each molecule has unique absorption and emission due to the distinct energy levels of a molecule. These spectral lines of molecules can be seen in the spectrum of a planet. These are called biosignatures. An absence of biosignatures means that life is not possible on the planet, and the presence of biosignatures indicates opportunities for life. Figure 1.1 shows examples of biosignatures in the mid-infrared (mid-IR).

The most important mission in search of biosignatures at the time of writing is the Habitable Worlds Observatory (HWO) mission[1]. It is a space concept mission built upon previous concept missions such as Habitable Exoplanets Observatory (HabEx) [2] and Large Ultraviolet Optical Infrared Surveyor (LUVOIR) [3]. HWO will measure the spectra from ultraviolet (UV) to near-infrared (near-IR) in search of biosignatures. Its goal is to identify and directly image 25 habitable worlds outside our solar planets. However, these spectra are not the only wavelengths containing biosignatures. In figure 1.1, the mid-IR spectra are shown of Earth, Venus, and Mars. As can be seen, all the important spectral lines are present in the mid-infrared range (5 $\mu\mathrm{m}$-20$\mu\mathrm{m}$). This is one major reason for measuring the mid-IR with another space mission complementary to the HWO mission.

Another reason for a mid-IR mission can be found by looking at the flux of the stars and planets. The flux of the star, as well as the flux of the planets, can be described by the Planck formula, which describes the radiation from a perfect black body as a function of both wavelength and temperature. The temperature dependence is quite intuitively: a hotter object emits, in general, more radiation and relatively more radiation with higher energy (or equivalently shorter wavelengths). This means that the peak of the radiation of a star is at a shorter wavelength than the peak of a planet, which is relatively cold compared to a star. As a result, the flux of the planets is relatively large in the mid-infrared wavelength range compared to the optical wavelength range, as shown in figure 1.1b. This is one major advantage of measuring the spectra of planets in the mid-infrared.

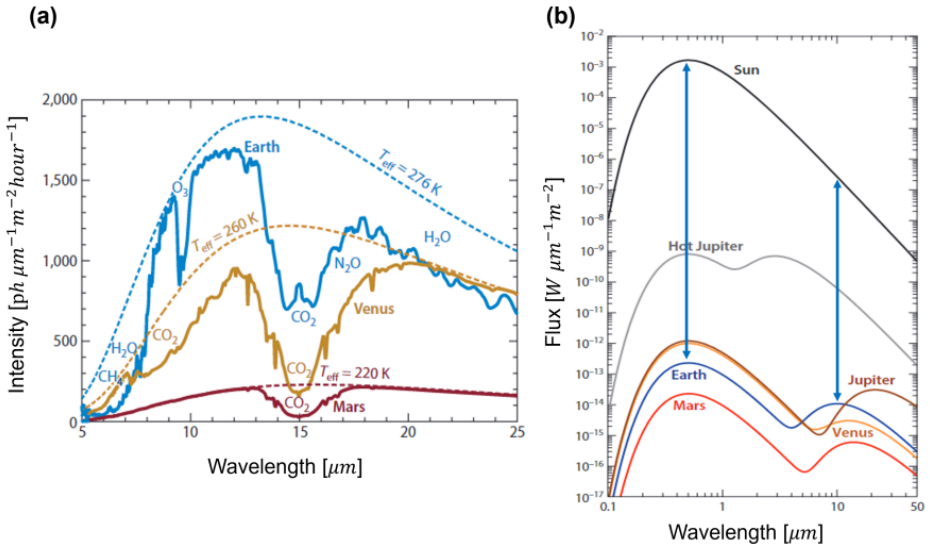

Figure 1.1: Figure (a) shows the spectra of the Earth, Mars, and Venus with the recognizable patterns from the live-indicating molecules: CO_2, H_2O and N_2O. Figure (b) shows the total flux of different planets compared to the star. It can be seen that the flux of planets is relatively large in the mid-infrared part of the spectrum. Figure was adapted from [4] who combined the figures from [5] and [6].

So, it is interesting to research the spectra of planets in the mid-infrared range for the search for life. A space mission that is proposed for analyzing the mid-IR spectra for exoplanets [7] in search of life is the Large Interferometer for Exoplanets (LIFE). In this thesis, the detector will be designed so that it (or its successors) can be used for the LIFE mission. This mission will be explained in further detail in the next section.

1.1. Large Interferometer for Exoplanets (LIFE)

The LIFE mission aims to measure wavelengths between 4-18.5 μm [8]. An artist's impression of LIFE and the working principle are shown in figure 1.2. As explained earlier, the flux of the planets is relatively large at these wavelengths. However, the flux of the star is still larger. To measure the planet's spectrum effectively, the star's signal must be nulled. LIFE does this by introducing a π phase shift in an interferometer. This can be best explained using 1.2b. In this figure, it can be seen that the signal of the star has no optical path length difference at points 1 and 2, meaning that they are in phase. Therefore, introducing a π phase shift means that the signal of the star will interfere destructively and thus be nulled. In contrast, the planet's signal has an optical path length difference at points 1 and 2 in the figure. Therefore, it already has a phase difference, and introducing a π shift does not null the signal. Hence, an interferometer with a π phase shift allows the planet signal to be measured while nulling the star's signal.

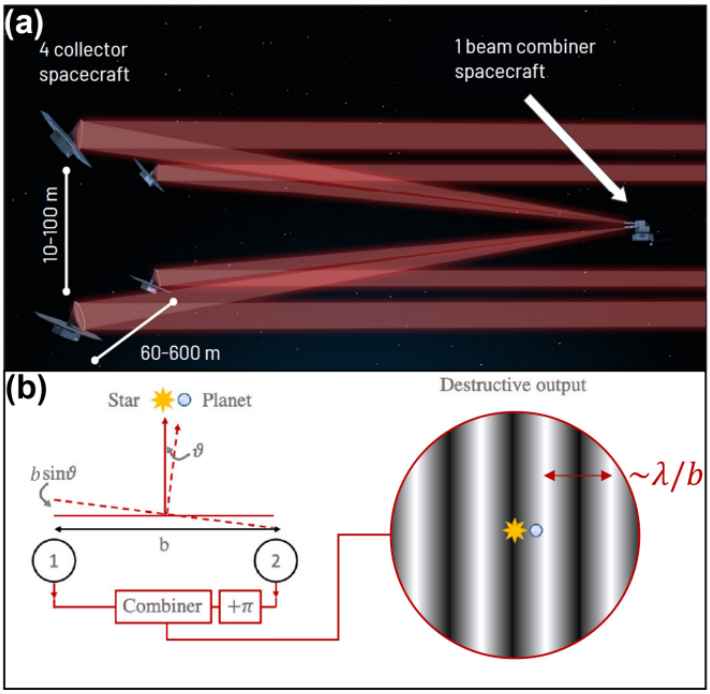

Figure 1.2: Figure (a) shows an impression of the LIFE mission concept. Credit: LIFE initiative [8] Figure (b) shows the working principle of the interferometer. The star signal interferes destructively at the detector, resulting in a sinusoidal fringe pattern from which the planet signal can be measured. Figure adapted from Ras [4].

The LIFE mission will measure the spectra of planets and will thus be a spectrometer. A spectrometer consists of a 1D array of detectors. Each detector covers a part of the frequency band of interest and is optimized for that part. In this thesis, we will only focus on two detectors of this array with only a fraction of the bandwidth of the total bandwidth for the LIFE mission around $10\,\mu\mathrm{m}$ and $18.5\,\mu\mathrm{m}$.

1.1.1. LIFE detector requirements

Now that we have explained the general concept of the LIFE mission, we can discuss the requirements of the detectors used in the spectrometer. To successfully measure the spectra of the planets, the noise of other sources should be limited. This is one of the assumptions made by the LIFE signal simulation [9]. Moreover, the efficiency of the signal coupling to the detector should be sufficient. The requirements for the detector will be set using figure 1.3. Figure 1.3 shows the signal of an Earth-twin located at 10 pc together with the noise sources originating from background radiation and the instrument, assuming an optical efficiency of 70% [9]. Using this figure, we get the most important requirement for designing a detector for the LIFE mission: The dark current is set at a value: $I_D \leq 10^{-2}\frac{ph}{s}$ [9]. One other design requirement is the readout noise. However, the LIFE paper [9] does not mention an explicit limit on the readout noise. Therefore, the requirement for the readout noise is that it should not dominate the contributions from the fundamental noise sources. This is shown in figure 1.3a). This means that the readout noise should be in the same order as the dark current, so the readout noise should be less than $10^{-2}\frac{ph}{s}$.

To conclude the requirements, the LIFE mission concept puts the following requirements on the detectors [9]:

- Wavelength range: 4-18.5 $\mu\mathrm{m}$
- Optical (or quantum) efficiency $\geq 70\%$
- Dark current: $I_D \leq 10^{-2}\frac{ph}{s}$

There is still one remark that has to be made. LIFE is still a concept mission. The requirements, including figure 1.3 are still active research topics and can change. However, the dark current requirement, the most important one, is assumed to be increased, so detectors that meet these requirements will

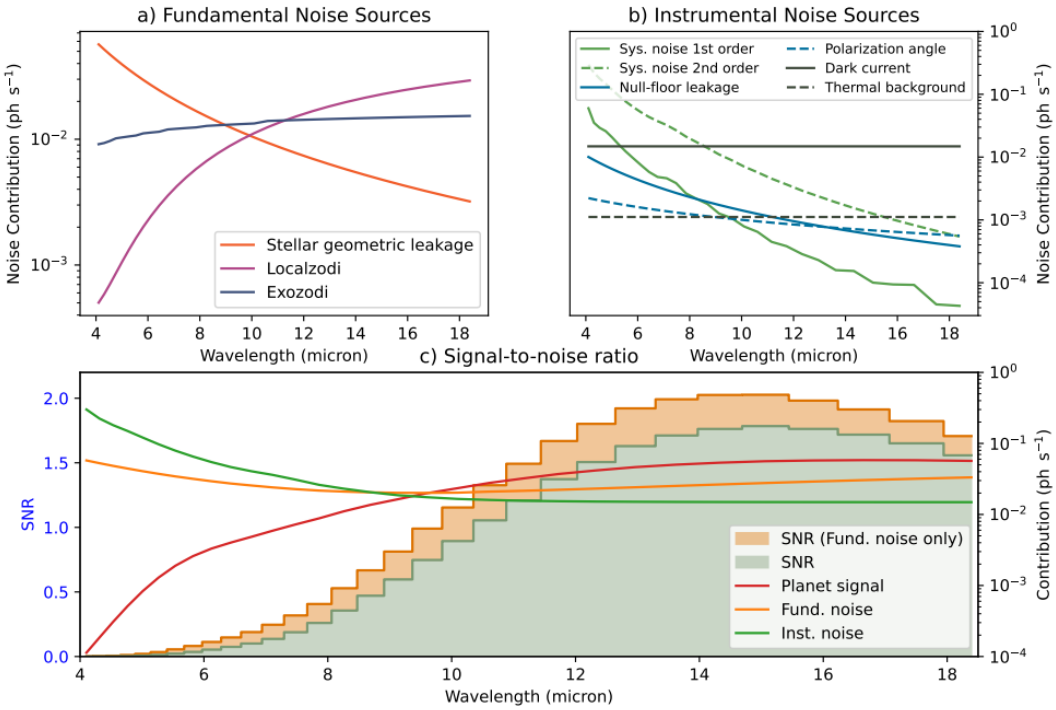

Figure 1.3: The signal and noise expected in the LIFE mission for an Earth-Twin located at 10 pc from the Earth in the mid-infrared frequencies for the LIFE baseline scenario. a) Shows the noise contribution of the fundamental noise sources originating from background radiation. b) Shows the noise contributions from the instruments. In b), the systematic noise sources are displayed in green. For the design of the detectors, the most important requirement is determined here, which is the dark current set at $10^{-2}\,\frac{ph}{s}$. c) Shows the full signal-to-noise ratio and the signal-to-noise ratio from the fundamental noise sources only. The signal and the noise contributions are plotted as a function of wavelength. Figure is adapted from [9].

also meet future requirements.

1.2. Detectors

The requirements for the detectors are quite strict. In general, we can divide detectors into two types: semiconductor and superconductor devices. Both types of detectors have a band gap.

In semiconductors, this is the bandgap between the valence and conduction band. When a photon comes in, an electron gets excited to the conduction band from the valence band. These excited electrons can then be measured. However, the band gap is relatively large for semiconductors, so photons will only excite 1 electron if the energy is high enough. As a result, the energy resolution is zero, as all photons within our range of interest will cause the same electron excitation. Moreover, because of the high energy gap, many photons will not be measured, as their energy is lower than the bandgap. Lastly, all materials with a gap can have excitations due to noise. These excitations will result in a so-called dark current. Due to the low number of excitations during operation, the dark current of a semiconductor device will be relatively high.

Superconductor devices have a bandgap between a state with a Cooper pair and a state with two excited quasiparticles. This bandgap is much smaller (order 1000) than the bandgap between the valence band and the conduction band in semiconductor devices. Therefore, one photon will result in hundreds of excitations in the detector. This results in 3 major advantages:

- We can now measure the colors of the photons as photons with different colors have different energies and thus result in a different number of excitations in the detector. Due to the large number of excitations, this energy resolution can be very high in superconductor devices compared to semiconductor devices.
- Due to the low energy bandgap, we can now measure photons with low energy.
- The number of excitations due to noise in the system is very low compared to the number of excitations caused by the incoming photon. As a result, the dark current of a superconductor device is very small compared to a semiconductor device.

One of the possible superconductor detectors that can fulfill the requirements for the LIFE mission is a microwave kinetic inductance detector. In this thesis, MKID design for the LIFE mission will be researched. In the next section, the working principle of MKIDs will be explained.

1.2.1. Microwave Kinetic Inductance Detectors (MKID)

One of the proposed technologies for LIFE is the Microwave Kinetic Inductance Detector. This type of detector will be researched in this project and is the specialization of the Terahertz group of the TU Delft. The Kinetic Inductance detector is a superconducting detector [10] capable of single-photon counting with energy resolution in the infrared wavelengths [4]. An MKID can be explained as a microwave resonator that consists of an inductance and a capacitance. The inductance component can be split up into two components: the more known geometric inductance and the kinetic inductance due to the inertia of Cooper pairs. Together, the inductance terms and the capacitance determine the resonance frequency. When a photon comes in, it gets absorbed in the detector, breaking a Cooper pair into two excited quasiparticles. As a result, the resonator's resistance and kinetic inductance change, resulting in a different resonance frequency and transmission. This phenomenon is shown in figure 1.4. These changes can be measured using a frequency sweep measurement, and from this, the signal can be reconstructed. This unique resonance frequency is a major advantage over other superconductor detectors as it allows frequency division multiplexing.

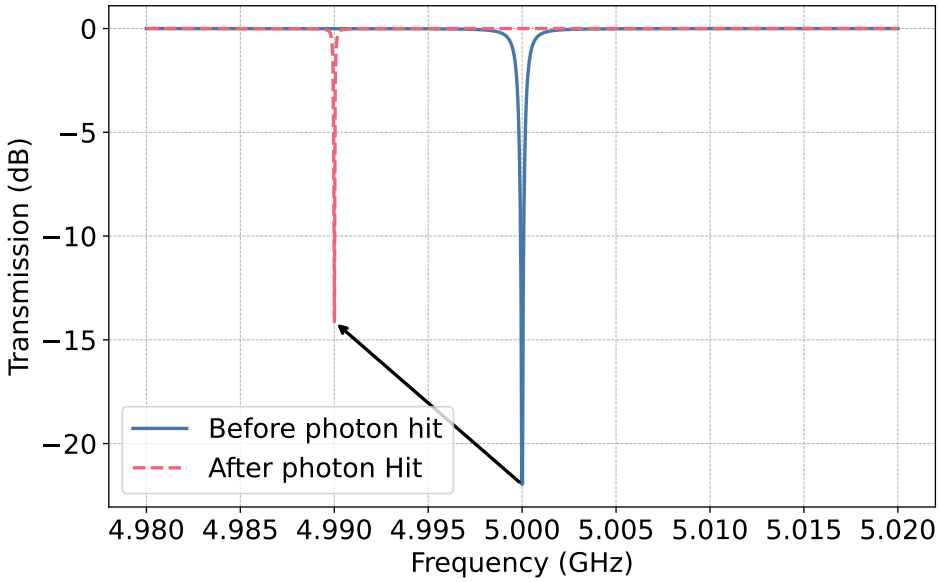

Figure 1.4: The measurement principle of an MKID. An incoming photon breaks Cooper pairs, causing a shift in the resonance frequency and the peak depth. From this, the signal can be reconstructed. The data used is only for illustration purposes.

Previous works have shown that MKIDs are capable of single-photon counting at some of the desired wavelengths ($3.8\,\mu\mathrm{m}$ and $8.5\,\mu\mathrm{m}$) of LIFE as demonstrated in the MSc thesis of Wilbert Ras [4] and at $25\,\mu\mathrm{m}$ as shown in work by Peter Day et al. [11]. So, the current status of MKIDs for mid-infrared wavelengths is that the concept of single-photon counting in the mid-infrared with MKIDS has been proven. However, the detectors must be optimized for high optical coupling in the entire wavelength range while maintaining sensitivity. Therefore, this thesis research will focus on optimizing and designing MKIDs covering a part of the band in the mid-IR.

1.3. Types of KIDs

The first type of KIDs are antenna-based KIDs. They capture the wave via an antenna. After this, the wave is guided towards the resonator, which will break Cooper pairs and cause a response. Antenna-based KIDs have been shown to be very sensitvite [12]. However, antennas in the mid-infrared have several problems, such as very small feature sizes that are hard to fabricate and need a very accurate lens alignment, as they are phase-sensitive. Therefore, this type of KID can not be used in this work.

The second type, LEKIDs, can be described as a lumped element, i.e., they have a separate inductor and capacitor in a KID. In these designs, the inductor is the light-sensitive part that can capture the radiation. They are often used for applications in the visible and near-infrared [13]. However, the sensitivity of these KIDs decreases with increasing wavelength. Therefore, LEKIDs are not sensitive enough for single-photon counting at the higher wavelengths of LIFE.

The last type of KIDs are absorber-based KIDs. These KIDs use an absorbing structure to absorb incoming radiation. The absorber itself is part of the resonator. Absorbers allow for larger feature sizes compared to antenna's and they are incoherent detectors, meaning that they are less prone to lens misalignment. That's why, in this thesis, we will design absorber-based KIDs for the mid-infrared.

1.4. Thesis goals and outline

Main goal

This project is part of a larger goal within the Terahertz sensing group and SRON to demonstrate a sensitive and efficient single-photon counting MKID for the mid-infrared. To be more specific, the goal of this project is:

Simulate, design, and experimentally evaluate microwave kinetic inductance detectors for the

mid-infrared (4-18.5 μm) wavelengths to optimize the optical coupling while maintaining a high sensitivity to allow single-photon counting.

The MKID needs to be designed in such a way that it fulfills the requirements of the LIFE mission. The most important requirements are the efficiency and the sensitivity: it needs to be sensitive enough to count single photons.

Currently, a test bed is being developed in Zurich, Switzerland, to test detectors for the LIFE concept [14], called NICE. This setup will work at 15K and the goal is to demonstrate the sensitivity required for the LIFE mission. The wavelength band used in the NICE setup is focused around $10\,\mu\mathrm{m}$. Therefore, two designs will be made. One is a $10\,\mu\mathrm{m}$ which could be used in the NICE setup. The other is a $18.5\,\mu\mathrm{m}$ KID. This is the highest wavelength of the LIFE mission and theoretically the hardest wavelength for single-photon counting due to its lower photon energy and, thus, lower response.

Sub-goals and outline of the thesis

Absorber for mid-infrared wavelengths

This part of the research involves optimizing the optical efficiency of the detector using the CST software. This part of the work will be based on the work done by Daan Roos (chapter 2 of [15]). His work contains feasibility studies for absorbers for two different wavelengths: $18\,\mu\mathrm{m}$ and $8.5\,\mu\mathrm{m}$. In this thesis, the design of these absorbers will be optimized and analyzed for our use.

The theoretical background of the absorbers is presented in Chapter 2, while their design is described in Chapter 3.

Design of detector

After designing the absorber, the rest of the MKID will be designed. The design of the absorber will give us quite some design constraints. The reason for this is that the absorber has a relatively large kinetic inductance. Therefore, only the resonance frequency needs to be tuned after finishing the absorber design. To effectively readout the MKID, it needs to have a resonance frequency between 2-8 GHz. A frequency smaller than 2 GHz is too slow for single-photon counting, and there exist no amplifiers for frequencies above 8 GHz. Using the absorber design, the rest of the MKID will be designed using the electromagnetic simulation software SONNET.

The theory behind KIDs is presented in Chapter 2, while their design is detailed in Chapter 4. The fabrication process and results are discussed in section 5.

Evaluation of design

The design will be manufactured. After this, the design needs to be evaluated. This is done at the facility of SRON Netherlands Institute for Space Research in Leiden. The goal of the measurements is to get the efficiency and the sensitivity of the device. The measured values will then be compared with the expected theoretical values.

Chapter 6 described the experimental setup used in the measurements. The data analysis and results of the experiment are discussed in chapter 7.

2

Theory

In this chapter, the theory of lens-absorber coupled kinetic inductance detectors (KIDs) will be discussed. We start this chapter with introducing superconductivity and the two-fluid model. After that, we discuss the theory behind KIDS. Then we will discuss the theory behind absorbers and introduce a meandering line absorber. Lastly, we discuss the simulation of the absorber.

2.1. Superconductivity and two-fluid model

In a superconductor cooled beneath its critical temperature, the electron-phonon interactions become stronger than the effective Coulomb force between electrons. As a result, it is energetically favorable for two electrons to form a bound state called Cooper pairs. These Cooper pairs can travel without resistance in the superconductor. Cooper pairs have, as described by Newton's first law, inertia; it takes time for the Cooper pairs to accelerate or decelerate when an electric field is applied. This means that in the case of an AC field, the Cooper pairs will lag behind the voltage of the AC field. The moving Cooper pairs here are the current in the superconductor and act thus as an inductance. This behavior is called kinetic inductance, as the inertia of the Cooper pair causes the inductance.

Cooper pairs are bosons and can thus occupy the same state. Therefore, a single energy is needed to split a Cooper pair into two quasiparticles: $2\Delta = 1.76 k_B T_c$. In this expression, Δ is the energy gap of the superconductor, k_b is the Boltzmann constant, and T_c is the critical temperature of the superconductor. The factor 2 in the expression originates from the fact that 2 electrons are forming a Cooper pair. The energy needed to break Cooper pairs (in Al ≈ 0.37 meV [16]) is very small compared to semiconductors (≈ 1.15 eV in Silicon [17]). This energy is so small that phonons, vibrations in the lattice due to the finite temperature, can break the Cooper pairs. As a result, the superconductor has a non-zero thermal quasiparticle distribution for $T << k_b T_c$ [18]:

$$n_{qp} \approx 2N_0 \sqrt{2\pi k_B T \Delta} \exp\left(-\frac{\Delta}{k_B T}\right). \tag{2.1}$$

Here, N_0 is the single-spin density of states at the Fermi surface. The total number of quasiparticles in the system, N_{qp}, can be found by multiplying n_{qp} by the volume V: $N_{qp} = n_{qp} V$.

The two-fluid model describes the total conductivity of the superconductor. This theory assumes two parallel channels[19]. The conductivity can then be written as: $\sigma = \sigma_1 - i\sigma_2$. The first channel, σ_1, describes the response of the quasiparticles. These dissipate energy by exchanging energy with ions, like normal electrons. This is called Joule heating. The other channel, σ_2, describes the inductive response of the Cooper pair. The Mattis-Bardeen theory [20] gives us the expressions for σ_1 and σ_2 The expressions for σ_1 and σ_2 for a thermal quasiparticle distribution are:

$$\frac{\sigma_1}{\sigma_N} = \frac{4\Delta}{\hbar\omega} \exp\left(-\frac{\Delta}{k_B T}\right) \sinh\left(\frac{\hbar\omega}{2k_B T}\right) K_0\left(\frac{\hbar\omega}{2k_B T}\right), \tag{2.2}$$

$$\frac{\sigma_2}{\sigma_N} = \frac{\pi\Delta}{\hbar\omega}\left[1 - 2\exp\left(-\frac{\Delta}{k_B T}\right)\exp\left(-\frac{\hbar\omega}{2k_B T}\right) I_0\left(\frac{\hbar\omega}{2k_B T}\right)\right]. \tag{2.3}$$

Here, σ_N is the normal state conductivity, Δ is the energy gap of the superconductor: $\Delta = 1.76 k_b T_c$ with k_b being the Boltzmann constant and T_c the critical temperature of the superconductor. I_0 and K_0 are the modified Bessel functions of the first and second kind, respectively. $\hbar$ is the reduced Planck constant, and ω is the angular frequency of the electromagnetic wave.

2.2. KIDs: their working principle and observables

Figure 2.1 shows a microscope image of KID. It consists of a superconducting resonator, which is capacitively coupled to a readout line, with an absorber to absorb incoming radiation. The absorber is discussed in more detail in 2.4. The response of a KID can be derived from the scattering parameters (S-parameters). The S-parameters of a two-port network describe the amplitude and phase relations of the voltage waves at the ports. In our case, the KID can be modeled as a two-port network with the two ports on the readout line before and after the coupler of the KID. This is shown in figure 2.2.

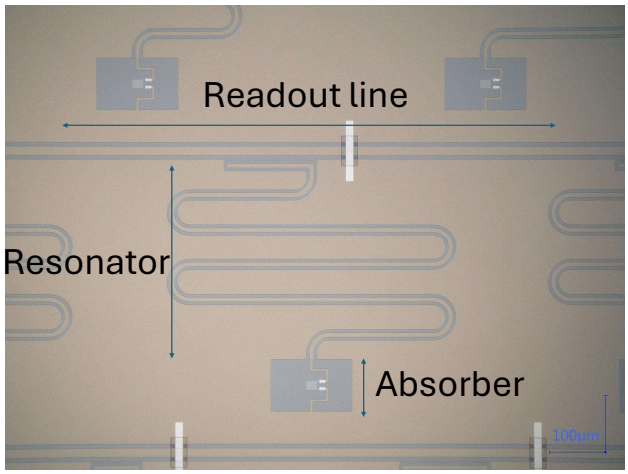

Figure 2.1: Microscope image of a fabricated KID consisting of a transmission line resonator with an absorbing structure as a load. The resonator is capacitively coupled to a readout line.

The forward S parameter from port 1 to port 2 can be expressed as [4]:

$$S_{21} = \frac{2}{2 + \frac{Z_0}{Z_{\text{in}}}} = \frac{\frac{Q}{Q_i} + 2iQ\frac{\delta\omega_0}{\omega_0}}{1 + 2iQ\frac{\delta\omega_0}{\omega_0}}. \tag{2.4}$$

Here, $\delta\omega_0$ en ω_0 are the change in resonance frequency and the resonance frequency, respectively. Q is the quality factor and Q_i the internal quality factor. These are discussed later. S_{21} is a complex quantity that varies with frequency. In the complex plane, its trajectory describes a circle that is shifted from the origin by a horizontal (real) distance x_c. As the frequency increases, the point $S_{21}(f)$ moves clockwise along this circular path. The value of the horizontal shift $x_c = \frac{1+S_{21,\text{min}}}{2}$. Here, $S_{21,\text{min}}$ is the

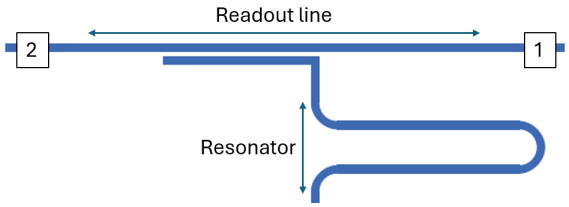

Figure 2.2: The location of the two ports for the S-parameters

minimum transmission from port 1 to port 2, and its value is: $S_{21,\text{min}} = \frac{Q}{Q_i}$. The resonance frequency of the KID is when $\Im\left(S_{21} = 0\right)$, thus at the x-axis crossing of the circle.

The quality factor Q of a resonator is defined as the energy stored per cycle divided by the energy lost per cycle [16]: $Q = \frac{\omega E_{\text{stored}}}{P_{\text{loss}}}$. Here, E_{stored} is the energy stored per cycle, and P_{loss} is the energy loss per cycle.

The quality factor of a resonator consists of two components: the quality factor of the coupler to readout line Q_c and the internal quality factor Q_i. The two quality factors can be added in the following way to find the total quality factor: $\frac{1}{Q} = \frac{1}{Q_c} + \frac{1}{Q_i}$. The internal quality factor of a superconducting resonator is given as [21]:

$$Q_i = \frac{\omega L}{R} = \frac{1}{\alpha_k}\frac{\omega L_s}{R_s} = \frac{2}{\alpha_k \beta}\frac{\sigma_2}{\sigma_1} \tag{2.5}$$

Here, β is a geometric factor. It's expression is: $\beta = 1 + \frac{\frac{2d}{\lambda}}{\sinh\left(\frac{2d}{\lambda}\right)}$ with the thickness of the film d and the magnetic penetration depth λ. β is 2 for the limit of thin films that are used in this thesis [12]. α_k is the kinetic inductance fraction: $\frac{L_k}{L}$. So, now that we have introduced the quality factor, we can discuss its response to a change in conductivity. A change in the internal quality factor, δQ_i, can be calculated via [4]:

$$\frac{\delta Q_i}{Q_i} \approx -\frac{\delta \sigma_1}{\sigma_1} \tag{2.6}$$

with $\delta\sigma_1$ the change in the real part of the conductivity σ_1. We can also calculate the change in the resonance frequency ,$\delta\Omega = \delta\omega - \delta\omega_0$ [4]:

$$\frac{\delta\omega_0}{\omega_0} = \frac{\alpha_k \beta}{4}\frac{\delta\sigma_2}{\sigma_2}. \tag{2.7}$$

Here $\delta\sigma_2$ is the change in the imaginary part of the conductivity σ_2.

So now, we want to know how σ_1 and σ_2 change as function of the number of quasiparticles: $\frac{d\sigma 1}{dn_{qp}}$ and $\frac{d\sigma 2}{dn_{qp}}$. From this, we can derive how the KID will respond to an incoming photon. [22] derived expressions for $\frac{d\sigma 1}{dn_{qp}}$ and $\frac{d\sigma 2}{dn_{qp}}$ for a thermal quasiparticle distribution:

$$\frac{d\sigma_1}{dn_{qp}} \approx \sigma_N \frac{1}{N_0 \hbar\omega}\sqrt{\frac{2\Delta_0}{\pi k_B T}}\sinh\left(\frac{\hbar\omega}{2k_B T}\right) K_0\left(\frac{\hbar\omega}{2k_B T}\right), \tag{2.8}$$

$$\frac{d\sigma_2}{dn_{qp}} \approx \sigma_N \frac{-\pi}{2N_0 \hbar\omega}\left[1 + 2\sqrt{\frac{2\Delta_0}{\pi k_B T}}\exp\left(-\frac{\hbar\omega}{2k_B T}\right) I_0\left(\frac{\hbar\omega}{2k_B T}\right)\right]. \tag{2.9}$$

Here, N_0 is the single spin density of states at the Fermi level, and Δ_0 is the energy gap at zero temperature.

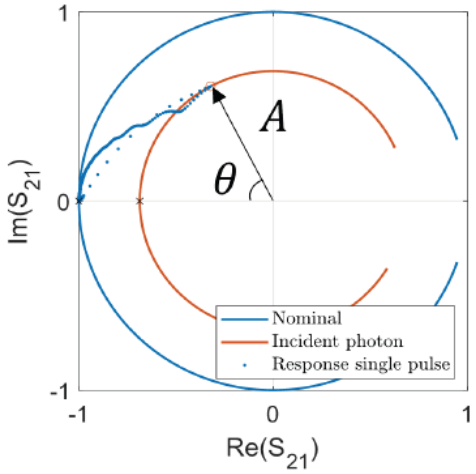

Figure 2.3: The result of a frequency sweep of S_{21}. One can see that an incoming photon increases the phase θ and a decrease of the amplitude A. This figure is adapted from [4].

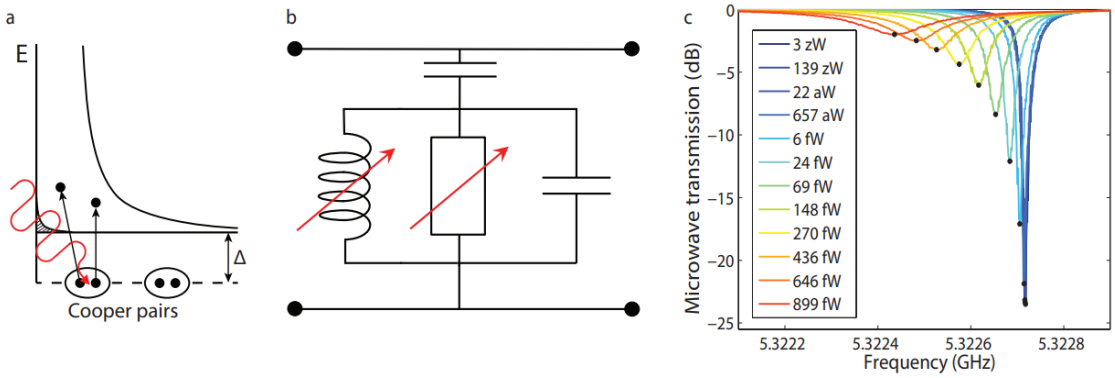

Figure 2.4: This figure demonstrates the working principle of an MKID. Panel a) shows an incoming photon breaking a Cooper pair into two quasiparticles. b) shows a simplified circuit of a capacitively coupled MKID. An incoming photon will change the value of the variable inductance and resistance due to Cooper pair breaking. c) shows the change in the resonance frequency (inductance change) and the height of the dip (resistance change) as a result of an incoming photon for an aluminum microwave resonator. The legend shows the incoming radiation power for photons with a frequency of 1.54 THz. This figure is adapted from [16].

So now, an incoming photon breaking up Cooper pairs and causing a change in n_{qp} can be expressed as a change in S_{21}. and thus ω_0. This principle is shown in figure 2.4. The number of quasiparticles that photons create, N_{qp}, depends on the photon energy E_{ph}: $N_{qp}\frac{\eta_{pb}E_{ph}}{\Delta}$. Here, η_{pb} is the pair-breaking efficiency, which describes how much energy of the energy is used to create quasiparticles. η_{pb} is discussed in more detail in section 4.3. From this we can also see that photons with different energies will create a different amount of quasiparticles. If the photon energy is high enough compared to the band gap energy, we can count single photons with an inherent energy-resolving ability.

We will not use the original S_{21} circle as it is unfavorable due to its shift from the origin. Therefore, we will shift the circle along the x-axis so that the resonance aligns with the origin. The resulting S_{21} is shown in figure 2.3. Thus, we have found observables that we can use. The observables A and θ are expressed as [4]:

$$\theta = \tan^{-1}\left(\frac{\mathrm{Im}(S_{21})}{x_c - \mathrm{Re}(S_{21})}\right), \tag{2.10}$$

$$A = \frac{\sqrt{(\mathsf{Re}(S_{21}) - x_c)^2 + \mathsf{Im}(S_{21})^2}}{1 - x_c}. \tag{2.11}$$

We can also rewrite the observables as functions of the change in the quasiparticle density. This means that we have found a measurement of the KID's responsivity to incoming photons. The responsivity can be expressed as follows [16]:

$$\frac{dA}{dN_{qp}} = -\frac{\alpha_k \beta Q}{\sigma_2 V} \frac{d\sigma_1}{dn_{qp}}, \tag{2.12}$$

$$\frac{d\theta}{dN_{qp}} = -\frac{\alpha_k \beta Q}{\sigma_2 V} \frac{d\sigma_2}{dn_{qp}}, \tag{2.13}$$

These expressions are valid for $T \ll T_c$. In this equation, V is the volume of the inductor (the inductor in this thesis is the aluminum absorber).

For the measurements in Chapter 7, we will use the phase response θ as our observable. This is because A is non-monotonic. θ is monotonic function, which simplifies the data analysis.

So, now we have derived expressions for the final observable. The measurement of the observables is discussed in chapter 6. We will discuss the absorption of infrared photons in the following sections.

2.3. Absorbing infrared photons

To absorb photons, we will add an absorbing structure to the detector. For now, we consider a thin sheet of metal with surface impedance [23]:

$$Z_s = \frac{1+j}{\sigma\delta} \coth\left(\frac{(1+j)d}{\delta}\right). \tag{2.14}$$

Here, δ is the classic skin depth ($\delta = \sqrt{\frac{2}{\omega\sigma\mu_0}}$), ω is the angular frequency and μ_0 is the permeability in vacuum. σ here is the DC conductivity of the metal caused by Joule heating. The frequency of the incoming radiation is much higher than the gap energy of the aluminum. Therefore, one should not consider the Mattis-Bardeen theory for conductivity but for normal conductivity. Equation 2.14 is not valid for all situations. For this, we need to look at the conductivity as given by the Drude model [24, 25, 26]:

$$\sigma(\omega) = \frac{\sigma_0}{1 + j\omega\tau} \tag{2.15}$$

This formula has the frequency-dependent conductivity $\sigma(\omega)$ as a function of the DC conductivity σ_0, angular frequency ω, and mean free time between collisions τ. If the mean free time between collisions of electrons becomes comparable to the period of the incoming radiation: $\tau\omega \gtrapprox 1$, then $\sigma \neq \sigma_0$. In this case, a significant part of the conductor's electrons will not collide with the ions in the material. Here, kinetic inductance starts to show, similar to Cooper pairs, which have effectively a τ of ∞. Moreover, the fundamental part of the conductivity goes to zero for high frequencies, as electrons effectively stay in the same position and no longer carry current. For now, we assume that we are not in this limit. The effect of τ on absorbers is discussed in more detail in 3.4.

Consider an absorbing layer with a surface impedance given by 2.14 between layers of air and a dielectric as shown in figure 2.5. The layer of air have a characteristic impedance of $Z_{air} = 377\,\Omega$ and the dielectric $Z_{di} = \frac{377}{\sqrt{\epsilon_{di}}}$. Here, ϵ_{di} is the relative permittivity of the dielectric. Now, assume a wave from the silicon layer toward the absorbing layer and the air. The reason why we explain this situation becomes clear later on. In that case, you can calculate the reflection on the interfaces based on the impedance via the reflection coefficient Γ_{abs}:

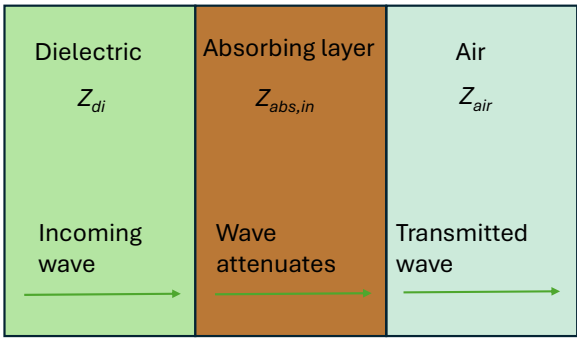

Figure 2.5: Incoming plane wave through a dielectric with characteristic impedance Z_{di}. Part of the wave is absorbed in the absorbing layer with input impedance $Z_{abs,in}$ and part of the wave is transmitted to the layer of air with characteristic impedance Z_{air} behind the absorbing layer.

$$\Gamma_{\text{abs}} = \frac{Z_{\text{L}} - Z_{di}}{Z_{\text{L}} + Z_{di}}. \tag{2.16}$$

Here, Z_{L} is the input impedance of the load. For the physicists among us, this is equivalent to the Fresnel equations with the refractive indices of the materials. Equation 2.16 shows that in the optimal situation, we perfectly match the load impedance Z_l to Z_{di}, and we find that all the radiation will be transmitted to the load. In our case, the load impedance is the parallel combination of the input impedance of the air and the absorbing layer. Thus we have $Z_l = Z_{di}$. From this, we can find that the impedance of the absorbing layer,$Z_{abs,in}$, must be equal to $\frac{377}{1+\sqrt{\epsilon_{di}}}$. In that case, we can find the amount of absorbed power by realizing that the layer of air and the absorbing layer are effectively a voltage divider. This results in a maximum of 77% absorbed power. So, in this situation, 23% of the power is still transmitted.

To solve this, we will include a backing reflector. We will use a good conducting metal with $\sigma \to \infty$ or equivalently $Z \to 0$. Equation 2.16 shows that all the radiation will be reflected with a π phase shift for this metal. If we place this backing reflector at a $\lambda/4$ distance from the absorbing layer, we will introduce another phase of π due to the traveled distance. This means that the radiation will constructively interfere at the absorber. Theoretically, all radiation will then be absorbed, independent of the medium between the absorbing layer and the backing reflector. This allows us to match the absorbing layer only to the dielectric. Therefore, we will include a $\lambda/4$-backing reflector in our design.

All chip layers, including the backing-reflector, must be made on a substrate. We will use silicon for the substrate as it is used in KIDs with the highest shown sensitivity [12]. Silicon has a lower characteristic impedance ($Z_{si} \approx 111.5\,\Omega$) compared to air. Therefore, the chip will be illuminated through the substrate as it allows for easier matching with air compared to the front side. Figure 2.6 shows the layer configuration for the situation where back-illumination is used. We will also add a silicon lens on top of the substrate to focus the radiation on the absorber.

The detector's sensitivity depends on the material used for the absorbing layer. Therefore, we will use Aluminum for the absorbing layer as it is the material for the KIDs with the highest shown sensitivity [12, 27].

Equation 2.14 reduces to $Z_s = (1+j)(\frac{\mu\omega}{2\sigma})^2$ for $t >> \delta$. The real and imaginary parts are equal in this situation, resulting in reflections for the case of a thick slab. Therefore, we need to use a thin aluminum sheet, smaller than the skin depth, to increase the real part of the impedance. The resulting surface impedance of 2.14 for a 23 nm aluminum sheet (the thinnest that can reliably be produced) with a resistivity of $2.43 \cdot 10^{-8}\ \Omega\,\text{m}$ is shown in figure 2.7.

It can be seen from figure 2.7 that the real and imaginary parts of the impedance are comparable. For the absorber to work optimally, the real part of the aluminum absorbing structure should be matched to the silicon, and the imaginary part should be as small as possible. We will need to use a design that

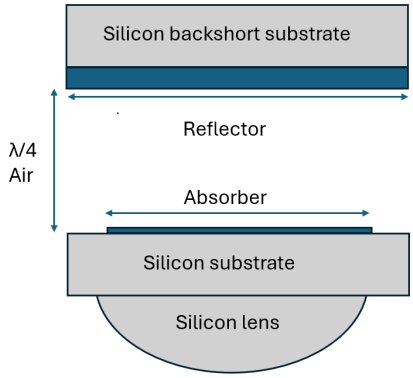

Figure 2.6: The layer configuration for backside illumination. We have a silicon lens that focuses the radiation on the absorber. Both the absorber and reflector are made on a silicon substrate.

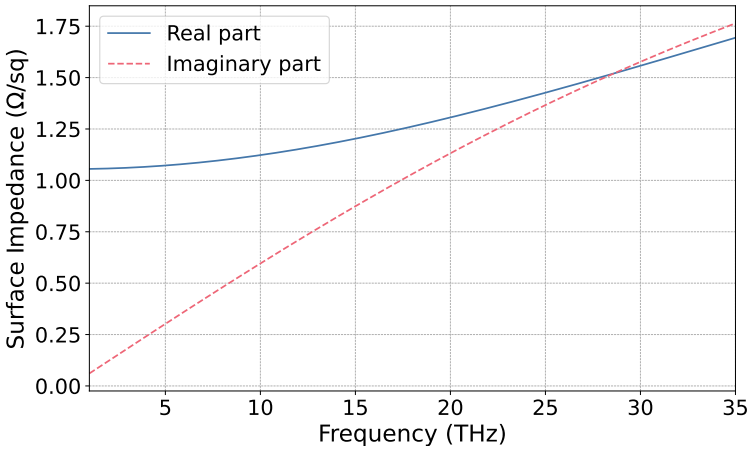

Figure 2.7: Surface impedance calculated using equation 2.14 for 23 nm thick aluminum with a resistivity of $2.43\,\mu\Omega\,\mathrm{cm}$, as used in this work.

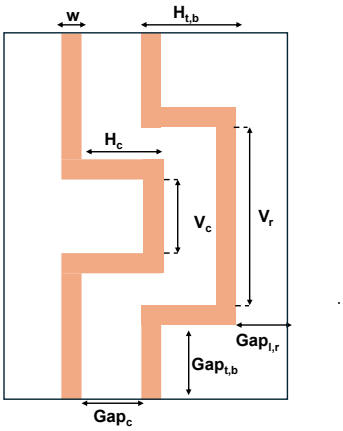

Figure 2.8: An overview of the meandering line absorber design.

uses a filling factor that is high enough to match the real part while canceling the imaginary part. These designs will be discussed in the next section.

2.4. Absorber

The first option is a strip absorber, which consists of straight aluminum lines with air in between [28]. However, there are two major downsides to this design. The first is that we only have lines in one direction. This means that we can only absorb one of the two polarizations of the radiation. The second problem is the required width of the aluminum lines. This design has an analytical impedance equation [28]. Daan Roos [15] used this equation to show that the width of the lines must be 45 nm for 30 THz, This is much narrower than the current fabrication limits of a minimum 250 nm line width.

Instead, we can use a meandering line absorber, like the one in figure 2.8. This structure has two meandering lines in the unit cell. We now have lines in two directions to absorb two polarizations.

Secondly, more parameters can be tuned. As a result, the impedance of this absorber structure can be matched more easily. This especially allows for tuning of the imaginary part of the impedance compared to other designs such as the strip absorber. However, this also makes the structure more complex. Parameters cannot be treated as independent variables. Changing one variable to, for example, add or remove capacitance between the lines often also changes the capacitance at other places.

As a result of the inductive and capacitive couplings in the two meandering lines, the absorber acts similarly to a resonator with the maximum absorption efficiency at the point where the imaginary impedance is zero. Figure 2.9 shows this resonant behavior for 1 polarization. The location of the peak can be tuned, and the height is optimized by matching the impedance to the dielectric on top. Both polarizations do have their own response and we thus need to tune two peaks. This optimization process is not trivial, as this absorber has no analytical expressions yet. Therefore, we must simulate and optimize the structure with CST [29]. The simulation and optimization of the absorber will be discussed in section 3.1. After the absorber is optimized, the KID can be designed. This is discussed in chapter 4, but first, the important theory of KIDs will be discussed in the next sections.

2.5. Absorber simulation

Simulating the full absorber structure with a dielectric lens on top is time-consuming. Therefore, we will split the simulations into two parts. We simulate the incident radiation at the lens to the absorber with the GOFO as described in [15]. The result is a spectrum of plane waves at the absorber [30]. The GOFO simulation for our measurements is discussed in 6.4.

In bounded media, only specific solutions to the Maxwell equations exist due to the boundary conditions. These solutions are called spatial modes. In the lens and substrate, two types of modes, called polarizations, exist: transverse electric (TE) modes and transverse magnetic (TM) modes. The TE and

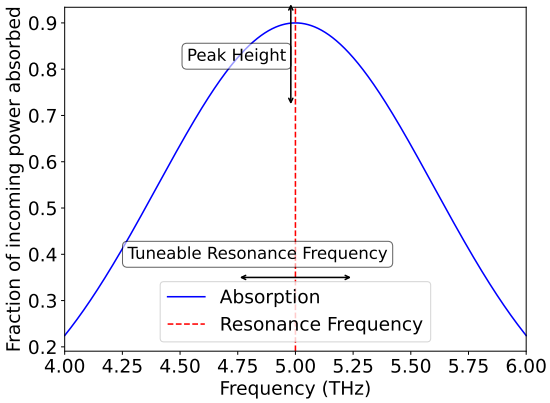

Figure 2.9: A schematic view of the absorption peak of an absorber. It shows the tunable resonance frequency and an optimizable peak height for 1 polarization. Both polarizations have a different response and we thus need to optimize the peaks of both polarizations. The data used is only for illustration purposes.

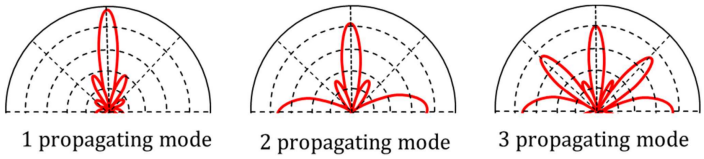

Figure 2.10: The Floquet modes transmitted from a point source. The absorber will receive and reflect radiation at higher angles if higher-order Floquet modes exist in the structure. Figure from [32].

TM modes have no electric or magnetic fields in the propagation direction, respectively.

Simulating the response with spatial modes can be very time-consuming, as we must simulate the complete absorber. Therefore, we will exploit that our absorber is periodic and can be divided into unit cells. If we use this periodicity and assume an infinite array of unit cells, we can use another type of modes called Floquet modes [31]. These modes are periodic, meaning that the field is the same in all unit cells at the same position within the unit cell. As a result, we can now only simulate one unit cell instead of the full absorber, reducing the simulation time heavily.

Figure 2.10 shows that higher order Floquet modes will cause the absorber to receive and reflect power at larger angles. The reflection can be especially problematic as other absorbers can absorb this power. In that case, there will be crosstalk between the absorbers. Therefore, we want the first two Floquet modes to only interact with the absorber to limit this. To do this, we need to make the distance between unit cells within the absorber so small that the radiation falling on the unit cells can only be in phase for radiation under relatively small angles. This can be achieved when the unit cell is small compared to the wavelength. We can derive this using the frequency at which a higher-order Floquet modes appears [33]:

$$f = \frac{c}{d(\sin\theta\cos\varphi + 1)}. \tag{2.17}$$

Here, d is the periodicity, θ is the polar angle, ϕ is the azimuth, c is the speed of light, and f is the frequency. Using this formula and the fact that we will scan ϕ from 0 to 90 and θ from 0 to θ_0 it can derived that

$$d \leq \lambda_d \left(\frac{1}{\sin\theta_0 + 1}\right). \tag{2.18}$$

Here, λ_d is the wavelength of the material before the absorber, so in our case, the dielectric lens. Our lens has a f-number of 2 ($f_\# = f/D$) We can now use that our lens has a maximum scanning angle of $\theta_0 = \sin^{-1}\left(\frac{1}{2f_\#}\right) = 14.5$ to find the constraint of the periodicity for our design:

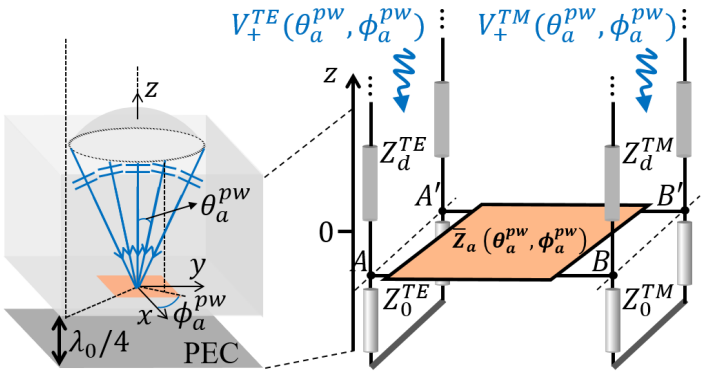

Figure 2.11: The Floquet wave model for the lens absorber geometry. In this model, you have two incoming plane waves modeled as incoming voltage waves connected to the absorber via two transmission lines, which model the dielectric lens Z_d. The backshort is modeled as a short (PEC). The response is a function of the angles of the plane wave with respect to the absorber: θ_a^{PW} and ϕ_a^{PW} [31].

$$d \leq 0.8\lambda_d = 0.8\frac{\lambda_0}{\sqrt{\epsilon_r}} \tag{2.19}$$

In this formula, λ_0 is the wavelength in free space, and ϵ_r is the relative permittivity of the dielectric lens. So if we meet this requirement, we know that all the power in the system is carried by the TM and TE fundamental Floquet modes.

The equivalent transmission line model for the first two Floquet modes for an absorber structure with lens and backshort is shown in figure 2.11 [31]. Firstly, we have the dielectric characteristic impedance Z_d to feed incoming plane waves to the absorber. The absorber's response to the two Floquet modes and their crosstalk are represented as Z-parameters in $\bar{Z}_a$. After the absorber, there is a layer of air with characteristic impedance Z_0. The backing reflector is modeled as a perfect conductor and thus a short in the model.

We simulate this in the software CST Studio Suite [29]. The simulation will be done using the frequency domain solver with periodic boundaries along the surface of the absorber. The boundary condition for the axis perpendicular to the absorber is set to closed for the side of the lens and open (PEC with electric field is zero) for the backing reflector side. An overview of the unit cell in CST is shown in figure 2.12.

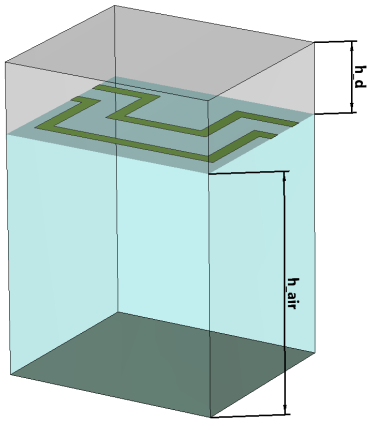

Figure 2.12: A unit cell simulation in CST. On the top layer we have a grey coloured dielectric lens with height h_d followed by the absorber structure in green. Behind the absorber there is a layer of air h_{air}, which is coloured blue in the figure, with a black coloured backing reflector at the end. In this work $h_{\text{air}} = \lambda/4$ as the backing reflector performs optimally in that case.

3

Mid-infrared absorber

In this chapter, the optimization and results of absorbers are discussed. The theory behind absorbers was previously introduced in chapter 2. Firstly, we discuss the optimization process of the absorber. Afterwards, the optimized unit cells are presented. Then we discuss the full absorber design and introduce the relevant efficiencies. We end this chapter with a study on the effect of uncertainties in material parameters on the absorber performance.

3.1. Optimizing an absorber

To analyze the performance, we need to define the absorption efficiencies of the absorbers in terms of the output of the CST simulations. We can define the absorption efficiencies for both Floquet modes and the average as function of the S-parameters:

$$\eta_{\text{abs},TE} = \left(1 - |S_{TE,TE}|^2 - |S_{TM,TE}|^2\right) \cos\theta, \tag{3.1}$$

$$\eta_{\text{abs},TM} = \left(1 - |S_{TM,TM}|^2 - |S_{TE,TM}|^2\right) \cos\theta, \tag{3.2}$$

$$\eta_{\text{abs,avg}} = \frac{\eta_{\text{abs},TE} + \eta_{\text{abs},TM}}{2}. \tag{3.3}$$

Here, $S_{1,2}$ means the scattering parameters from excitation at the Floquet mode port 2 and observing reflected voltage at the Floquet mode port 1. In other words, for each Floquet mode, the efficiency is defined as the total power minus the power being reflected in the same Floquet mode and the reflected power that has been transmitted to the other Floquet mode.

In this equation, the $\cos\theta$ term originates from a normalization that CST uses for the power. On broadside incidence, theoretically, all the power could be absorbed by a perfect absorber as the area that the wave sees is at its maximum. At $\theta = \pi/2$, the incoming wave does not 'see' the absorber at all as it is coming from the side, and this means that 0 $\%$ of the power will be absorber. This is known as Lambert's cosine law. However, CST does not account for this, and therefore, an extra $\cos\theta$ is added.

At the moment of writing, there does not exist an analytical model or an optimization technique for this absorber structure. The best optimization technique at the moment of writing is a table made by Daan Roos [15] that describes the qualitative changes in TE and TM's efficiencies and resonance frequencies. This table was made for frequencies around 1.5 THz. During this work, it was noticed that these relations do not always hold. A reason for this could be that the dimensions are totally different. Both, absolute and also relative to each other within the unit cell. Another problem is that it is not always possible to change only one parameter due to fabrication limits and the periodicity constraint of equation 2.19, i.e., an increase of one parameter results in a decrease or increase of another parameter. However, this table is still valuable for future work at higher frequencies than the original frequency as it works in general. So, it can be used to start the optimization process to change the frequency of a

previously made absorber design. Moreover, it is also valuable for inexperienced people as they will understand how the parameters will affect the results.

Table 3.1: An indication of how the results change after changing dimensions. f_{TE} and f_{TM} represent the resonance frequencies of the structure for TE and TM polarization, respectively. max($\eta_{\text{abs,TE}}$) and max($\eta_{\text{abs,TM}}$) represent the absorption efficiencies of TE and TM polarizations at the resonance frequency of the structure. The findings of Daan Roos [15] reported here indicate the effect after increasing the mentioned dimension and indicate how much a parameter increases (indicated by the number of +), decreases (indicated by the number of −), or stays relatively the same ( ).

Parameter	**Change in** f_{TE}	**Change in** f_{TM}	**Change in max** ($\eta_{\textbf{abs,TE}}$)	**Change in max** ($\eta_{\textbf{abs,TM}}$)
$H_{t,b}$	- - -	-	- -	+++
H_c	- -	-	+	—
V_r	- -	- -	- -	++
V_c	$\sim$	-	+	–
gap_c	-	++	-	$\sim$
$gap_{t,b}$	$\sim$	- - -	+	-
$gap_{l,r}$	+++	$\sim$	$\sim$	-

For optimization of the absorbers two ratios were defined. The goal of these ratios is to compare different designs. The first ratio uses a comparison with a 'perfect' absorber following the cosine Lambert law. This ratio is more interesting from the engineering perspective as one can easily compare designs with respect to the most ideal case. This ratio is defined as:

$$\eta_{\text{eng}} = \frac{\int\int \eta_{\text{abs}}(f_{\text{center}}, \theta, \phi) \sin\theta d\theta d\phi}{\int\int \eta_{\text{perfect,abs}}(f_{\text{center}}, \theta, \phi) \sin\theta d\theta d\phi} \tag{3.4}$$

Here, η_{eng},η_{abs}, $\eta_{\text{perfect,abs}}$ are respectively the 'engineering ratio' of the two efficiencies, the efficiency of the absorber designs and the efficiency of the ideal absorber, which obeys the Lambert cosine law. All are evaluated at the center frequency, f_{center}.

In the second ratio, the absorber is compared to an absorber that perfectly absorbs all the incoming power. This situation is physically not possible, but it is interesting from a physics perspective to know how much of the incoming power is lost. Its definition is:

$$\eta_{\text{phy}} = \frac{\int\int \eta_{\text{abs}}(f_{\text{center}}, \theta, \phi) \sin\theta d\theta d\phi}{\int\int \eta_{\text{all}}(f_{\text{center}}, \theta, \phi) \sin\theta d\theta d\phi} \tag{3.5}$$

Here, η_{phy},η_{abs}, η_{total} are, respectively, the 'physics ratio' of the two efficiencies, the efficiency of the absorber designs and the efficiency of an absorber that absorbs all the incoming power.

3.2. Optimized absorber unit cells

For optimization of the absorber, the absorption efficiencies have been evaluated from broadside incidence up to the maximum subtended angle of the lens, which is $15°$. First, the efficiencies were evaluated at broadside incidence. This was done for a frequency band around the center frequency of the absorber. The result is shown in figure 3.1.

The right panel of figure 3.1 shows that the $18.5\,\mu\text{m}$ design has a higher fraction of absorber power as it can be matched better to the silicon lens. This is because the wavelength is higher, and thus, larger structures can be used. For the $10\,\mu\text{m}$, one needs to use smaller structures due to the constraint on the periodicity of the unit cells described in equation 2.19. As a result, the unit cell for the $10\,\mu\text{m}$ design is smaller. This structure is so small that at the moment of writing, the lines and the gaps between the lines need to be smaller than the minimum gap size of 500 nm and minimum line width of 250 nm. Therefore, the decision was made to make the gaps the same size and, in this way, spread the risk of failure during fabrication. This was especially a problem for the TM polarization as there is an extra gap vertically compared to horizontally (see figure 2.8). This effect can be seen by the lower absorption for the TM Floquet mode in the left panel of figure 3.1.

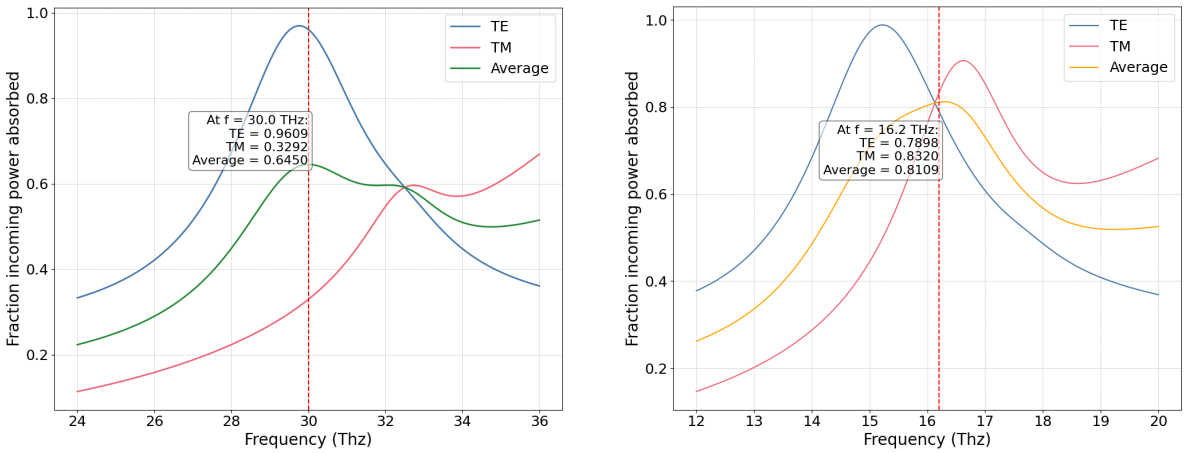

Figure 3.1: The fraction of the incoming power absorbed in both absorber designs. The incoming power is modeled using the Floquet wave model in CST for incoming TM and TE plane waves. **Left:** Fraction of incoming power absorbed in the $10\,\mu\mathrm{m}$ absorber. **Right:** Fraction of incoming power absorbed in the $18.5\,\mu\mathrm{m}$ absorber.

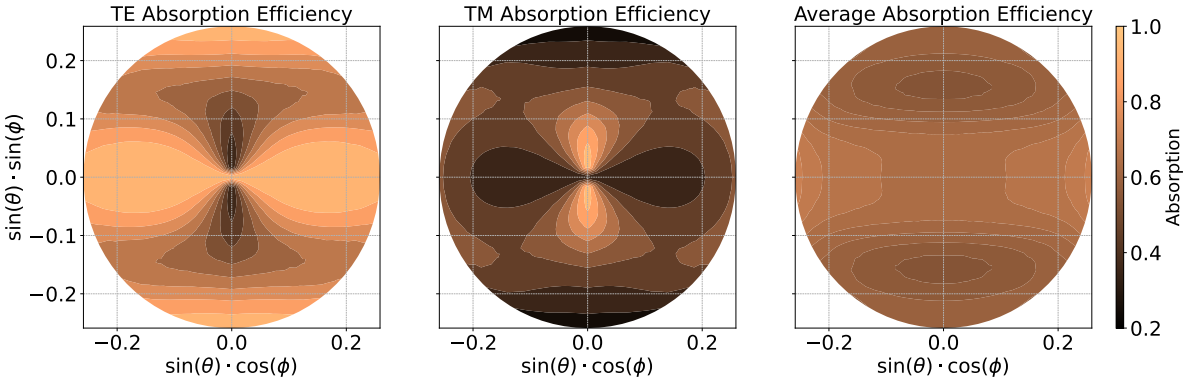

Figure 3.2: The absorption efficiency of both Floquet modes (TE and TM) and the average absorption efficiency as a function of u,v coordinates for the $10\,\mu\mathrm{m}$ absorber made of 23 nm thick aluminum.

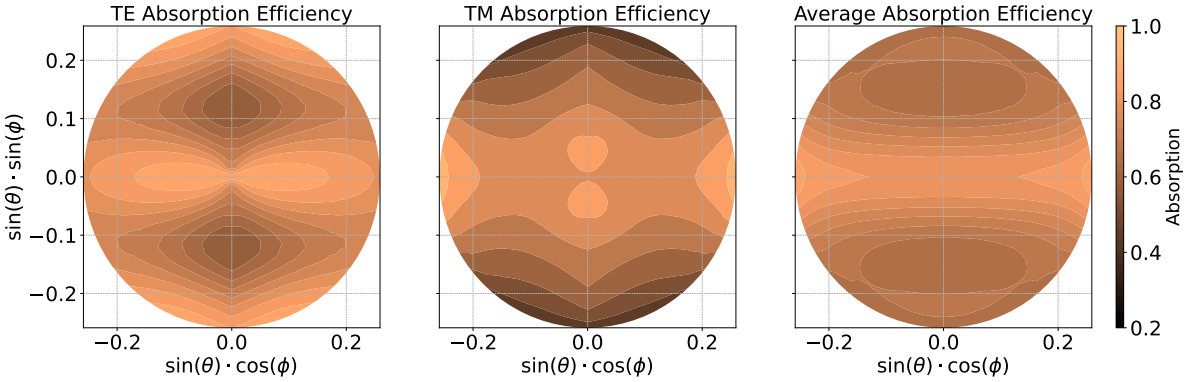

Figure 3.3: The absorption efficiency of both Floquet modes (TE and TM) and the average absorption efficiency as a function of u,v coordinates for the $18.5\,\mu\mathrm{m}$ absorber made of 23 nm thick aluminum.

Moreover, the efficiency was evaluated for different incoming angles of the plane wave. The result is shown in figures 3.2 and 3.3. In order to reduce the simulation time, two measures were taken for this simulation. Firstly, symmetry in the four quadrants was used. The simulation in CST was done with angles ϕ from 0 to 90 $^\circ$ and θ from 0 to 15. In post-processing, the quadrants were mirrored to show the complete response of the absorber as a function of angles ϕ and θ. Secondly, only the center

wavelength was simulated to reduce the computation time.

This optimization of the absorber resulted in two designs for the unit cell. One design for 10 µm and another design for 18.5 µm. The resulting parameters are shown in table 3.2.

Table 3.2: Parameters of the optimized 10 µm and 18.5 µm absorber unit cells.

Parameter	10 µm	18.5 µm
Gap left and right ($gap_{l,r}$)	0.36	0.55
Gap top and bottom ($gap_{t,b}$)	0.19	0.25
Gap center (gap_c)	0.50	0.50
Horizontal top and bottom ($H_{t,b}$)	0.93	1.86
Horizontal center (H_c)	0.63	1.25
Vertical right (V_r)	1.58	3.24
Vertical center (V_c)	0.40	1.61
Width (w)	0.20	0.25

The values of both efficiency ratios, used for optimization, of the final designs of the 18.5 µm and 10 µm absorbers are shown in table 3.3.

Table 3.3: Comparison of the two efficiency ratios of equations 3.4 and 3.5 for the 10 µm and 18.5 µm absorber unit cells final designs.

Efficiency Ratio	**Design Type**	
	10 µm	18.5 µm
η_{eng}	0.63	0.74
η_{phys}	0.62	0.72

3.3. Full absorber design

Previously a design was presented for the unit cell. Now the total width of the absorber will be determined. For this purpose 2 types of efficiencies need to be discussed first: the aperture efficiency and the focus efficiency.

The aperture efficiency describes how much of the desired incoming power from the source is absorbed in the absorber. The aperture efficiency is the ratio of the maximum absorbed power across all frequencies and incidence angles to the total incoming power:

$$\eta_{ap}(f) = \frac{\max\left\{P_{abs}(f, \theta_l^{pw}, \phi_l^{pw})\right\}}{P_{inc}}. \tag{3.6}$$

Here, P_{inc} is the incident power on the lens's aperture, and P_{abs} is the power absorbed in the absorber as a function of frequency and lens angles $\theta_l^{pw}$and ϕ_l^{pw}. P_{inc} is set, but P_{abs} can be varied as seen in it's expression [31]:

$$P_{\text{abs}}(f, \theta_l^{pw}, \phi_l^{pw}) = \frac{1}{2}\Re\left\{ \iint_{-w/2}^{w/2} \left[\vec{E}_t(\vec{\rho}, \theta_l^{pw}, \phi_l^{pw}) \times \vec{H}_t^*(\vec{\rho}, \theta_l^{pw}, \phi_l^{pw})\right] \cdot \hat{z}\, d\vec{\rho} \right\}. \tag{3.7}$$

Here, the Poynting vector of the total electric and magnetic field (respectively, E_t and H_t) is integrated over the dimensions of the total absorber. In this formula, w is the total width of the full absorber. As can be seen, increasing the width of the absorber increases the integration domain. This means that we increase the absorbed power P_{abs}, which increases the aperture efficiency η_{ap}.

The second efficiency that plays a role in the choice of absorber width is the focusing efficiency η_f. This efficiency describes describes how close the pattern is compared to the pattern to the situation with an ideal focus. The focusing efficiency is defined as the overlap of the solid angles of the reception pattern (Ω_0) and the solid angle of a perfect focus, an Airy pattern (Ω_{Airy}) [31]:

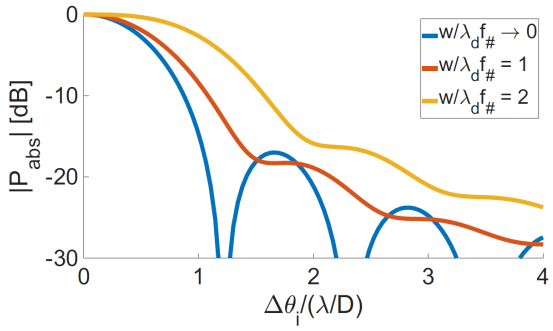

Figure 3.4: The normalized patterns for lens-absorbers of 3 different sizes. Increasing the size, widens the patterns and reduced the focus efficiency. Figure from [15].

$$\eta_f = \frac{\Omega_{\text{Airy}}}{\Omega_0}. \tag{3.8}$$

The solid angle of an Airy pattern is known [34]:

$$\Omega_{\text{Airy}} = \frac{\lambda^2}{A_{\text{lens}}}. \tag{3.9}$$

Here, λ is the wavelength of the plane wave incident on the lens, and A_{lens} is the area of the lens aperture. The solid angle of the reception pattern is given as [31]:

$$\Omega_0 = \int_0^{2\pi} \int_0^{\frac{\pi}{2}} F(f,\theta,\phi) \sin\theta \, d\theta \, d\phi, \tag{3.10}$$

where the reception power pattern is defined as:

$$F(f,\theta_l^{pw},\phi_l^{pw}) = \frac{P_{\text{abs}}(f,\theta_l^{pw},\phi_l^{pw})}{\max\{P_{\text{abs}}(f,\theta_l^{pw},\phi_l^{pw})\}}. \tag{3.11}$$

Suppose we increase the width of the absorber in equation 3.7, then we increase the domain over which we integrate the Poyting vector, resulting in a larger P_{abs} and a wider pattern as shown in figure 3.4. This originates from the fact that absorbers are multi-moded detectors that couple incoherently. Compared to single-moded devices, we can now receive power from new angles, effectively resulting in a larger Ω_0 and thus a lower focusing efficiency. So, an increase in the width of the absorber results in an increase in aperture efficiency η_{ap} and a decrease in focusing efficiency η_f. This means we have an optimization problem for the width of the absorber w.

The primary goal of this thesis is to achieve efficient single-photon counting at the specified wavelengths in the mid-infrared range. Consequently, we make the design two make two designs. One designs prioritizes η_{ap} over η_f to increase the optical coupling of the detector. Previous studies have shown that the optimal absorber width for this purpose is approximately $w \approx 2\lambda f_{\#}$, as η_{ap} does not increase significantly beyond this point. At the same time, η_f continues to decrease substantially [15, 31]. Therefore, the absorber width and the corresponding number of unit cells are selected as close to $2\lambda f_{\#}$ to maintain this balance. The second designs has a lower number of unit cells compared to the first design to decrease the Al volume and thus increase its responsivity. Both designs always have an odd number of unit cells so that always a unit cell is located in the focus point of the lens. The exact number of unit cells will be discussed in chapter 5. The calculation the aperture and focus efficiency is discussed in section 6.4.

3.4. Effect of uncertainties in material parameters on the absorber performance

In the design process of the absorber previously described in this chapter, all the material parameters were assumed to be known with high certainty. These values were either from a database from SRON with data from previously made KIDs or estimated from the literature.

However, the parameters can never be known with such a high certainty. Especially, the thickness and resistivity ρ often differ slightly from the aimed values. For other parameters, such as the mean free time between collisions τ, uncertainty can cause problems. τ, for example, can not be measured easily; only a theoretically calculated value can be found.

Therefore, in the next section, a tolerance study is conducted to show the effects of differing material parameters on absorption efficiency. Firstly, the effect of uncertainties in the thickness and conductivity of the material are discussed. This is followed by an analysis of the impact of τ and the Drude model on the absorption efficiency.

3.4.1. Effect of different resistivity and material thickness on the absorption

Firstly, the effect of different thicknesses and DC resistivity is researched. The impact of these parameters is combined as the DC resistivity and the thickness are related. The DC resistivity of a metal is inversely proportional to its thickness. These are thus not two independent parameters and, therefore, researched together.

The effect of a difference in resistivity in thickness is modeled in CST for the $10\,\mu\mathrm{m}$ design. The setup is the same as before (as described in section 2.5), and the geometrical parameters are the final parameters of the $10\,\mu\mathrm{m}$ design (as described in section 3.2). The only variation is the change in material. For the change in the material, three different sets of parameters are used from a database of SRON with measured parameters for aluminum

- Thickness d = $21\,\mathrm{nm}$, resistivity ρ = $3.59\,\mu\Omega\,\mathrm{cm}$
- Thickness d = $23\,\mathrm{nm}$, resistivity ρ = $2.43\,\mu\Omega\,\mathrm{cm}$
- Thickness d = $28\,\mathrm{nm}$, resistivity ρ = $1.74\,\mu\Omega\,\mathrm{cm}$

The surface impedance was calculated like before via equation 2.14 for these parameters. The result of the CST simulation for the average absorption efficiency in the case of broadside incidence is shown in figure 3.5.

Figure 3.5 shows that the change of material parameters mostly influences the height of the absorption peaks and not its frequency location. From this, it can be concluded that the imaginary impedance of the absorber is dominated by its geometrical components. This is a positive conclusion regarding tolerance, as a lower resistivity than designed will not cause a significant decrease in the absorber's performance.

3.4.2. Effect on the absorption due to the scattering time

Secondly, the effect of electron collisions as described by the Drude model, which is discussed in section 2.3, is researched. For this effect, different values for τ are used. The value for τ for our film of aluminum is found using the free electron model [26]:

$$\tau = \frac{3}{128\pi^4\hbar^2 N_0^3 E_F^4 e^2 \rho} \tag{3.12}$$

Here, N_0 is the Fermi density of states (single spin), and E_f is the Fermi energy. Using values from [35] for N_0 and E_F, we find that $\tau \approx 15\,\mathrm{fs}$. This is in agreement with the value of $\tau = 13\,\mathrm{fs}$ found for aluminum with a similar thickness [11].

To model the effect of different τ values, we vary this parameter over two orders of magnitude, from $\tau = 150$ fs to $\tau = 1.5$ fs to see the effect on the absorber's performance and plot the resulting absorption efficiencies in figure 3.6. In this figure $\tau = 0$, the situation without scattering is also added as a reference.

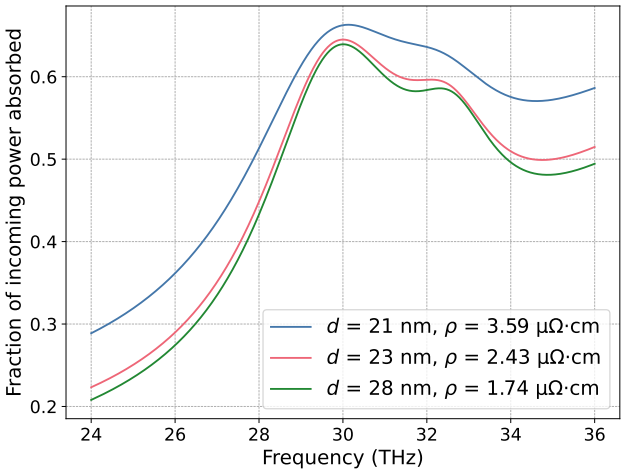

Figure 3.5: The effect of different material parameters on the average absorption efficiency for broadside incidence of the $10\,\mu\mathrm{m}$ (30 THz) absorber design. The sets of ρ and d are from data of previously measured KIDS. It shows that different material parameters do influence the peak's height but do not significantly influence the frequency of the maximum height of the peak. This means that the inductance and capacitance in the absorber are dominated by its geometric components and not the intrinsic inductance of the line.

The impact of the electron collisions is added via a frequency-dependent conductivity as in equation 2.15. This increases the surface impedance of the material, as explained in section 3.1.

Figure 3.6 shows that the absorber performance is influenced significantly for $\tau >> 15$ fs. However, for smaller variations in τ, other parameters, such as conductivity and the width of the lines, are expected to have a larger influence on the variation between simulated and measured efficiencies.

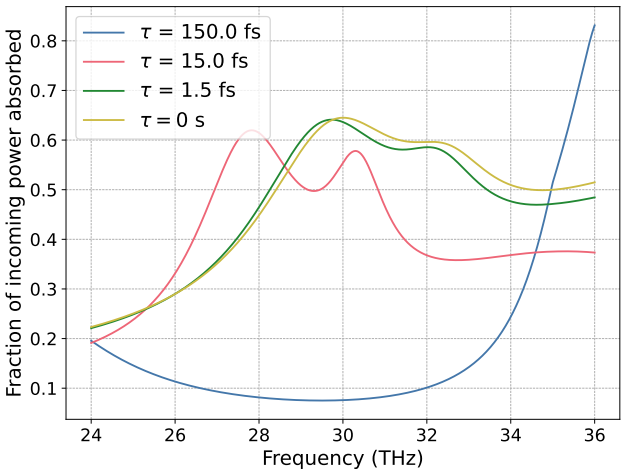

Figure 3.6: The effect of the mean free time between electron collisions,τ, on the average absorption efficiency for broadside incidence of the $10\,\mu\mathrm{m}$ (30 THz) absorber design. This effect is simulated in CST with the conductivity described by the Drude model in equation 2.15. The expected value for τ is 15 fs and is obtained using the free electron model The other τ values show the sensitivity of the absorption efficiency to variations in τ.

4

Kinetic Inductance Detector Design and Performance

Previously, we discussed the theory behind KIDs and absorbers in chapter 2 and designed an absorber in 3 . In this chapter, we will design the rest of the KID.

A KID behaves as a classical LC-resonator. In this resonator, the absorber will act as an inductive load to the resonator. Each KID needs to have its own resonance frequency within the readout band. The absorber parameters are set as varying the absorber will most likely decrease the performance of the absorber. Therefore, we will use a transmission line to tune the resonance frequency. In this chapter, this tuning will be discussed, along with the effect of a backshort and current inhomogeneities on the resolving power of KIDS.

4.1. Resonance frequency tuning

The KID consists of two parts: The absorber structure with the inductive load and a CPW. The CPW is coupled to the readout line. However, the coupling to the readout line is assumed to have no effect on the impedance of the resonator. A schematic overview of a CPW-absorber KID is shown in figure 4.2. The CPW has an input impedance $Z_{\text{CPW,in}}$, and the absorber has an input impedance of $Z_{\text{abs,in}}$.

As previously said, a CPW is used for the tuning. This is because CPWs don't need a lossy dielectric to work, so high quality factors of a few million can be achieved [36]. Figure 4.1 shows a CPW structure consisting of a center line of width S and a gap between the center line of the ground plane with width W.

The CPW will be made from a superconducting material that is different from the absorber's. This type of KIDs is called Hybrid KIDs. For the absorber, a superconducting material with a very low energy gap and, thus, high sensitivity aluminum is used. The connected CPW is most sensitive to TLS losses and noise [16]. Therefore, a superconductor with low noise is used for the CPW. In this thesis, the CPW

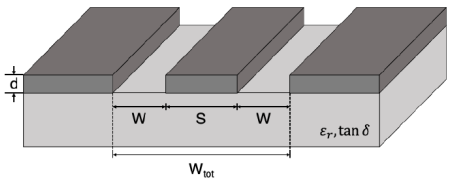

Figure 4.1: A co-planar waveguide. It consists of one central line and two ground planes on the side, each with a thickness of d. The width of the central line is defined by the parameter S. W is the gap width between the central line and the ground plane. The total width of the CPW (the distance between the two ground planes is W_{tot}.The relative permittivity ϵ_r and the loss tangent $\tan\delta$ are defined by the material of the substrate underneath the CPW. In Appendix chapter A a full derivation can be found for the characteristic impedance Z_{CPW} and the phase velocity v_p of a CPW. Figure from [37]

will be made from the low-noise superconductor NbTiN. The combination of NbTiN and Aluminum as superconducting materials has another advantage. There is a large difference in the gap energy of both materials (90 GHz vs 1.1 THz). This results in the quasiparticles being confined in the sensitive Aluminum [16].

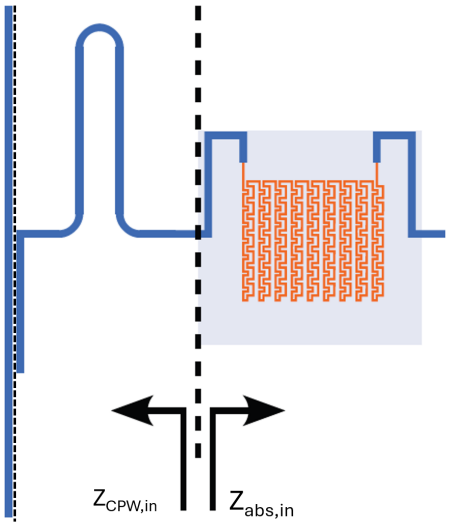

Figure 4.2: A schematic overview (not to scale) of a KID with an absorber as an inductive load to the CPW. The input impedance of the absorber is set due to the optimization of the absorber for optical coupling. The CPW will be used to tune the resonance frequency. The CPW has an input impedance $Z_{\text{CPW,in}}$, and the absorber has an input impedance of $Z_{\text{abs,in}}$. The coupling between the CPW and readout line is assumed to have no effect on $Z_{\text{CPW,in}}$ and is thus not taken into account. This figure is adapted from [15].

Since the imaginary part of the impedance must be zero at the resonance frequency, it follows that we to tune the CPW such that: $\text{Im}\left(Z_{\text{Abs,in}}\left(f_{\text{KID}}\right)\right) = -\text{Im}\left(Z_{\text{CPW,in}}\left(f_{\text{KID}}\right)\right)$

In this formula, $Z_{\text{CPW,in}}$ and $Z_{\text{Abs,in}}$ are the input impedance, respectively, of the CPW and the absorber. One must bear in mind that the readout of the absorber is in the order of a few GHz. This frequency is below the gap frequency of the aluminum. Therefore, the conductivity is described by the Mattis-Bardeen theory. $Z_{\text{abs,in}}$ thus has a completely different value at GHz than at THz (as mentioned for the incoming radiation in the context of absorbing radiation) and must not be confused.

Using transmission line theory, the CPW input impedance can be expressed as [15]:

$$Z_{\text{CPW,in}} = Z_{\text{CPW}} \frac{Z_L + jZ_{\text{CPW}} \tan\left(\frac{2\pi fl}{v_p}\right)}{Z_{\text{CPW}} + jZ_L \tan\left(\frac{2\pi fl}{v_p}\right)} \tag{4.1}$$

In this formula, Z_{CPW} is the characteristic impedance of the CPW, Z_L is the load at the end of the CPW, v_p is the phase velocity, and l is the length of the CPW. In this thesis, the CPW is open at the end, resulting in $Z_l = \infty$. This can be applied to the previous equation to get [15]:

$$Z_{\text{CPW,in}} = Z_{\text{CPW}} \frac{1}{j\tan\left(\frac{2\pi fl}{v_p}\right)} = -jZ_{\text{CPW}} \cot\left(\frac{2\pi fl}{v_p}\right) \tag{4.2}$$

Now, the resonance condition can be applied ($\text{Im}\left(Z_{\text{Abs,in}}\left(f_{\text{KID}}\right)\right) = -\text{Im}\left(Z_{\text{CPW,in}}\left(f_{\text{KID}}\right)\right)$) to rewrite the formula for an expression for the length l [15]:

$$l = \frac{v_p}{2\pi f_{\text{KID}}} \cot^{-1}\left(\left(\frac{\text{Im}\left(Z_{\text{abs,in}}\right)}{Z_{\text{CPW}}}\right)\right) \tag{4.3}$$

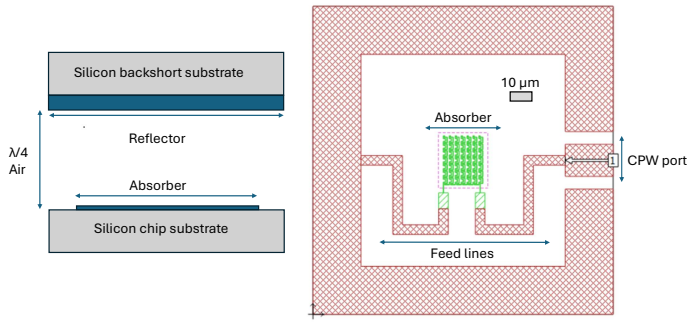

Figure 4.3: The simulation setup in SONNET. On the left, simulation stratification is shown with reflector and absorber on two separate chips separated by a $\lambda/4$ air distance. The material of the substrate for both chips is silicon. The figure shows the setup of the main chip. The aluminum absorber, which is connected to feed lines, is shown in green. The NbTiN of the ground plane and the feed lines are shown in red. The simulation used one port (port 1) at the end of the CPW. The edge of the aluminum backshort in the top silicon layer is shown as a red dashed line. We use a CPW with $S = 10\,\mu\mathrm{m}$ and $W = 6\,\mu\mathrm{m}$ in the KID.

The length of the CPW l is now expressed as a function of a single set parameter $Z_{\text{Abs,in}}$, two parameters specific to the CPW (Z_{CPW} and v_p), and the chosen resonance frequency f_{KID}. In Appendix A, a full derivation can be found for the characteristic impedance Z_{CPW} and the phase velocity v_p of a CPW. We will use a CPW with $S = 10\,\mu\mathrm{m}$ and $W = 6\,\mu\mathrm{m}$ in the KID. The readout line is a CPW with $S = 20\,\mu\mathrm{m}$ and $W = 8\,\mu\mathrm{m}$.

The input impedance of the absorber $Z_{\text{Abs,in}}$ can be found using a simulation in SONNET. The resulting simulation setup can be found in figure 4.3. We simulate the aluminum absorbers for microwave readout frequencies (GHz order). The absorber structure is connected with NbTiN feedlines to the ground plane and a port resembling the CPW's end. All are on a silicon substrate with a layer of air on top. Above the layer of air is another layer of silicon, which represents the substrate of the backshort chip. On this backshort chip, a 100 nm aluminum square was added as a $\lambda/4$ backing reflector.

Figure 4.4 shows the resulting input impedance of the absorber (as Al and PEC) and CPW for the center frequency KID of the fabricated chips. The intersection of the input impedance of the absorber and CPW gives the resulting resonance frequency of the KID. More detail on the chip design can be found in 5. The absorber is simulated as PEC and Al for kinetic inductance fraction estimate described in section 4.2.

4.2. KID sensitivity

Based on the designs, the expected pulse height of the KID θ can be estimated to evaluate its sensitivity to single-photon detection. We can do this by rewriting equation 2.13 to a simpler form. We do this by substituting equations 2.3 and 2.9 in equation 2.13 and taking the limit of T to zero. This results in the following expression of the change in angle $\delta\theta$ as a function of the change in the number of quasiparticles δN_{qp}:

$$\delta\theta = \frac{\alpha_k \beta Q}{2VN_0\Delta}\delta N_{qp} \tag{4.4}$$

The energy of the incoming photon is known as we know the wavelength: $E_{ph} = \frac{hc}{\lambda}$. This means that we can calculate the number of generated quasiparticles via the following equation:

$$\delta N_{qp} = \frac{\eta_{pb} E_{ph}}{\Delta} \tag{4.5}$$

Here, η_{pb} is the pair-breaking efficiency. It describes the fraction of the absorbed energy converted into excited quasiparticles during downconversion. The maximum pair breaking efficiency that one can achieve is: $\eta_{pb} = 0.59$ [38, 39].

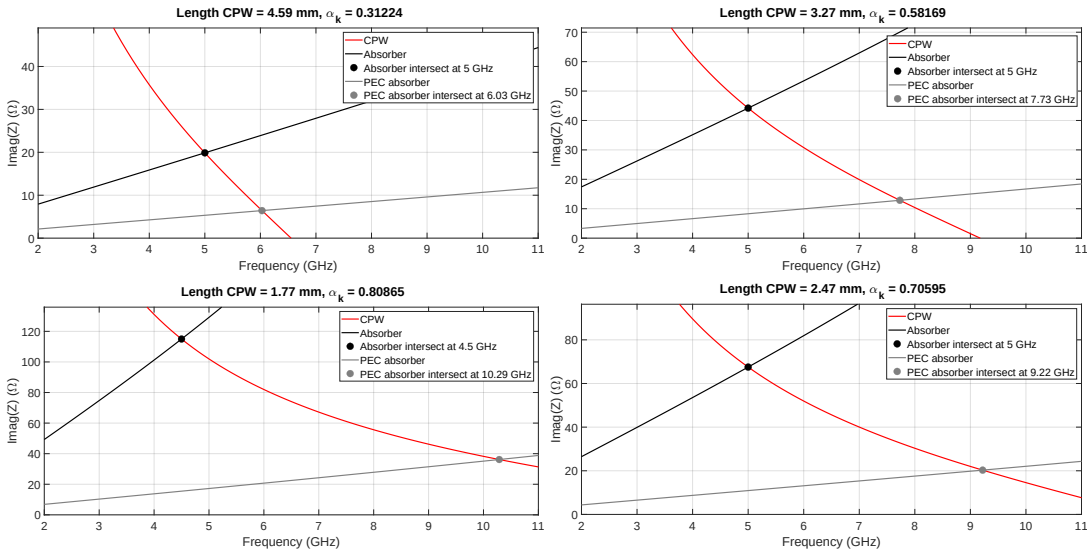

Figure 4.4: The simulated input impedance of the absorber (both as Al and as PEC) and the CPW input impedance as a function of frequency for different designs made in this thesis. Both impedances plotted are the imaginary part. The impedance of the CPW is mainly capacitive; thus, $-\mathrm{Im}(Z_{CPW})$ is plotted. In the title of each subfigure, the length of the NbTiN CPW and the kinetic inductance fraction α_k is shown, which can be calculated with equations 4.3 and 4.6 respectively. The data used is the data of the center frequency KID of each chip. The chip designs are discussed in 5. **Top left:** $10\,\mu\mathrm{m}$ KID with a 3x3 unit cell absorber. **Top right:** $10\,\mu\mathrm{m}$ KID with a 5x5 unit cell absorber. **Bottom left:** $18.5\,\mu\mathrm{m}$ KID with a 5x5 unit cell absorber. **Bottom right:** $18.5\,\mu\mathrm{m}$ KID with a 7x7 unit cell absorber.

All the variables of equation 4.4 can be found or calculated easily except α_k. However, the kinetic inductance fraction can be calculated for transmission line resonators like the ones presented in this thesis. For this, we need to replace the aluminum of the absorber with a PEC in the SONNET simulation. Then, the difference in resonance frequency can be used to find α_k:

$$\alpha_k = 1 - \delta F^2 \tag{4.6}$$

$$\text{where } \delta F = \frac{f_{Al}}{f_{PEC}} \tag{4.7}$$

Appendix B contains a full derivation for these equations.

Now, the peak heights can be calculated. We use $N_0 = 1.08 \cdot 10^{47}\mathrm{m}^{-3}\,\mathrm{J}^{-1}$ [12]. We estimate η_{pb} for a thin Al film on a Si substrate by calculating the phonon escape time $\tau_{\text{esc}} = 0.053$ ns from the film thickness using [40]. Extrapolating the η_{pb} data from [41] with the value for τ_{esc} we find $\eta_{pb} \approx 0.15$. Using these values, we calculated the peak heights as shown in table 4.1.

Table 4.1: The expected peak heights for the different KID designs. The following parameters are used as input for equations 4.4 and 4.5 : $N_0 = 1.08 \cdot 10^{47}\mathrm{m}^{-3}\,\mathrm{J}^{-1}$ [12], $\eta_{pb} = 0.15$ [40] [41], $Q = 40 \cdot 10^3$ and T_c= 1.3 K.

KID Design	$E_{ph}(eV)$	α_k	$V(\mu m^3)$	θ (rad)
Design 1 : 18.5 μm large absorber	0.0670	0.81	4.00	0.12
Design 2 : 18.5 μm small absorber	0.0670	0.71	2.04	0.21
Design 3 : 10 μm large absorber	0.1240	0.58	0.86	0.75
Design 4 : 10 μm small absorber	0.1240	0.31	0.31	1.11

4.3. (Noise) Limitations on the KID resolving power

KIDs have an inherent energy-resolving ability. An incoming photon creates a large number of quasiparticles. From the peak height shown in equation 2.10, the photon's energy can be calculated. However, multiple noise processes and inhomogeneities cause a spread in the number of generated quasiparti-

cles. The measure of this spread versus the actual photon energy is defined as the resolving power of the KID, R:

$$R = \frac{E}{\delta E} \tag{4.8}$$

Here, E is the photon's energy, and δE is the spread of energies due to varying responses. R can be determined from a histogram of the data. The data is assumed to follow a Gaussian distribution with E being the average of the distribution and δE being the full-width half maximum (FWHM). The resolving power can be split into different parts. Since we are adding variances, contributions to the resolving power need to be added as follows:

$$\frac{1}{R^2} = \sum_n \frac{1}{R_n^2} \tag{4.9}$$

The rest of this section discusses the different causes for a spread in δE. Firstly, we will address factors contributing to the signal-to-noise resolving power, R_{SN}, that describes how well the energy can be determined due to noise fluctuations. These contributions are from the two-level system noise, the amplifier noise, and the generation-recombination noise. Afterward, we will address downconversion losses. Current inhomogeneities, including their effect on the resolving power of absorber-based KIDs, are discussed in section 4.5. We don't discuss generation recombination noise [42] as it is not observed in the measurements in this thesis.

4.3.1. Two level system noise

The KID is made on a dielectric layer, which, in our case, is silicon. There is often an oxide layer on the KID or the interface of the KID and dielectric. In these and other amorphous layers, two-level systems (TLS) exist. A TLS is an atom in a system of two minima in a double-well potential. Due to the low temperature ($T \leq T_c$) and the KID's electric field, the atom's tunneling is driven between these two minima. This results in a time-varying dielectric constant, which occurs as noise mainly in the phase response of the KID [4]. For the typical temperatures in the cooler, the TLS noise scales with the inverse of temperature squared, thus $\propto 1/T^2$, and the inverse square root of the internal power: $P_{int}^{-1/2}$ [22]. One can use non-oxidizing materials to minimize TLS noise in the system.

4.3.2. Generation recombination noise

Previously, it was assumed that the photons from the source are the only cause of excess quasiparticles. However, this is not true; other sources cause the breaking of Cooper pair and creation of quasiparticles, such as thermal phonons from the superconductor and its surroundings [4, 42]. The arrival of thermal phonons is not constant, and there will be a fluctuation in the number of quasiparticles in the system. This fluctuation is called the generation recombination (GR) noise.

4.3.3. Amplifier noise

Another noise source is found in amplifiers and attenuators in the readout system. This noise is white and given by [18]:

$$S_{A,\theta}^{system} = \frac{k_b T_{sys}}{r_c^2 P_{read}} \tag{4.10}$$

Here, k_b is the Boltzmann constant, T_{sys} the equivalent noise temperature of the system and $r_c = \frac{Q}{2Q_c}$. For the overcoupled KIDS in this thesis, $r_c = 0.5$. Moreover, P_{read} is the readout power of the system.

4.3.4. Downconversion losses

Not all the energy of the photons is used to break Cooper pairs. A part of the energy is lost during the electron and phonon interactions in the downconversion process. This is because electrons and phonons will receive energy from the excess energy of the photon in comparison with the Cooper pair. Not all electrons and phonons will have energies larger than the bandgap. The energy of these electrons and phonons is lost.

The downconversion processes are all statistical, resulting in a variation of the energy lost during downconversions. The average fraction of the absorbed energy that is converted in creating quasi-particles is the pair-breaking efficiency, η_{pb}. The maximum value for the pair breaking efficiency in Al is $\eta_{pb} = 0.59$ [38, 39]. The limit on the resolving power due to the statistical variation in ηpb is the Fano limit [43], R_{Fano}:

$$R_{\text{Fano}} = \frac{1}{2\sqrt{2\ln(2)}}\sqrt{\frac{\eta_{pb}E_{ph}}{\Delta F}} \tag{4.11}$$

Here F is the Fano factor, which is ≈ 0.2. The Fano limit, however, assumes an ideal case with no phonons escaping the superconductor. In reality, phonons can escape the KID and this energy is lost. These losses increase the variation in converted energy and reduce the statistical Fano limit. To account for this, we must add a material and geometry-dependent factor J in equation 4.11. The result is the following R due to downconversion statistics and phonon losses [44]:

$$R_{\text{phonon}} = \frac{1}{2\sqrt{2\ln(2)}}\sqrt{\frac{\eta_{pb}E_{ph}}{\Delta(F+J)}} \tag{4.12}$$

4.4. Backshort etch

The backshort is made on another chip and is connected to the main chip via a Perminex layer with a thickness of $\lambda/4$, as discussed in chapter 5. The backshort chip is made on a silicon substrate. Since our wavelengths are small, the distance between the two chips is also very small ($\lambda/4$ is $2.5\,\mu\text{m}$ and $4.63\,\mu\text{m}$ in our case). This means that an additional silicon layer is present close to the CPW. The surface of silicon can contain an amorphous layer of oxides. This layer of oxides can introduce TLS noise [45] and a shift in resonance frequency.

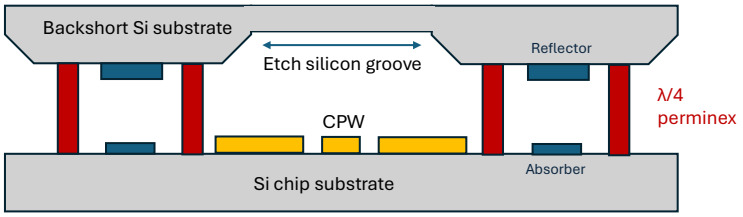

Figure 4.5: The main and backshort chip with the groove above the CPW highlighted.

The power spectral density (PSD) of the TLS noise, S, can be described by the following equation [46]:

$$\frac{S}{f_r^2} = \frac{\kappa(\nu, f, T)}{4E_s l}\frac{t\int \frac{|E|^4}{\sqrt{1+|E|^2/E_s^2}}ds}{W'^2} \tag{4.13}$$

This equation uses the assumption that the electric field inside the field strength is thickness-independent. In this equation, κ is a material-dependent parameter found empirically. It is a function of the operating frequency ν, the readout frequency f, and temperature T. E_s in equation 4.13 is the saturation field value. l is the length of the CPW resonator and t is the thickness of the TLS layer. s, the parameter over which is integrated, is the width parameter in the dielectric above the CPW. Lastly, W' is the total electric energy stored in the system: $W' = \frac{\int \varepsilon |E|^2 dA_{\text{system}}}{2}$. From this equation, we can see that we can reduce the TLS noise by reducing the electric field strength E in the silicon surface. Therefore, it was decided to make a groove in the silicon of the backshort chip above the CPW to remove these effects. This is shown in figure 4.5.

Equation 4.13 can be simplified for our use. If we take the limit of a large E-field and assume that the total energy stored in the system W does not change, the following relation can be found for the PSD

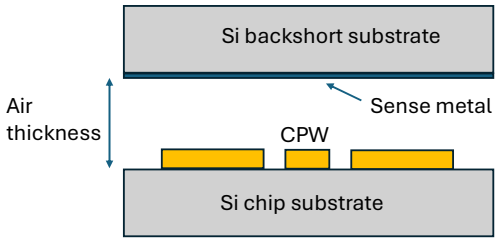

Figure 4.6: The location of the Sense metal at the surface of the silicon backshort substrate right above the CPW. We vary the air thickness in the simulations.

and the field TLS volume: $\frac{S}{f_r^2} \propto |E|^3$. So now, the TLS noise can be related to the strength of the electric field at the silicon surface. This can be simulated in SONNET using a sense metal. A sense metal is a special metal in SONNET that allows us to simulate the tangential component of the electric field. This is done in the following way: The sense metal is a special layer that allows us to measure current. We can choose the reactance of the sense metal. The reactance of the sense metal is set to a very high value such that it does not affect the electric field in the KID or create resonances. Then, the electric field can be calculated via Ohm's law: $E = \chi J$. Here, E is the electric field, χ is the reactance (Ω) and J is the current density in the sense metal ($\mathrm{A\,m^{-1}}$). In this simulation, the thickness of the air layer between the CPW and silicon surface, d_{air}, is varied, giving different field distributions. Figure 4.7 shows two examples of the current distribution for various air distances between the silicon and the CPW.

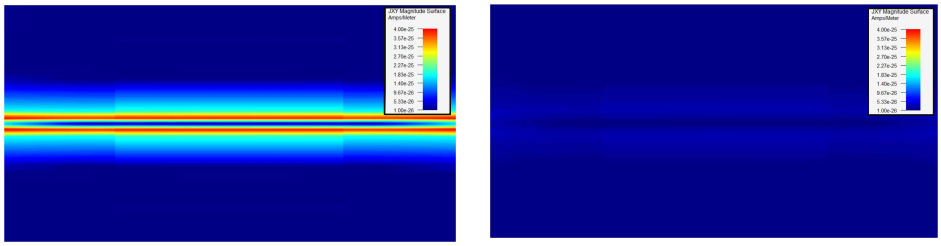

Figure 4.7: Current distribution at the surface of the silicon of the backshort chip for a CPW with a center line width of $10\,\mu\mathrm{m}$ and a gap between the center line and ground plane of $6\,\mu\mathrm{m}$. This configuration is used for the KIDs made in this thesis. **Left:** The current density on the Si surface for a layer of air of $2.05\,\mu\mathrm{m}$ between the CPW and silicon of the backshort. **Right:** The current density on the Si surface for a layer of air of $16\,\mu\mathrm{m}$ between the CPW and silicon of the backshort.

The results of the normalized field strength are shown in the left panel of figure 4.8. The simulations are done with a reactance of $\chi = 3 \cdot 10^{16}\Omega/sq$. The resulting currents in the sense metal are summed and then normalized by the data point for the smallest air thickness between the slabs (d_{air}). This data point is at $d = 1\,\mu\mathrm{m}$. It is the smallest thickness that still gives the expected current distribution of the CPW. Therefore, this point is considered the field value immediately above the CPW and is used to normalize the other data points.

The simulated electric field values can be coupled to the extra noise due to the backshort chip via the known proportionality between noise and field and a measurement of the extra TLS noise due to extra silicon above the CPW. This measurement gave an extra TLS noise contribution of 10dB for a 6-10-6 CPW with an air thickness between the CPW and the silicon of $1\,\mu\mathrm{m}$ [47]. The resulting excess noise due to the electric field in the Si backshort chip is shown in the right panel of figure 4.8

The simulations are performed for CPW with four different parameters. The first parameter set is used for the CPWs in this thesis. These CPWs have a gap width of $6\,\mu\mathrm{m}$ between the central plane and the ground plane and a central plane width of $10\,\mu\mathrm{m}$. These will be called 6-10-6 CPW. The other types

of CPWs are the 8-20-8, a very commonly used CPW, and the 2-3-2 and the 40-24-40. The last two are the, respectively, smallest and largest CPWs that are in a database of SRON for the KID (mask) generation software.

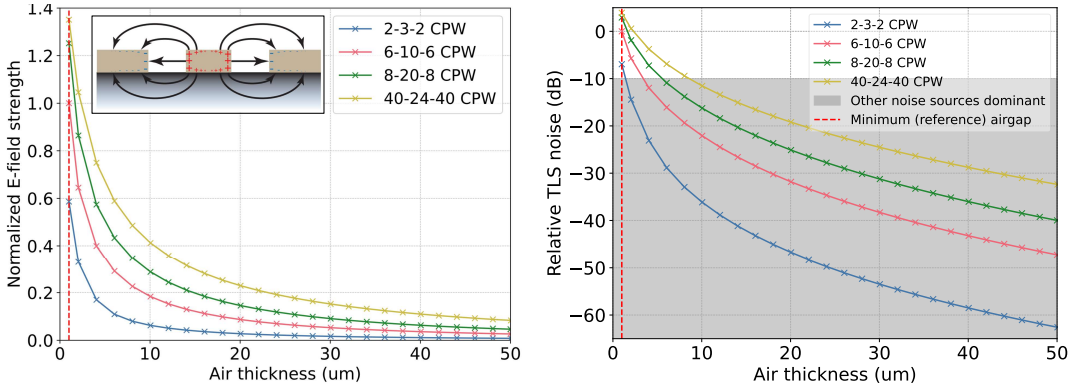

Figure 4.8: Comparison of the field strength at the surface of the silicon of the backshort chip and the excess noise due to the backshort chip for different CPW geometries. A 2-3-2 CPW means a center line width of $3\,\mu\mathrm{m}$ and a gap between the center line and the ground plane of $2\,\mu\mathrm{m}$. **Left:** The field strength at the surface of the silicon of the backshort chip as a function of the thickness of the air between the backshort chip and main chip. The data is normalized by a data point for which an excess noise measurement exists [47]. The field distribution insert is adapted from Hänhle[48]. **Right:** The relative extra TLS noise caused by the silicon backshort chip. The reference is a measurement on an antenna KID with a CPW by Jochem Baselmans of 10 dB excess TLS noise at $1\,\mu\mathrm{m}$. This means that we choose a depth such that the TLS is reduced by 10 dB or more so that it is no longer the dominant noise source.

Figure 4.8 shows that smaller CPWs have a lower field strength in the silicon. As a result, TLS noise is lower for smaller CPWs. The simulation resulted in the decision to set d_{groove}=$10\,\mu\mathrm{m}$. This is the depth of the etch in the silicon backshort chip. The total distance between the silicon of the backshort chip and the CPW is $\lambda/4 + d_{\text{groove}}$.

All except 5 KIDs will have a groove in the backshort chip above the CPW in the chips fabricated for this thesis. This aims to test and verify the effect of the backshort (groove) on the noise and resonance frequency of the KID. The 5 KIDs without grooves are the KIDs with the 5 lowest resonance frequencies, as the backshort is expected to lower the resonance frequency.

4.5. Effect of current inhomogeneity on the resolving power of absorber KIDS

4.5.1. Theory

Current inhomogeneity in aluminum can also limit resolving power. To derive this, we need to look at the resonator differently than before, as the response dependence on the local current is not so trivial from the derivation shown in section 2.2. To derive the dependence on the current, we need to use the perturbation theory. Perturbation theory is widespread and has its best-known applications within quantum mechanics. It yields an approximate solution to a problem by splitting the problem into a simple, analytically solvable part and a small change to the system (the perturbation). In this derivation, the resonator at resonance frequency is the base solution, and the change in kinetic inductance due to an absorbed photon is the perturbation.

The complete derivation using the perturbation theory is presented in chapter C. The outcome of this derivation allows us to express the shift in resonance frequency as a function of the energy stored in the electric and magnetic fields, denoted by W_e and W_m, respectively [49]:

$$\frac{\omega - \omega_0}{\omega_0} = \frac{\Delta W_m - \Delta W_e}{W_m + W_e}. \tag{4.14}$$

Here, ΔW_m and ΔW_e represent the changes in magnetic and electric field energy due to the perturbation, respectively. The response dependence on the current can be found in equation 4.14. For this,

we need to realize that $\frac{\omega-\omega_0}{\omega_0}$ is proportional to the response $\delta\theta$ and that only the (kinetic) inductance changes, meaning that $\Delta W_e = 0$. So, the response only depends on W_m. Kouwenhoven [18] found an expression for the change in stored energy, W_m, as a function of the change in the kinetic inductance at the resonance frequency in a 1D situation:

$$\Delta W_m = \int_{l_1}^{l_2} \delta L_k(l) \left| I_{\text{max}}(l) \right|^2 dl \tag{4.15}$$

In this equation, l_1 and l_2 are the integration bounds for the length, $\delta L_k(l)$ is the location-dependent change in kinetic inductance, and $I_{\text{max}}(l)$ is the location dependent current during resonance. We use a 1D situation as an approximation, as the length of the aluminum lines is large compared to the width.

By combining equation 4.15, which shows that the stored energy scales with I^2_{max}, and equation 4.15, it follows that the KID response scales with $I_{\text{max}}(l)^2$.

After the photon hits the absorber, quasiparticles will be generated. During the time that the resonator needs to respond to a change in impedance, called the ring time, $t_{\text{ring}} = \frac{2Q}{\omega_r}$, the quasiparticles will diffuse. The distance that quasiparticles travel during diffusion, known as the diffusion length, determines the integration bounds of equation 4.15. As a result, if the distance over which the current varies significantly is smaller than the diffusion length, the response will be almost uniform, whereas a larger variation distance causes the response to depend on the location of the photon incidence.

The diffusion constant, D, must first be known to calculate the diffusion length. It can be calculated using the Einstein equation[50]:

$$D = \frac{1}{2e^2 \rho N_0} \tag{4.16}$$

In this equation, e is the electric charge of an electron, ρ is the normal DC resistivity, and N_0 is the single spin density of states at the Fermi level. N_0 can be found in literature for aluminum: $N_0 \approx 1.08 \cdot 10^{47} m^{-3} J^{-1}$[12].

We can define the diffusion distance now that we have defined the ring time t_{ring} and the diffusion constant D. The diffusion distance is the distance the created quasiparticles travel during the ring time:

$$d_{\text{diffusion}} = \sqrt{t_{\text{ring}} D} \tag{4.17}$$

4.5.2. Simulation

The current inhomogeneity in the absorber part of the KID is simulated in SONNET. The setup of the simulation is shown in figure 4.9. In this simulation, a $18.5\,\mu\text{m}$ KID design is simulated with a 23 nm thick aluminum absorber with 7x7 unit cells in the absorber. The KID simulated here is the KID with the center frequency of chip design 1. The resonance frequency of this KID is 4.5 GHz. The chip designs are discussed in chapter 5.

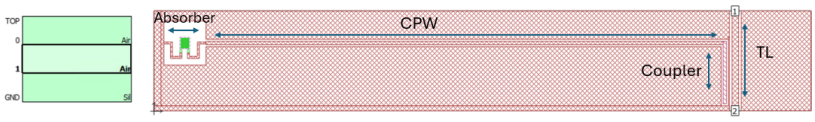

Figure 4.9: The simulation setup in SONNET. The green structure is the aluminum absorber part of the KID. The red part is the NbTiN in the KID. The CPW, transmission line (TL), and coupler are all NbTiN. On the left, the stratification is shown.

The simulation is very similar to the simulation setup in figure 4.3. There are two large differences compared with the previous simulation. The first change is that the full KID is simulated here as we want to find the current distribution at the resonance frequency of the KID. To find these currents, we need to simulate the full KID as there are also currents in the CPW that influence the currents in the absorber. The other large difference is the stratification of the backshort. The stratification of the

backshort is set to air in the current simulation. This is done as a groove will be made in the silicon of the backshort to reduce TLS noise and a shift in resonance frequency. This is discussed in detail in section 4.4.

However, the large size of the whole structure and the small mesh size needed to keep the shape of the absorber correct made it impossible to run the SONNET simulation due to the large memory required. Therefore, we choose the dimensions of the absorber such that the width of the absorber lines and the spacings in between match the grid size. We choose 250 nm as the grid size, the smallest size possible without memory issues. This means that the simulated design slightly varies from the presented $18.5\,\mu\mathrm{m}$ design.

Figure 4.10 shows the resulting current density. There are no large variations within the absorber except for the higher current density in the sharp corners of the absorber due to current crowding effects [51, 52]. However, the current crowding is so local, compared to the total area that quasiparticles can reach due to diffusion, that it will not affect the resolving power.

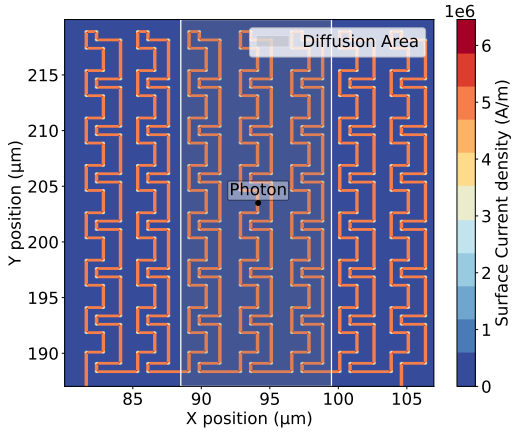

Figure 4.10: The distribution of the current density in the aluminum absorber part of the KID sampled with steps of $0.05\,\mu\mathrm{m}$ in both the x and y direction. There are no large variations within the absorber unit cells except for current crowding in the corners. In the figure, the area quasiparticles can reach due to diffusion for a photon absorbed in the middle of the absorber is highlighted in gray.

However, diffusion can still influence the resolving power of KIDs. As shown in figure 4.3, parts of the feed lines are made of aluminum. The aluminum of the feedline is extensive compared to the absorber lines, resulting in a low current density. This means that the response is lower in that case as the response scales with the local current squared as shown in equation 4.15, causing an extra variation in peak heights.

We model this effect with the same setup as before in 6.1. In this case, we are only interested in the current density as a function of the length of the line $I(l)$, as diffusion mainly occurs in that dimension. Therefore, we change the distance between points in the current data from $0.05\,\mu\mathrm{m}$ to $0.25\,\mu\mathrm{m}$, which is precisely the width of the lines and the spacing between the lines. As a result, we only have one data point over the width of the line. This means we have simplified the two-dimensional current data $I(x, y)$ to a 1D current that is a function of length: $I(l)$.

In the model, we start with the absorption of photons. The absorption pattern is modeled via an Airy pattern originating from the center of the lens aperture focused at the center of the absorber directly beneath it. The intensity I is then given as[53]:

$$I = \left(\frac{2J_1(ka \sin\theta)}{ka \sin\theta} \right)^2 . \tag{4.18}$$

Here, J_1 is the first-order Bessel function of the first kind, k is the wavenumber, and a is the radius of the lens aperture. θ is the observation angle, which means the angle between the axis going through

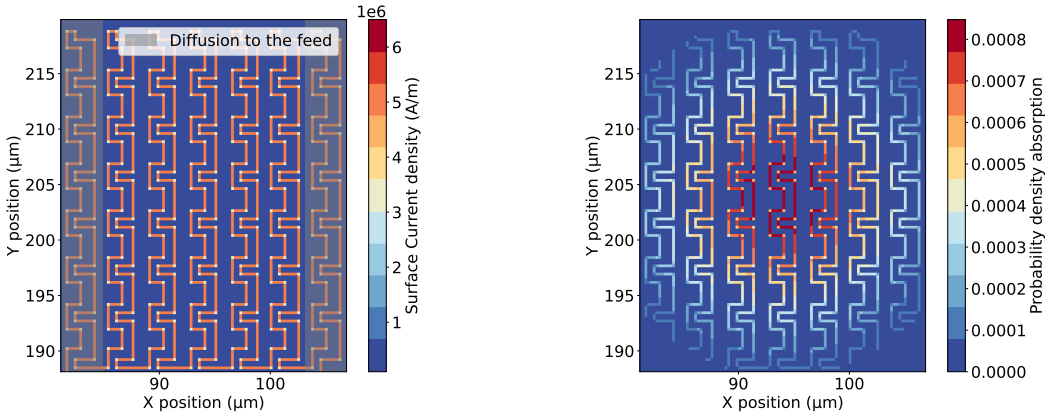

Figure 4.11: The data used to estimate the resolving power due to quasiparticle diffusion to the feed. **Left:** The current density within the absorber with a sample distance of 0.250 nm resulting in 1 sample point over the width of the line. This 1D current data is used for estimations of the resolving power. The bars at the edge of the figures illustrate the zone where a lot of quasiparticles will diffuse to the feed after photon absorption. **Right:** Probability density function for photon absorption, obtained by normalizing the Airy pattern intensity from the lens over the absorber structure. The total integrated probability across all absorber lines equals one.

the lens's aperture's center and the line connecting the position of interest on the absorber and the center of the aperture.

Figure 4.11 shows the absorption probability for photons together with the resulting current density.

We will use the same mesh as the current density for the absorption of the photons so that the photon is now at a location l. From this location, we calculate the minimum and maximum positions to which quasiparticles can diffuse, which are $l_{\text{min}} = l - d_{\text{diffusion}}$ and $l_{\text{max}} = l + d_{\text{diffusion}}$. After this, we integrate $I(l)^2$ to find the response as described in equation 4.15 with l_{min} and l_{max} as integration boundaries. This implies that we assume that quasiparticles form a uniform distribution and the kinetic inductance is constant: $L_k(l) = L_k$.

We also need to consider boundary conditions, as photons may be absorbed close to the start or end of the absorber. In that case, l_{min} can be smaller than zero, and l_{max} may be larger than the total length of the absorber. The areas where this is true are highlighted in the left panel of figure 4.11. In this simulation, we will consider two boundary conditions:

1. Quasiparticles stay in the absorber. They see a hard wall at the end and can not enter the feed. Again, we use that a constant L_k. This means that we need to compensate for the location of incidence: When a photon is absorbed closer to the boundary of the absorber, the corresponding integration interval is shorter. In contrast, photons absorbed in the middle have a longer segment over which the response is integrated. To account for this variation in the interval length, we divide the integral by the integration interval length. This effectively means that we average $I(l)^2$.
2. Quasiparticles can leave the absorber and enter the aluminum part of the feed. Here, we assume the feed lines do not contribute to the integration. This is valid as the current density in the feed is a factor 100 lower than in the absorber, and the response scales with the current density squared. In this situation, we will thus change l_{min} to zero if $l_{\text{min}} < 0$ or l_{max} to the length of the absorber if l_{max} is larger than the length of the absorber.

The integration will yield a distribution of integrated current. We change this distribution to one of θ by assigning the calculated peak height from section 4.2 to the median of the distribution. The other values of the distribution are scaled proportionally based on this median.

In the simulation, we estimate the resolving power by simulating the absorption of 1 million photons. The resulting histogram with resolving power for the first boundary condition, where quasiparticles stay in the absorber, is shown in figure 4.12. The resulting distribution is very narrow. However, the distribution is not Gaussian. As a result, we can not use a kernel density estimate. Therefore, we will use the worst

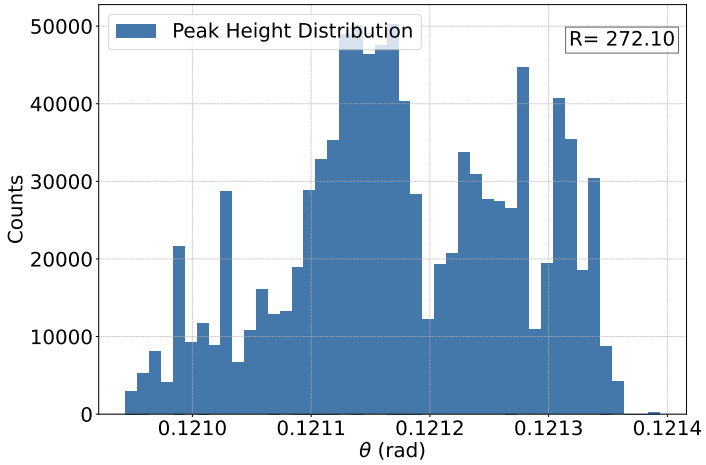

Figure 4.12: The resulting histogram due to current inhomogeneities within the absorber. The boundary condition is closed, i.e. quasiparticles stay in the absorber. We find a relatively narrow, non-Gaussian distribution. We use the lowest and highest values of θ for R due to the non-Gaussian shape. We find $R = 272.10$.

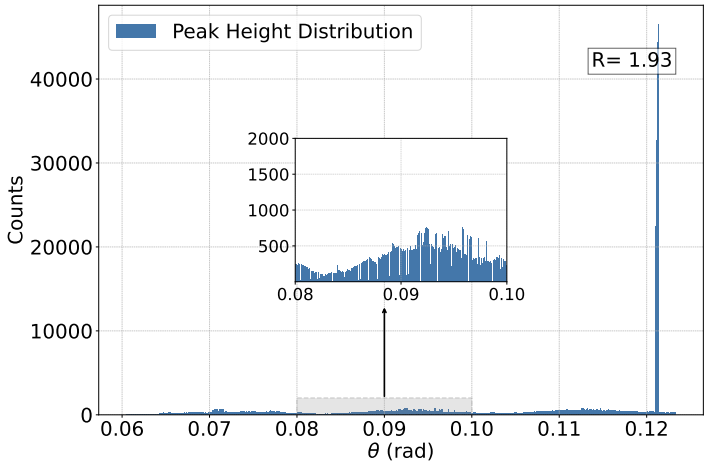

Figure 4.13: The resulting histogram due to current inhomogeneities within the absorber. The boundary condition is open, i.e., quasiparticles can leave the absorber. Quasiparticles in the wide part of the feed are assumed not to contribute to the response, due to the 100x lower current density in the feed. We find a narrow distribution of higher counts and a long tail of lower peak values. We use the lowest and highest θ to find R. We find a low resolving power of $R = 1.93$.

case scenario where δE is the difference between the minimum and maximum found difference in the simulation. From this, we find $R = 272.10$, which is large compared to other contributions, such as Fano statistics ($R_{\text{fano}} = \approx 6.8$), resulting in a non-significant contribution to the total resolving power.

Figure 4.13 shows the result for boundary condition 2, where quasiparticles can diffuse to the feed. The result is, again, a very narrow peak around the average expected peak height. However, due to the diffusion of quasiparticles to the feed, there is a uniform distribution of relatively low counts for lower peak heights. This reduces the resolving power drastically to $R = 1.93$.

However, many of these pulses have such low values that they get lost in the noise floor. Therefore, it is not good to look at these pulses as a resolving power but as a detection efficiency. This efficiency can be seen as a detection efficiency, $\eta_{\text{detection}}$. For this purpose, we look again at the simulation results in figure 4.14. To get an idea of how many pulses in the tail get lost, we will analyze the data again, but now we will consider a signal-to-noise resolving power to filter the data. We take a typical value of $R_{sn} = 5$. All peaks that fall outside $R_{sn} = 5$ are rejected in the analysis. The resulting histogram is shown in figure 4.14. We find a detection efficiency of 84%.

From this research, we conclude that current inhomogeneities within the absorber do not degrade the

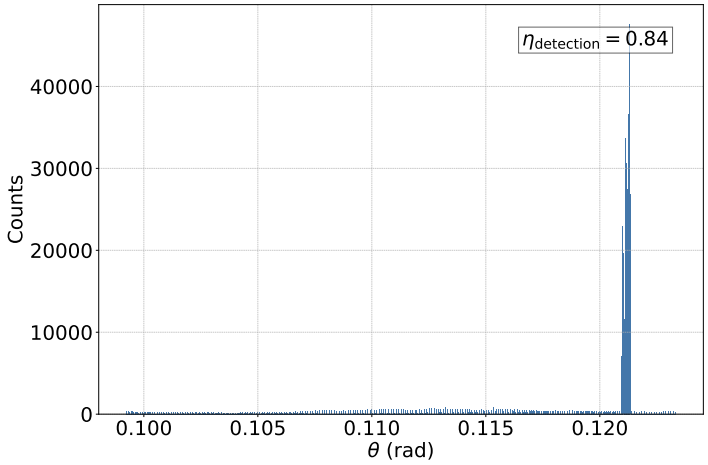

Figure 4.14: The resulting histogram due to current inhomogeneities within the absorber. The boundary condition is open, i.e., quasiparticles can leave the absorber. Quasiparticles in the wide part of the feed are assumed not to contribute to the response, due to the 100x lower current density in the feed. We find a relatively narrow distribution of higher counts and a uniform distribution of low counts for lower peak values. Here we analyze how many pulses in the tail are lost in the noise floor. For this, we consider a typical value for R_{sn} of 5. All counts outside this range are considered lost. Then we find an additional detector efficiency, $\eta_{\text{detection}}$ of 84%.

resolving power. We also conclude that the wide feed will lower the efficiency and resolving power of the detector. Future detectors should make the connecting Al feed as small as possible to avoid loss of quasiparticles or add an extra long, narrow line between the absorber and feed to ensure that all the quasiparticles will contribute to the response maximally.

5

Chip design and fabrication results

This chapter starts with an overview of the 4 different chip designs with their parameters. After this, we discuss the fabrication process. This chapter ends with the results of the fabrication.

5.1. Chip design overview

In this thesis, a total of 9 chips will be made from 4 different chip designs, 2 for each wavelength. Here, an overview of the different designs with the important parameters is added:

- **Design 1:** $18.5\,\mu\mathrm{m}$ **with larger absorber**
  - Absorber unit cells: 7×7
  - Absorber dimensions: $w_x = 2.4\,\lambda f_{\#} = 25.97\mu\mathrm{m}, \quad w_y = 2.7\,\lambda f_{\#}$= 29.68$\mu\mathrm{m}$
  - Backshort spacing: $\lambda/4$= $4.63\,\mu\mathrm{m}$
  - Backshort dimensions: $w_x = 40.97\mu\mathrm{m}, \quad w_y =$ 44.68$\mu\mathrm{m}$
  - Center frequency: 4.5 GHz (frequency range: 3.34 to 5.82 GHz)
  - Scaled frequency spacing: $\frac{\Delta f}{f} = 2 \times 10^{-2}$
  - Total number of KIDs: 25 (5x5 KID array hexagonally spaced with 0.75 mm pitch)
  - Designed quality factors (Q_c):
    - 40×10^3 (13 resonators, assigned to the lowest readout frequencies)
    - 100×10^3 (12 resonators, assigned to the highest readout frequencies)
  - CPW: $10\,\mu\mathrm{m}$ center line and $6\,\mu\mathrm{m}$ gap between center line and ground plane.
  - Readout line: $20\,\mu\mathrm{m}$ center line and $8\,\mu\mathrm{m}$ gap between center line and ground plane.
- **Design 2:** $18.5\,\mu\mathrm{m}$ **with smaller absorber**
  - Absorber unit cells: 5×5
  - Absorber dimensions: $w_x = 1.7\,\lambda f_{\#}$=$18.55\,\mu\mathrm{m}, \quad w_y = 1.9\,\lambda f_{\#}$=21.20$\mu\mathrm{m}$
  - Backshort spacing: $\lambda/4$= $4.63\,\mu\mathrm{m}$
  - Backshort size:$w_x = 33.55\,\mu\mathrm{m}, \quad w_y =$=36.20$\mu\mathrm{m}$
  - Center frequency: 5 GHz (frequency range: 4.34 to 5.69 GHz)
  - Scaled frequency spacing: $\frac{\Delta f}{f} = 1 \times 10^{-2}$
  - Total number of KIDs: 25 (5x5 KID array hexagonally spaced with 0.75 mm pitch)
  - Designed quality factors (Q_c):
    - 40×10^3 (13 resonators, assigned to the lowest readout frequencies)

        * 100×10^3 (12 resonators, assigned to the highest readout frequencies)
    - CPW: $10\,\mu\mathrm{m}$ center line and $6\,\mu\mathrm{m}$ gap between center line and ground plane.
    - Readout line: $20\,\mu\mathrm{m}$ center line and $8\,\mu\mathrm{m}$ gap between center line and ground plane.
- **Design 3:** $10\,\mu\mathrm{m}$ **with larger absorber**
    - Absorber unit cells: 5×5
    - Absorber dimensions: $w_x = 1.987\,\lambda f_{\#} = 11.75\mu\mathrm{m}, \quad w_y = 1.996\,\lambda f_{\#} = 11.80\mu\mathrm{m}.$
    - Backshort spacing: $\lambda/4$= $2.5\,\mu\mathrm{m}$
    - Backshort dimensions: $w_x = 26.75\mu\mathrm{m}, \quad w_y = 26.80\mu\mathrm{m}.$
    - Center frequency: 5 GHz (frequency range: 4.34 to 5.69 GHz)
    - Scaled frequency spacing: $\frac{\Delta f}{f} = 1 \times 10^{-2}$
    - Total number of KIDs: 25 (5x5 KID array hexagonally spaced with 0.75 mm pitch)
    - Designed quality factors (Q_c):
        * 40×10^3 (13 resonators, assigned to the lowest readout frequencies)
        * 100×10^3 (12 resonators, assigned to the highest readout frequencies)
    - CPW: $10\,\mu\mathrm{m}$ center line and $6\,\mu\mathrm{m}$ gap between center line and ground plane.
    - Readout line: $20\,\mu\mathrm{m}$ center line and $8\,\mu\mathrm{m}$ gap between center line and ground plane.
- **Design 4:** $10\,\mu\mathrm{m}$ **with smaller absorber**
    - Absorber unit cells: 3×3
    - Absorber dimensions: $w_x = 1.192\,\lambda f_{\#} = 7.05\mu\mathrm{m}, \quad w_y = 1.197\,\lambda f_{\#} = 7.08\mu\mathrm{m}.$
    - Backshort spacing: $\lambda/4$= $2.5\,\mu\mathrm{m}$
    - Backshort dimensions: $w_x = 22.05\mu\mathrm{m}, \quad w_y = 22.08\mu\mathrm{m}.$
    - Center frequency: 5 GHz (frequency range: 4.34 to 5.69 GHz)
    - Scaled frequency spacing: $\frac{\Delta f}{f} = 1 \times 10^{-2}$
    - Total number of KIDs: 25 (5x5 KID array hexagonally spaced with 0.75 mm pitch)
    - Designed quality factors (Q_c):
        * 40×10^3 (13 resonators, assigned to (lowest frequencies))
        * 100×10^3 (12 resonators, assigned to even KIDs (highest frequencies))
    - CPW: $10\,\mu\mathrm{m}$ center line and $6\,\mu\mathrm{m}$ gap between center line and ground plane.
    - Readout line: $20\,\mu\mathrm{m}$ center line and $8\,\mu\mathrm{m}$ gap between center line and ground plane.

The main variation between the chips is the number of unit cells of the absorber. The first reason for this is the fabrication limits. The risk of failed fabrication is especially high for the $10\,\mu\mathrm{m}$ design. Therefore, safer versions are made with fewer unit cells and thus less risk. This variation also gives us versions with a lower volume. These have a lower quantum efficiency but a higher responsivity. The higher responsivity increases the chance of being able to measure single photons. This is the second reason for this variation in the chip designs.

5.2. Fabrication process

All the designs consist of two chips: the main chip and the backshort chip. Figure 5.1 shows a general overview of the chip layers. The fabrication process consists of 13 steps, of which 4 are optional steps for the backshort. The fabrication steps are the following:

Full fabrication:

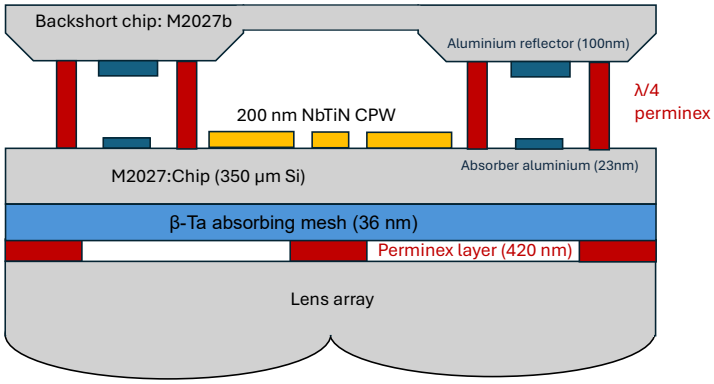

Figure 5.1: A not-to-scale overview of the different layers of the KID chips presented in this thesis. The bottom of the figure is a Lens array. The lens array is connected to a silicon substrate. The KID layers will be deposited on this substrate. Therefore, this will be called the main chip (M2027). The main chip is connected to the backshort chip via a $\lambda/4$ Periminex layer. On the backshort chip, a $\lambda/4$ aluminum backing reflector is placed.

1. **β-Ta backside**: We sputter deposit 36 nm β-Ta. We use photolithography and reactive-ion etching (RIE) to make the pattern. The impedance of β-Ta layer is matched such that the scattered THz radiation is absorbed and the GHz microwave readout is not affected[12]. The resulting pattern consists of β-Ta squares similar to the design shown in Baselmans et al.[54]. Obviously, there is no β-Ta mesh added under the lens. Moreover, the β-Ta mesh is removed under the Perminex pillars to create a flat floor for the Perminex.
2. **Cleaning and SiO_2 deposition**: We deposit 200 nm SiO_2 using plasma-enhanced chemical vapor deposition (PECVD) on the backside. This layer is used to protect the backside during the next steps.
3. **NbTiN**: We sputter deposit 200 nm NbTiN. We use photolithography, RIE, and wet etching to form the pattern. The NbTiN will form the ground planes and transmission lines.
4. **Polyimide**: We spin coat 0.5 µm Polyimide on the chip. We use photolithography for patterning. The Polymide will form bridges over the transmission line. The Polyimide is cured at 250°C for 3 hours.
5. **Aluminium evaporation and lift-off**: First, MMA and PMMA are applied to the chip to form the bilayer for the lift-off with PMMA on top. After this, the absorber pattern is made in the resist using electron beam lithography. After this, we deposit a 23 nm thick aluminum layer using evaporation. Then, we use lift-off to remove the PMMA and MAA resist.
6. **SiO_2 back removal**: We wet etch the SiO_2 from the backside of the wafer using a buffered oxide etch (BOE). During this, we protect the front of the wafer with PMMA.
7. **Perminex lens**: We spin ±420 nm Perminex on the backside of the chip. Photolithography is used for patterning.. We protect the front with PMMA and bake at 250°C for 10 minutes. After fabrication, the PMMA is still on the chip as a protection layer

Backshort fabrication (optional):

8. **Backshort marker**: We etch markers with a depth of ±0.1 µm in Si using a potassium-hydroxide (KOH) etch. We use photolithography for the patterning.
9. **Backshort aluminum**: We sputter deposit 100 nm aluminum for the backing reflector. Then we make the pattern using photolithography and wet etching.
10. **Backshort groove**: We etch ±10 µm Si with a KOH etch. We use photolithography for the patterning. This hole is etched under each KID except for 5 KIDs per chip. This groove is discussed in more detail in section 4.4

11. **Backshort Perminex**: This layer connects the backshort chip with the main chip. For this, we spin a $\lambda/4$ thick Perminex layer. $\lambda/4$ equals 2.5 and 4.63 µm for the $10\,\mu m$ and $18.5\,\mu m$ designs, respectively. We use photolithography for the patterning.

Full fabrication:

12. **Dice**: We dice the chips. During this step, we protect the backside of the main chip with a photoresist.
13. **Prepare for mounting**: We inspect and clean chips. After this, the backside resist on the main chip is stripped.

The mask for the main chip of the large $18.5\,\mu m$ absorber design is presented in figure 5.4. Detailed views of the KID and the absorber within this mask are shown in figures 5.2 and 5.3, respectively. The corresponding mask for the backshort chip of the same design is shown in figure 5.5.

After fabrication, a microlens array is mounted to the chip. Before mounting the microlens array, the PMMA protective layer is removed. The microlens array in this work is laser-machined by Veldlaser and designed by Shahab Dabironezare.

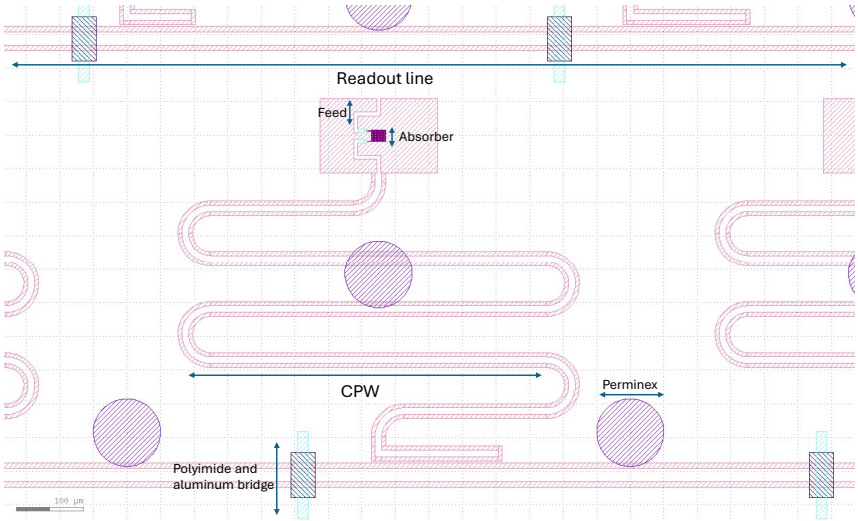

Figure 5.2: A zoomed view of one KID in the chip mask of figure 5.4. The most important parts of the KIDs are highlighted. The etched NbTiN is red. The readout line at the top and bottom can be seen with the polyimide (light blue) and aluminum (dark blue) bridges. From the figure, it looks like the perminex (purple) that connects the lens and chip is on transmission lines, but it is on the back of the chip. The feed and absorber are marked in the middle, and a close-up of both is shown in figure 5.3. The β-Ta layer is hidden for the visibility of the other layers.

5.3. Fabrication results

The main chips have been fabricated successfully. Figure 5.6 shows one of the two fabricated chips with a 5x5 unit cell absorber design for the $18.5\,\mu m$ detector design.

The backshort chip has also been fabricated. However, this has been harder than expected. The first iteration with a KOH etch did not succeed. The KOH etch resulted in a rough surface with sharp edges. As a result, the perminex could not be properly cured[55]. This happened although the grooves were deeper ($50\,\mu m$) then the designed $10\,\mu m$. Therefore, Tonny Coppens developed an alternative route. This resulted in the following altered fabrication steps for the backshort:

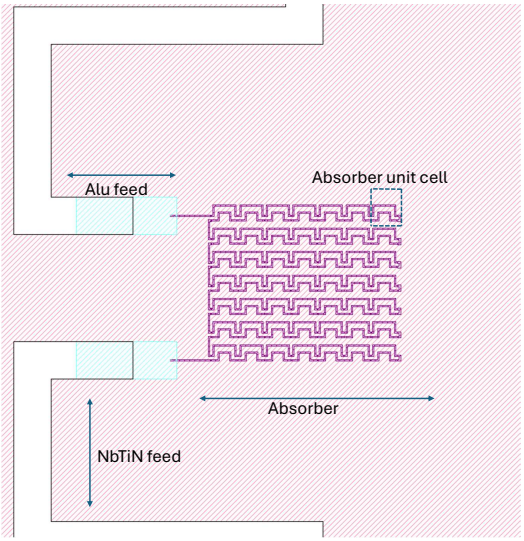

Figure 5.3: A zoomed view of an absorber in figures 5.4 and 5.4 The most important parts are highlighted. The etched NbTiN is red. We see the absorber (purple) with a unit cell highlighted in the middle. The absorber is connected to an aluminum feed (light blue), which is connected to a NbTiN feed.

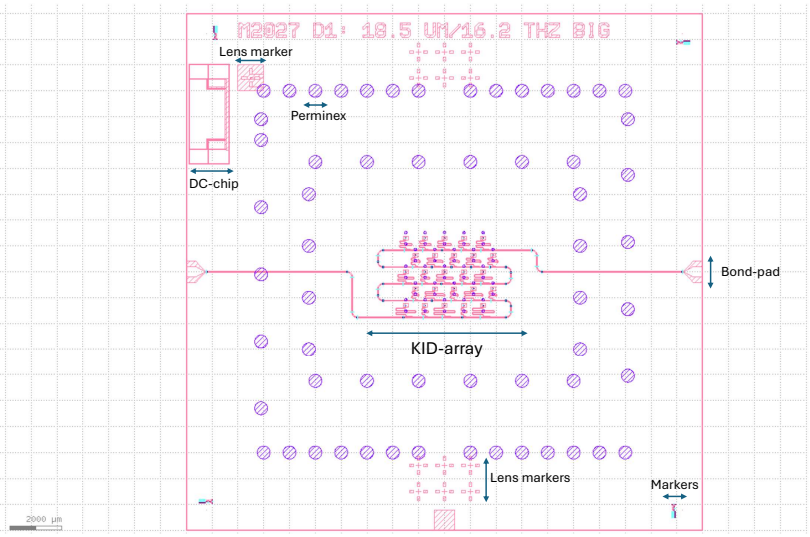

Figure 5.4: The mask design for one of the chips presented in this thesis. The other chips have similar designs. The important parts of the chip design are highlighted. In the upper left of the figure, we see the DC chip used for measuring the resistivity. Next to that we see the lens markers used to align the lens array and the Perminex that connects the lens array to the chip. We see a bond pad on the left and right of the mask to connect wires to the chip. Lastly, we have the KID array in the middle of the mask. The β-Ta layer is hidden for the visibility of the other layers. Zoomed view of a KID and absorber are shown in figures 5.2 and 5.3.

8. **Marker backshort:** We will either etch the markers in the silicon or pattern them in the aluminum.
9. **Backshort aluminum:** Same as before. Only step number is changed.

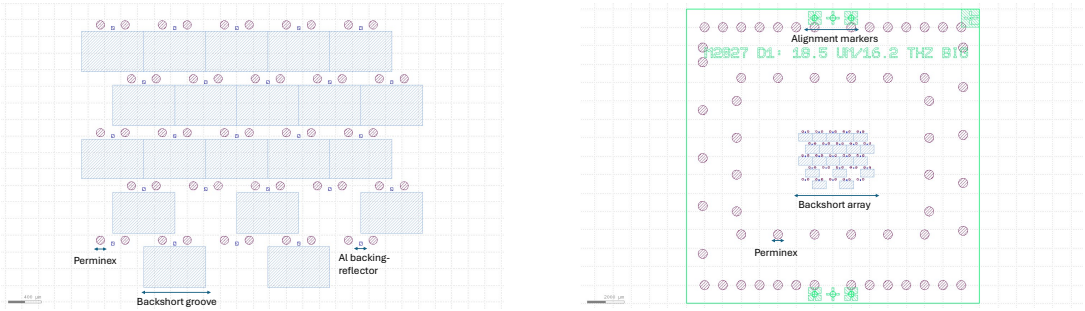

Figure 5.5: Backshort chip mask of the large $18.5\,\mu\mathrm{m}$ absorber variant. For the backshort design, the same alignment markers are used as the lens. The important parts are highlighted: Perminex (grape) connecting the lens and the backshort chip, the etched Silicon (gray), and the aluminum backing reflector (indigo). **Left:** The full chip mask. **Right:** A zoomed-in view of the backshort array.

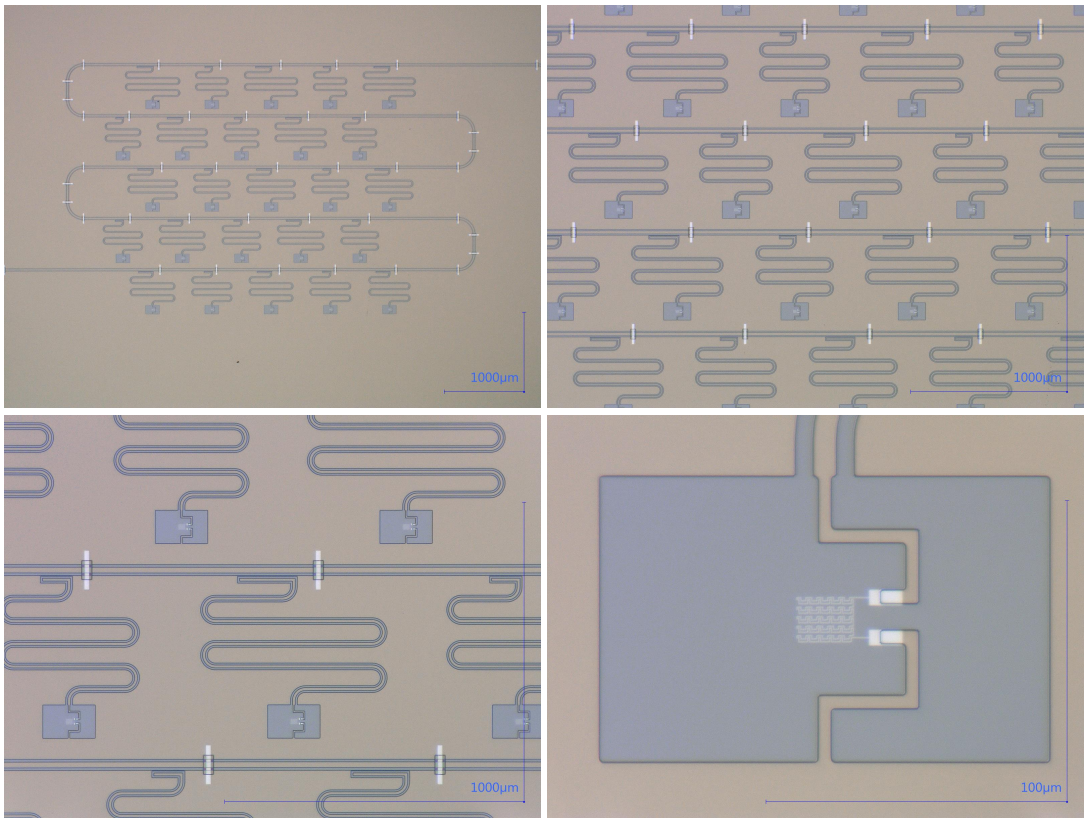

Figure 5.6: Microscope pictures of chip 2 of LT379, which is one of the 5x5 unit cell absorber chips. The taupe background in the picture is the NbTiN ground plane. The blue-grey is the silicon substrate, where all the NbTiN is etched away. The white structures are Al. **Top Left:** Overview of the full KID array with the surrounding ground plane. **Top right:** KID array. **Bottom left:** KID. **Bottom right:** Absorber.

10. **Backshort Perminex**: Same as before. Only step number is changed.
11. **Backshort groove:** We use a thick resist pattern of $10\,\mu\mathrm{m}$ to protect the chip. We use a RIE etch for the silicon.

This route worked for the fabrication of the backshort chips. One of the resulting backshort chips is shown in figure 5.7. However, this chip is still under development. Therefore, the chips will be measured without a backshort in Chapter 7.

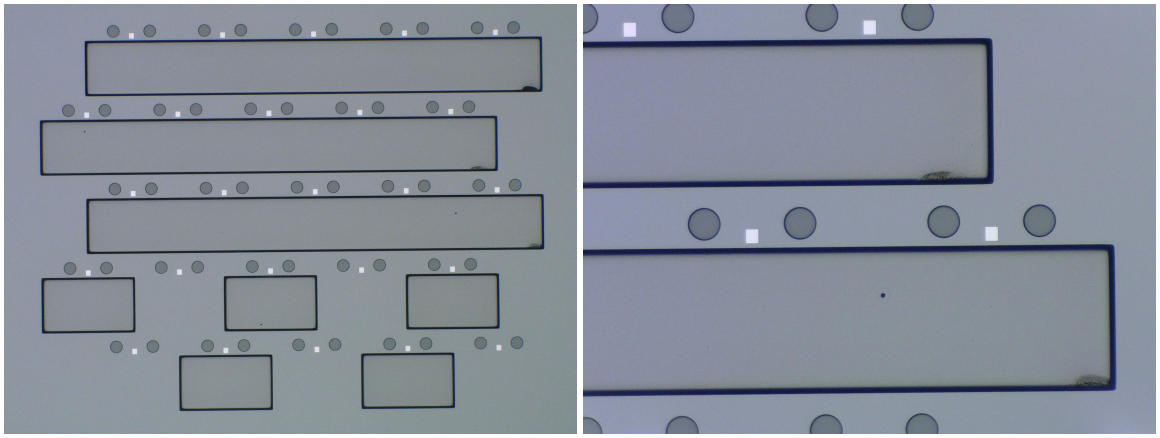

Figure 5.7: The fabricated backshort chips. The blue-grey color is the Silicon backshort substrate. The black rectangles are the RIE etches in the Silicon. The circles are the perminex pillars, and the white squares are the aluminum backing reflectors. **Left:** The full backshort chip. All KIDs in the array contain a RIE etch in the Si under the CPW, except for 5 KIDs. **Right:** A zoomed-in view on the etch. Irregularities in the depth of circa $1\,\mu\mathrm{m}$ can be seen at the edge of the etch in the silicon.

6

Experimental method

For this thesis, different chip designs have been made. The design methods are described in chapters 3 and 4 for the absorber and the rest of the KID, respectively. The final chip designs are discussed in chapter 5. In this chapter, the experimental evaluation of these designs is discussed. The chapter starts with an introduction to the setup used. Then, the readout will be discussed, followed by a model to calculate the expected incident power on the detector.

6.1. Experimental setup

As explained before, MKIDs use superconductors to measure the incoming photons. The detectors need to be cooled to a temperature below the critical temperature of the superconductor. In this thesis, a pulse tube pre-cooled dilution refrigerator cryostat is used. The cryostat setup is shown in figure 6.1.

The cryostat consists of 4 stages: the room temperature stage, '40 K' stage, '3 K' stage, and sample stage. The temperature in the name is not the exact temperature of the stages; it is only a rough value. The actual temperatures can be varied during experiments. Another name for the room temperature stage is the '300 K'. In this thesis, the temperature of the sample stage is 100 mK and is thus also sometimes called the '100 mK' stage. The detector is placed in the sample stage in an additional light-tight box.

Each of the stages of the cryostat is vacuum-pumped and separated by radiation shields. It is possible to mount transparent windows in the shields so the source can also be placed outside the cryostat. A pulse tube refrigerator cools the '300 K', '40 K', and '3 K' stages. A $He_3 - He_4$ dilution refrigerator cools down the sample stage. A Cryophy® shield and a superconducting Niobium shield are placed around the sample stage to protect the sensitive detector from magnetic fields.

In our setup for measurements at $18.5\,\mu\mathrm{m}$, the source used is a blackbody. The blackbody is mounted in the '3 K' stage. The temperature of the blackbody in our setup can be adjusted externally so that measurements for different blackbody temperatures can be done in the same cooldown. The radiation emitted by the blackbody is described in more detail in section 6.3.

For our measurements, we would like to have a narrow band around our desired wavelength of $18.5\,\mu\mathrm{m}$. The blackbody, however, emits more unwanted than desired radiation. The blackbody is not the only source of parasitic radiation. All components have a temperature above zero and will thus emit radiation. Therefore, we need to filter the radiation. A set of optical filters will be used for this. The exact description of the filters with their transmission is discussed in 6.3. All the filters are placed in holders at different stages. One special case is the neutral density filters, which are reflective. These are placed in a holder with a 45° tilt to prevent standing waves by aiming reflected radiation at an absorbing layer. This holder is highlighted as 'ND 100 mK' in figure 6.1

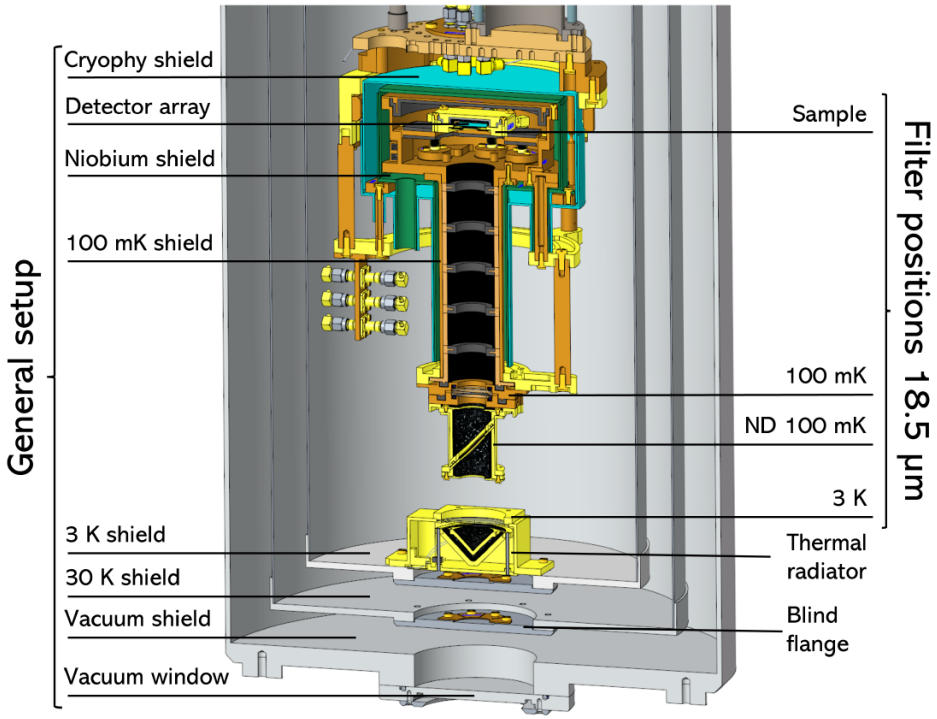

Figure 6.1: The setup used in the measurements. We have a vacuum shield, thermal shields for 30K, 40K, and 100 mK from the outside to the inside, and magnetic Niobium and Cryophy shields. The source is a thermal radiator mounted at the 3K stage shield. We mount filters at the sample stage, 100 mK stage, and at the 3K stage at the holder of the thermal radiator. The Neutral Density (ND) holder is a specific holder that is designed to prevent standing waves within the setup. The reflected radiation is aimed at an absorbing layer. Figure courtesy of Wilbert Ras.

6.2. Microwave readout

Figure 6.2 shows the used homodyne microwave readout. The microwave signal is generated outside of the cryostat. There, the signal is split into two parts: one reference signal that goes directly to the IQ mixer, and one signal that goes to the detector. The signal that goes to the detector will go through all the temperature stages for the detector. The signal will be attenuated in every temperature stage. After modulation by the detector, the signal will leave the cryostat again. On its way, the signal is amplified by a Low Noise Factory cryogenic LNA (type number: LNF-LNC2_6A) at the 3 K stage and by Miteq (type number: A-30-02000600-09-10P) in the 300 K stage. After leaving the cryostat, the modulated signal is mixed with the reference signal in an IQ-mixer. The resulting mixed signal consists of two components: the in-phase I component and the quadrature component Q.

The resulting I and Q components have an offset compared to our KID circle, which is centered at the origin. Therefore, we subtract this offset, resulting in a corrected I' and Q'. These corrected I and Q' can be related to the detector amplitude response A and phase response θ in the following way [4]:

$$A = \frac{X}{\langle X \rangle}. \tag{6.1}$$

Here, X is the magnitude of the mixed signal: $X = \sqrt{I'^2 + Q'^2}$. $< X >$ is the magnitude without a response, so A is normalized to 1. The expression for θ as a function of I and Q is:

$$\theta = \pi - \tan^{-1}\left(\frac{Q'}{I'}\right). \tag{6.2}$$

The data analysis of this signal is discussed in section 7.1.

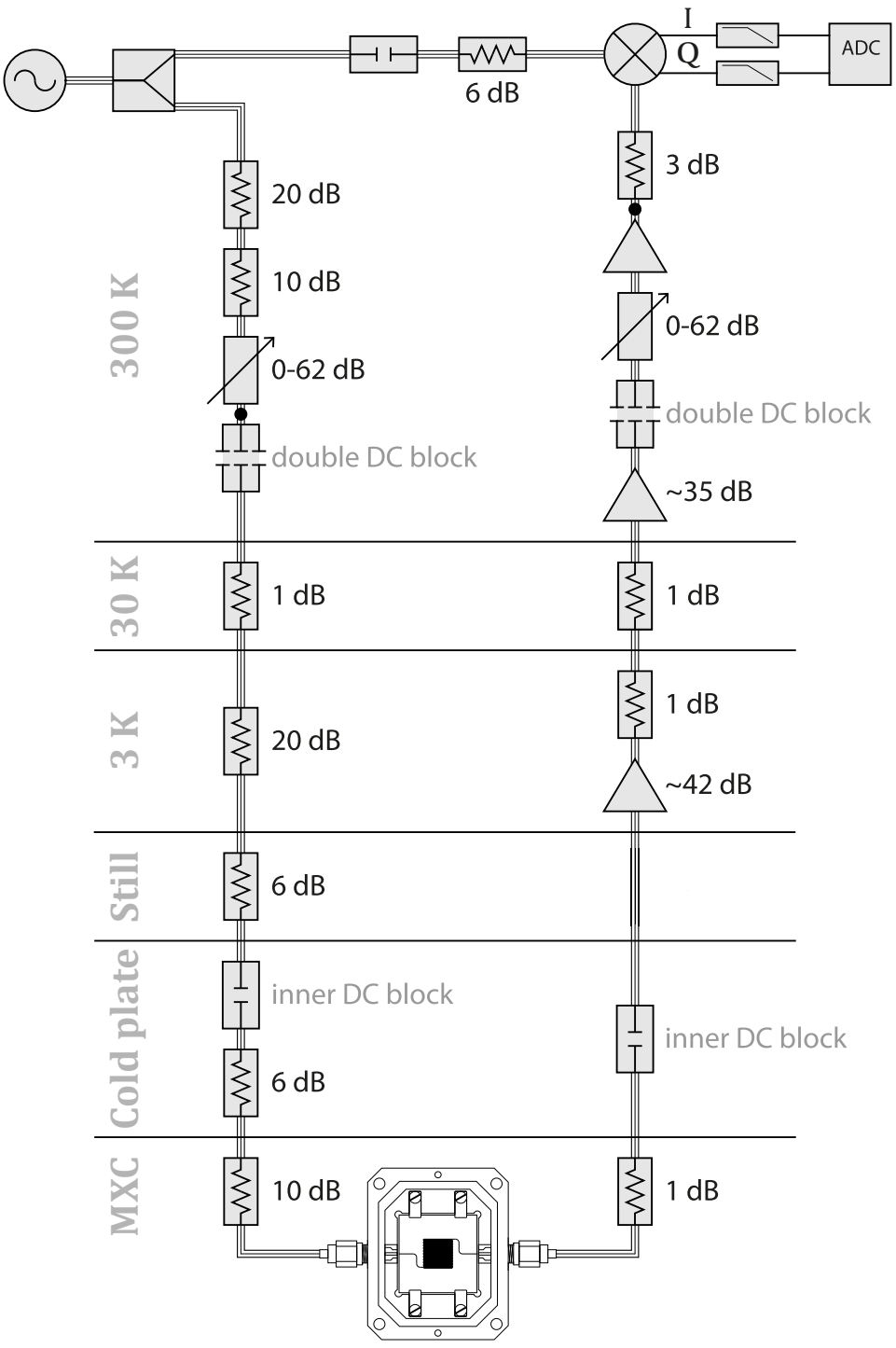

Figure 6.2: The microwave readout. At the room temperature stage, copper coaxial cables with a diameter of 3.8 mm are used. We use steel cables with a diameter of 2.19 mm at the 30 K stage. From the 20 dB attenuator at the input side down to the 1 dB attenuator at the mixing chamber (MXC), CuNi cables with a diameter of 0.86 mm are used. Between the two 1 dB attenuators, aluminum cables (2.30 mm diameter) are placed, while NbTi cables (0.86 mm diameter) are used just before the first amplifier. The readout power is controlled using adjustable attenuators (Weinschel 8310). The amplifiers at the 3 K stage and 300K stage are a Low Noise Factory LNF-LNC2_6A and an MITEQ LNA-30-02000600-09-10P, respectively. For S21 measurements, the components above the black dots in the setup can be replaced with a VNA (Keysight N5230A PNA-L). This figure is adapted from [18].

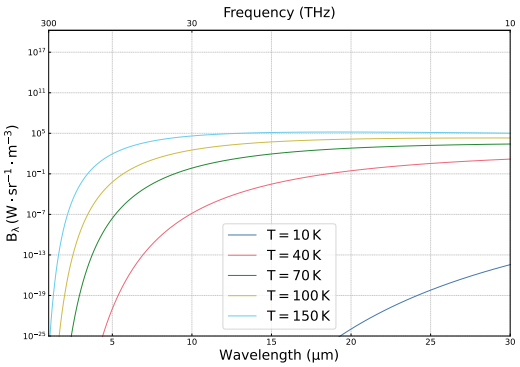

Figure 6.3: The irradiance as a function of wavelength for different blackbody temperatures. We see that most power is concentrated in the lower wavelengths.

The IQ mixer and signal generator can also be replaced by a vector network analyzer (VNA) to perform S_{21} measurements. In that case, the components above the black dots in figure 6.2 will be replaced by a VNA.

6.3. Modeling of the expected power

In this section, we will derive the expected power arriving at the detector. The radiation is generated by a blackbody. Planck's law describes the radiation emitted by the blackbody for 1 polarization:

$$B_\lambda(\lambda, T) = \frac{hc^2}{\lambda^5} \cdot \frac{1}{e^{\frac{hc}{\lambda k_B T}} - 1} \tag{6.3}$$

Here, k_b is the Boltzmann constant, h is Planck's constant, and c is the speed of light in vacuum. Figure 6.3 shows the blackbody irradiance for different blackbody temperatures. The blackbody emits a lot of unwanted radiation, especially at lower wavelengths. Therefore, the radiation will pass through a set of filters. The filters are shown in figure 6.4.

To calculate the expected power arriving at the detector, we need to multiply the radiation from the blackbody with the filter transmission and integrate this to find the total power arriving at the detector:

$$P_{rad}\,(T) = \int_0^{hc/2\Delta} \eta_{\text{opt}}(\lambda)\Theta(\lambda)B_\lambda(\lambda, T)\lambda^2\, d\lambda \tag{6.4}$$

Here $\Theta(\lambda)$ is the transmission spectrum of all the filters, and η_{opt} is the setup-specific optical coupling. η_{opt} is described in more detail in section 6.4. We integrate the power up to the wavelength that corresponds to the bandgap. This corresponds to a wavelength of ≈ 3.4mm.

The filter transmission of all the filters is shown in figure 6.4. For the measurements, the following filters are used in the measurements:

- *Panels a and b: ND1 and ND3 Filter.* Both are Neutral Density Filters produced by Thorlabs, inc. (part number: NDIR(10/30)B). The name gives the optical density of the filters: $OD = \log_{10}\left(\frac{1}{T}\right)$ with T the average transmission. We will use filters in our measurements with a 10^{-1} transmission for the ND1 and 10^{-3} for the ND3. Panels a and b show that the transmission of both filters is lower for higher wavelengths. They are primarily used to reduce the amount of radiation with longer wavelengths. The filter consists of a ZnSe substrate with a thin Nickel film on top. The filter is characterized between 0.2-18 μm. The transmissions at the edge of the characterization band are used for wavelengths outside of this band.
- *Panel c: BP185.* A $18.5\,\mu\text{m}$ bandpass filter made by Northumbria Optical Coatings ltd (part number: NC-2444-1). Panel c shows that the filter has a very high transmission for a very narrow

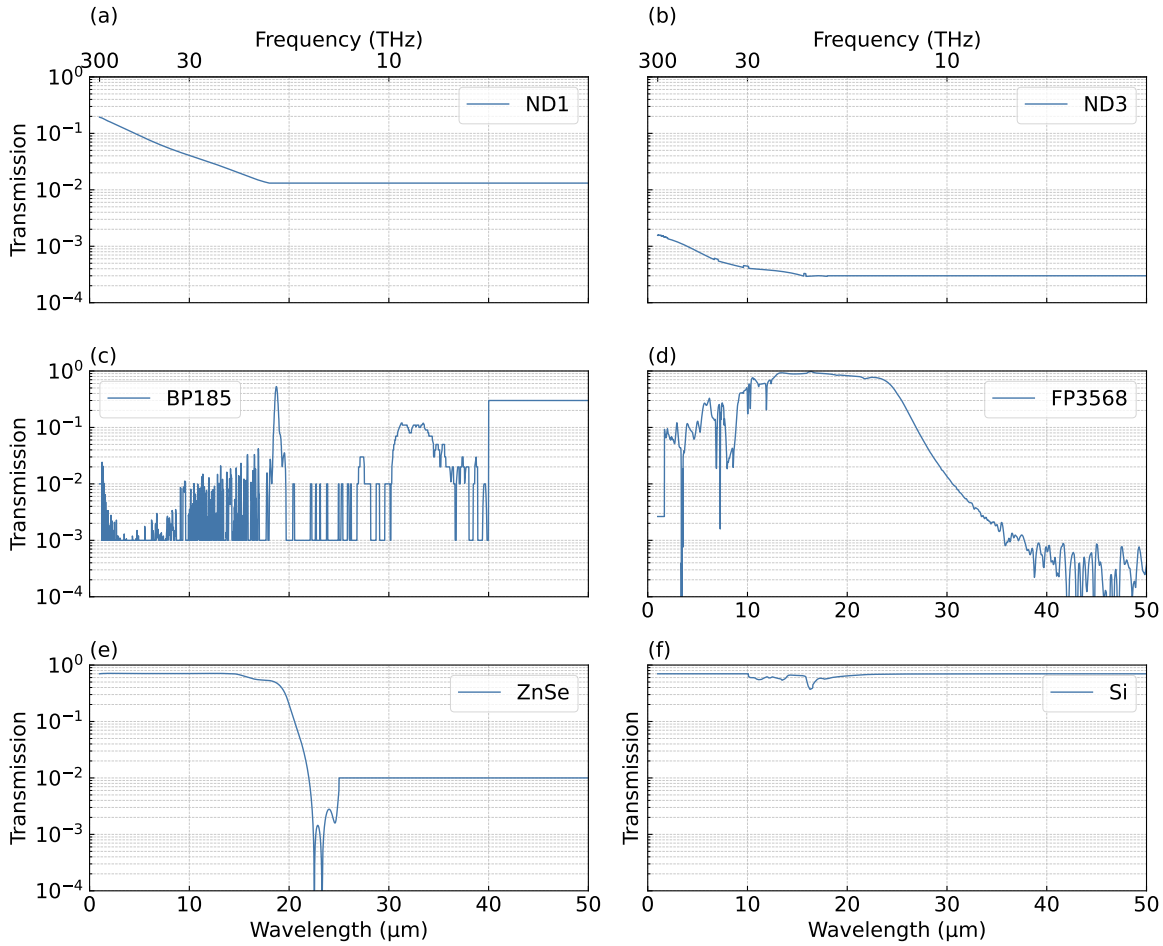

Figure 6.4: A slice of the total filter transmission of all the filters used for the measurements in this work. The full filter transmission is characterized between 1 mm and $1\,\mu\mathrm{m}$. **Panel a:** The optical density of a 1 neutral density filter. **Panel b:** The optical density 3 neutral density filter. **Panel c:** The $18.5\,\mu\mathrm{m}$ bandpass filter. **Panel d:** The FP3568 short wave pass filter. **Panel e:** The Zinc Selenide window. **Panel f:** The silicon lens and substrate.

band given by$\lambda_{\text{center}}/\text{FWHM} = 50$. The filter is characterized between 0.8 and 40 μm. For $\lambda < 0.8\,\mu\mathrm{m}$, we use the transmission at $0.8\,\mu\mathrm{m}$. For $\lambda > 40\,\mu\mathrm{m}$, we assume the transmission to be 0.3 [56].

- *Panel d: FP3568*. It is a metal mesh filter made by QMC Instruments Ltd. Panel d shows that the transmission decreases for longer wavelengths, and this filter is thus a short-wave pass filter. The cut-off wavelength is approximately $23\,\mu\mathrm{m}$. It has been characterized between 17- $80\,\mu\mathrm{m}$. The transmissions at the edge of the characterization band are used for other wavelengths outside of this band.
- *Panel e: ZnSe.* A Zinc Selenide window produced by Thorlabs, inc.(part number: WG70530). Panel e shows that it has a lower transmission for longer wavelengths, and the filter is thus a short-wave pass filter. The cut-off wavelength is $22\,\mu\mathrm{m}$. The thickness of the window is 3.0 mm. It is characterized for 1-25μm. We assume a transmission of 0.01 outside this band [57].
- *Panel f: Si.* The Silicon lens and substrate. The lens and substrate absorb and reflect radiation. The absorption of silicon is described in more detail in Appendix F.

The filter transmission is characterized at room temperature except for the $18.5\,\mu\mathrm{m}$ bandpass filter and silicon. The bandpass filter has an in-band characterization at 77K and an out-of-band characterization at room temperature. Silicon is characterized at 10 K. The filters' diameter is the same: 25.4 mm. During the measurements, the filters are used in this configuration:

Filters in the holder at the sample stage:

1. $18.5\,\mu\mathrm{m}$ bandpass filter,
2. $18.5\,\mu\mathrm{m}$ bandpass filter,
3. $18.5\,\mu\mathrm{m}$ bandpass filter.

Filters in the holder at the $100\,\mathrm{mK}$ *stage:*

4. $18.5\,\mu\mathrm{m}$ bandpass filter,
5. Zinc Selenide window,
6. FP3568 filter.

ND holder at the $100\,\mathrm{mK}$ *stage:*

7. ND3 or ND1 filter, depending on the measurement.

Filter holder at the blackbody in the $3\,\mathrm{K}$ *stage:*

8. $18.5\,\mu\mathrm{m}$ bandpass filter,
9. Zinc Selenide window.

6.4. Optical coupling

The optical coupling for a multi-moded detector can be defined as:

$$\eta_{\mathsf{opt}} = \eta_{\mathsf{so}} \frac{\eta_{\mathsf{ap}}}{\eta_f}. \tag{6.5}$$

Here η_{ap} and η_f are the aperture and focus efficiency, respectively, as described in section 3.3. η_{so} is the spill over efficiency:

$$\eta_{so}^{\Omega_s}(f) = \frac{\iint_{\Omega_s} F\left(f, \theta_l^{pw}, \phi_l^{pw}\right)\, d\Omega}{\iint_{4\pi} F\left(f, \theta_l^{pw}, \phi_l^{pw}\right)\, d\Omega}. \tag{6.6}$$

Here, Ω_s is the solid angle of the radiation as seen by the detector. In our case, the limiting aperture is a filter in the 3K filter holder in figure 6.1. This filter has a diameter of 25.4 mm and is placed at a distance of 300 mm from the detector. The corresponding opening angle from this filter is approximately 1.5°.

We need to find the absorbed power P_{abs} to find the reception power pattern F to calculate the efficiencies required for the optical coupling. Figure 6.5 shows the GOFO (Geometrical Optics, Fourier Optics) that is used to calculate the absorbed power. The technique primarily uses FO as this method allows us to calculate the plane wave spectrum (PWS), which is needed as input for the Floquet model, relatively easily [15]. The incident field is propagated using FO to the surface of the lens. From the lens's surface, GO propagates the radiation to an auxiliary surface called the FO-sphere. GO is used for this part of the propagation as it approximates the radiation as rays, which allows us to use Snell's law to simplify the situation [58]. Then, FO is used from the FO-sphere to the focal point, i.e., the absorber. The FO gives us the PWS, i.e., the values of V_+^{TE} and V_+^{TM}, as shown in figure 2.11. We find the $\bar{Z}_a$ by simulating the absorber in CST. Then, using the Floquet model, the absorbed power can be found. The simulation for this absorber was done with a code of Daan Roos [59].

Then, using P_{abs} we can calculate the efficiency terms. We find η_{ap} by dividing the max value of the $P_{\mathsf{abs}}(f, \theta, \phi)$ by the incoming power, as described in equation 3.6. We also calculate the reception power pattern F by normalizing P_{abs} by its maximum value, as described in equation 3.11. Then using $F\,\eta_f$ and η_{so} are calculated via equations,3.8 and 6.6, respectively. All the steps are done for both polarizations separately. The total optical coupling η_{opt} is calculated for both polarizations via 6.5. Figure 6.6 shows the total calculated optical coupling, which is higher than 1, as the optical coupling is normalized to the maximum power a single moded device can absorb. Absorbers are multi-moded devices and can thus have an optical coupling larger than 1. We find that the number of effective modes the absorber can couple to, $\frac{\eta_{ap}}{\eta_f}$, is 0.99 for the TE polarization and 1.07 for the TM polarization. We find a spillover

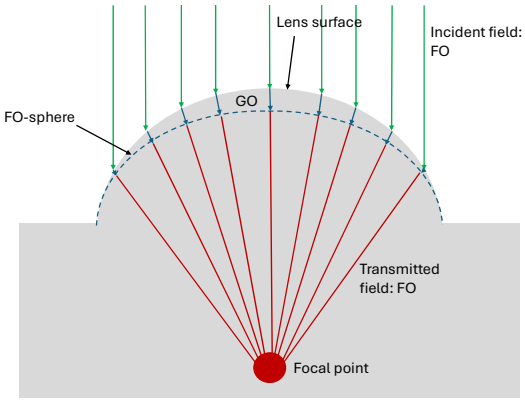

Figure 6.5: A not-to-scale schematic view of the GOFO technique [15] The incoming field is propagated via FO to the lens surface. From there, GO is used to the FO-sphere, as it allows using Snell's law [58]. From the FO sphere, the field is propagated to the focal point. The final result is a PWS that can be used with the Floquet model.

efficiency of 1 for both polarizations. This means that the lens focuses all the radiation on the absorber. Combining this, we find that $\eta_{opt} = 0.99$ for the TE polarization and $\eta_{opt} = 1.07$ for the TM polarization. These efficiencies are calculated without considering absorption in the silicon lens and substrate. If we consider 15% absorption of the power in the lens and substrate as described in Appendix F, we find that $\eta_{opt} \approx 0.92$ for the TE polarization and $\eta_{opt} = 0.85$ for the TM polarization.

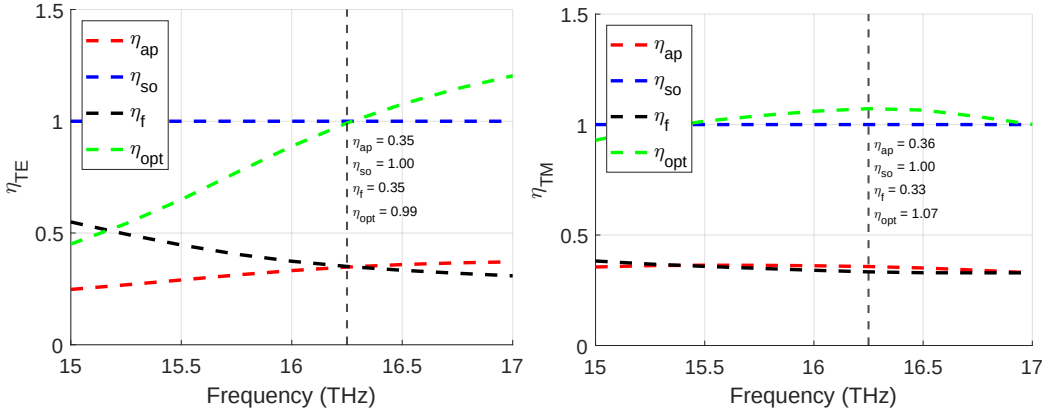

Figure 6.6: The optical coupling efficiencies of the 5x5 unit cell $18.5\,\mu\text{m}$ absorber for both polarizations. η_{ap}, η_f, η_{so} and η_{opt} are calculated via equations 3.6, 3.8, 6.6, and 6.5, respectively. The absorbed power P_{abs}, which is needed as input in these equations, is found using the GOFO model described in this section. This simulation is done with the measured value of ρ= $3.1\,\mu\Omega\,\text{cm}$. We find a spillover efficiency of 1 for both polarizations. This means that the lens focuses all the radiation on the absorber. The simulation does not consider absorption in the silicon lens or substrate. **Left:** The optical efficiencies of the TE polarization. The absorber effectively couples to 0.99 modes, resulting in $\eta_{opt} = 0.99$ for a spillover efficiency of 1. **Right:** The optical efficiencies of the TM polarization. The absorber effectively couples to 1.07 modes, resulting in $\eta_{opt} = 1.07$ for a spillover efficiency of 1.

7

Experimental results

This chapter will discuss the experimental results. The experimental setup used for these measurements is described in chapter 6. Three chips will be measured: chip 2, a $18.5\,\mu\mathrm{m}$ KID design with a smaller absorber as described in chapter 5, chip 5, an identical copy of chip 2, and a 12 THz membrane lens-absorber coupled KID designed by Jochem Baselmans and Shahab Dabironezare. This chapter starts with the data analysis and ends with the results of the measurements.

7.1. Data analysis

7.1.1. Single-photon counting

The first part of the experiment is a single-photon counting experiment. These measurements were done for relatively low blackbody temperatures ($\approx 3 - 100K$). The number of photons coming is still low enough for pulses to not overlap for these temperatures, so we can still distinguish peaks. We use a sampling rate of 1 MHz for these measurements to have enough sample points in pulses, which are typically a few hundred microseconds long. First, the data analysis used for single-photon counting is discussed, followed by the results of the measurements.

The data analysis consists of a few steps: smoothing the response, selecting peaks, measuring noise spectra, and finally, filtering the pulses with an optimal filter to find the peak height. Here, the steps will all be described in chronological order.

Finding pulses with response smoothing

The first step of the data analysis is smoothing. The goal of smoothing is to make it easier to find the location of the peaks in the time domain. For this, the data stream is convoluted with the expected pulse shape, which is an exponential decay with the recombination time τ_r as time constant: $e^{-\frac{t}{\tau_r}}$. We find the value of τ_r using a fit. This is shown in figure 7.1. From this smoothed response, the location of peaks can be found. We select the pulses in the raw timestream based on these locations.

Selecting pulses

Now that we have found the locations of the pulses, we can select the peaks corresponding to photons. The first requirement to select a peak is that it must be between a minimum and maximum threshold. A minimum threshold is set to reject peaks originating from noise spikes. This is also referred to as the minimum peak height (MPH). A maximum can also be chosen to eliminate cosmic rays. The thresholds are manually chosen as each measurement and/or KID gives different noise and peak heights values.

The second requirement is that the peak must stand out compared to its surroundings. For this, we set the minimum peak prominence (MPP). The minimum peak prominence is the vertical distance that the peaks must descend on either side of the peak before reaching an endpoint or increasing to a value higher than the original peak [4]. In this work, we use the same MPH and MPP for all measurements.

The thresholds are found by iterating. The thresholds are deemed good when the pulse shapes of the selected pulses match the expected exponential decaying pulse shape in aluminum, while pulses with

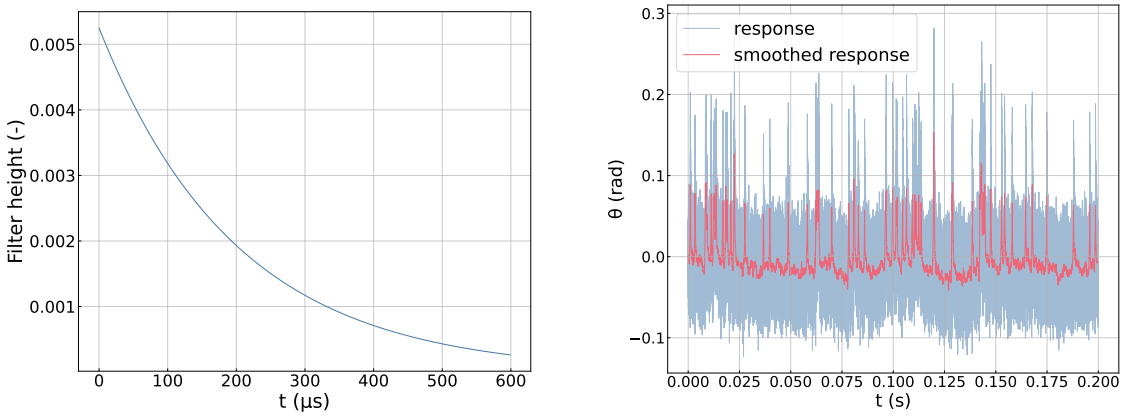

Figure 7.1: We smooth the response with an exponential decay to find the locations of peaks. **Left:** An example of an exponential filter, $e^{-\frac{t}{\tau_r}}$ that is convolved with the response to smoothen the data. The time constant is the quasiparticle recombination time: τ_r **Right:** The original and smoothed responses. The peaks are more prominent, and the location of the peak can be found more easily with a smoothed response.

significantly larger pulse heights (cosmic rays) are rejected.

We also remove overlapping pulses. For this, we set a pulse window based on the recombination time. It is set such that the pulses are decayed within the pulse window. If there is another peak found within the pulse window, then these pulses are deemed as too close. These pulses are then removed as they will incorrectly alter the peak height and the averaged pulse shape. However, we still consider them for the coupling estimations, as it is still an incoming photon.

The pulse window is set manually based on the averaged pulse shape. The averaged pulse shape is the shape that we get if we average all the pulse shapes. The averaged pulse shape should not be confused with the average pulse shape, which is the pulse shape of a typical pulse from the middle of the histogram.

Peak height estimation using optimal filter

To estimate the height of the peaks, we will use an optimal filter. For the filter to work properly, the pulses will be aligned so that their rise is in the same location. The optimal filter is based on this model for a signal: $d(t) = Hm(t) + n(t)$. Here $d(t)$ is the data , $m(t)$ is the normalized pulse response and $n(t)$ is the noise, all in the time domain. H is the peak height and is the variable that we want to know to find the energy of the incoming photon. For this, we will be applying a Fourier transform to $d(t)$ to find the frequency spectra of the signal: $D(f) = HM(f) + N(f)$. For this signal, an expression exists that minimizes the error of the solution for H [18]. This expression is the optimal filter [60]:

$$H = \frac{\int_{-\infty}^{\infty} \frac{D(f)M^*(f)}{|N(f)|^2}\, df}{\int_{-\infty}^{\infty} \left|\frac{M(f)}{N(f)}\right|^2 df} \tag{7.1}$$

Here, the frequency components $D(f)$, $N(f)$, and $M(f)$ are calculated using the single-sided, fast Fourier transform. We use the pulse data and the averaged pulse to calculate $D(f)$ $M(f)$, respectively. We calculate the PSD $|N(f)|^2$ using Welch's method. In this method, the data is first divided into overlapping segments. Followed by a periodogram calculated for each of the segments. Finally, the periodogram of the individual segments is averaged to find an estimation of the PSD with a low variance [61]

The noise spectrum needs to be calculated from a 'dark' measurement. In our case, the 'dark' measurement is the data between pulses.

7.1.2. Resolving power calculation

We will make a histogram using the height of the peaks, H, found using the optimal filter. We use a Gaussian kernel density estimate (KDE) on the peak heights H to find the average and variance of the histogram. The KDE uses a summation of Gaussians at each data point to estimate the continuous distribution of peak height. This gives us a continuous estimate of the distribution, which often captures the shape more accurately and converges faster than a histogram with discrete bins [62]. We can then extract a FWHM δ and average from the KDE. For small response $\theta < 1.5$ rad, like the ones in this thesis, the relation between E and H is assumed to be linear [4]:

$$\delta E = \frac{|E|}{|H|}\delta H. \tag{7.2}$$

Using this linear relation and equation 4.8, the resolving power can be calculated with the average value for H and the FWHM δH.

We can now calculate the different components of R, such as R_{sn}. For this, we need to find $deltaH_n$. δH_n determines the upper limit of the resolving power that we can reach if we are only limited by noise in the setup. It is defined as the FWHM of the histogram that would result if we use the noise $N(f)$ as an input in the optimal filter, i.e., we substitute $D(f) = N(f)$ in equation 7.1. This yields: [4, 60, 63, 64]:

$$\delta H_n = 2\sqrt{2\ln(2)}\left[\int_{-\infty}^{\infty} \frac{|M(f)|^2}{|N(f)|^2}\, df\right]^{-1/2}. \tag{7.3}$$

The factor $2\sqrt{2\ln 2}$ comes from a change from σ to FWHM.

7.1.3. Power-integrating

The second type of measurement is a power-integrating measurement. In this type of measurement, the blackbody is set to such a high temperature that we are even beyond the situation where photon peaks overlap. In that case, we measure an overall response offset compared to the situation without incoming power. We measure this response as a function of incoming power.

The blackbody will be set to a set of center temperatures for these measurements. A small sweep is performed around each center temperature, resulting in a small change in incident power. This allows us to measure the responsivity $\frac{d\theta}{dP}$ for each of the temperatures and derive important parameters such as the optical coupling and the sensitivity of the detector expressed as a Noise Equivalent Power (NEP). The NEP is the power that results in an SNR of 1 in an integration time of 0.5 s. The relevant steps and equations to find these results are discussed in the next section.

In the power-integrating measurements, we use two different sample rates of 1 MHz and 50 KHz.

7.1.4. Data analysis

The first step of the data analysis is finding the responsivity $\frac{d\theta}{P_{s,f}}$. Here, $P_{s,f}$ is the blackbody power per frequency, which can couple to a single-mode detector:

$$P_{s,f} = \lambda_0^2 B_f(f,T)\Theta(f). \tag{7.4}$$

Here, λ^2 is the single mode throughput, $B_f(f,T)$ is the spectral radiance per frequency for 1 polarization, and $\Theta(f)$ is the filter transmission.

We can find $\frac{d\theta}{P_{s,f}}$ by fitting a linear curve to the data of the small sweep of loading power. The result for a sweep around one of the temperatures, 100K, is shown in figure 7.2.

The second step involves finding the recombination time τ_R. We can find it from the roll off in photon noise in either the amplitude, phase, or their cross PSD. This work will use the cross PSD to eliminate the noise from uncorrelated sources such as TLS and the amplifier. The Cross PSD in the case of photon noise is given by [16]:

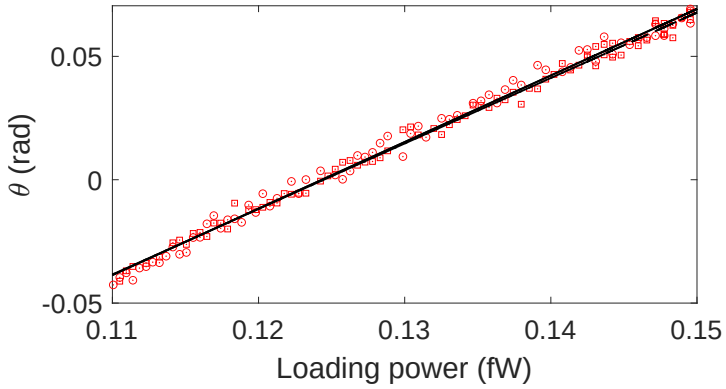

Figure 7.2: The response, in this case θ, of a KID for a sweep of power. The power here is the loading power arriving at the detector. The blackbody temperature is swept around 100 K. We linearly fit the data points to find the responsivity of the detector: $\frac{d\theta}{P_{s,f}}$.

$$S_{A,\theta}(F) = \frac{2P_{\text{abs}}hf(1+\eta_{opt}O_f)}{1+(2\pi F\tau_R^*)^2}.\frac{dA\,d\theta/dN_{qp}^2}{1+(2\pi F t_{\text{ring}})^2}, \tag{7.5}$$

Here, F is the modulation frequency, f is the frequency of the incoming photons, and t_{ring} is the resonator ring time. O_f is the occupation number per mode[65]: $\left(e^{hf/(k_bT}-1\right)^{-1}$.

For a KID, we typically find for t_{ring} of microseconds, while τ_r is typically in the order of 0.1 ms. This means that $\tau_r >> t_{\text{ring}}$ and thus that the roll-off of the PSD is caused by the recombination time and not the resonator ring time.

The cross PSD can be calculated via the time domain data, as the cross PSD, $S_{A,\theta}$, is the Fourier transform of the cross-correlation function $R_{A,\theta} =< A(t)\theta(t-u) >$ [16]. In the data analysis, this calculation is done using the MATLAB function *cspd*. The recombination time can be found by fitting the *cspd* output with 7.5. This is shown in figure 7.3.

We can use the fitted values of the responsivity $\frac{d\theta}{dP_{s,f}}$ and recombination time τ_R to find the experimentally determined NEP [12]:

$$\text{NEP}_{\text{exp}}(P,F) = \sqrt{S_\theta(F)}\left(\frac{d\theta}{dP_{s,f}}\right)^{-1}\sqrt{1+(2\pi f\tau_R)^2}, \tag{7.6}$$

where $S_\theta(F)$ is the PSD of the phase response θ.

We can also define the theoretical NEP in a background-limited case where photon noise dominates [66, 67]:

$$\begin{aligned}\text{NEP}_{\text{tot}}^2 &= \text{NEP}_{\text{Poisson}}^2 + \text{NEP}_{\text{Wave}}^2 + \text{NEP}_{\text{R}}^2 \\ &= \int 2\eta_{\text{opt}}(f)P_{sf}(f)hf\,df + \int \eta_{\text{opt}}^2(f)P_{sf}(f)hf\Theta(f)O_f(f)\,df \\ &+ \int \frac{4\eta_{\text{opt}}(f)\Delta P_{sf}(f)}{\eta_{pb}}\,df.\end{aligned} \tag{7.7}$$

Here, the first term on the right-hand side,NEP_{poisson}^2, is Poisson noise from photon fluctuations. The second term, NEP_{Wave}, is the NEP from photonbunching. The last term, NEP_{R}, is the NEP originating from generation recombination noise.

In the case that the NEP is limited by photon noise, we can relate the experimental NEP to the theoretical NEP in the following way: $\text{NEP}_{\text{tot}}^2 = \eta_{opt}^2(f_0)\text{NEP}_{\text{exp}}^2$. Here, we assume that $\eta_{opt}(f)$ is approximately

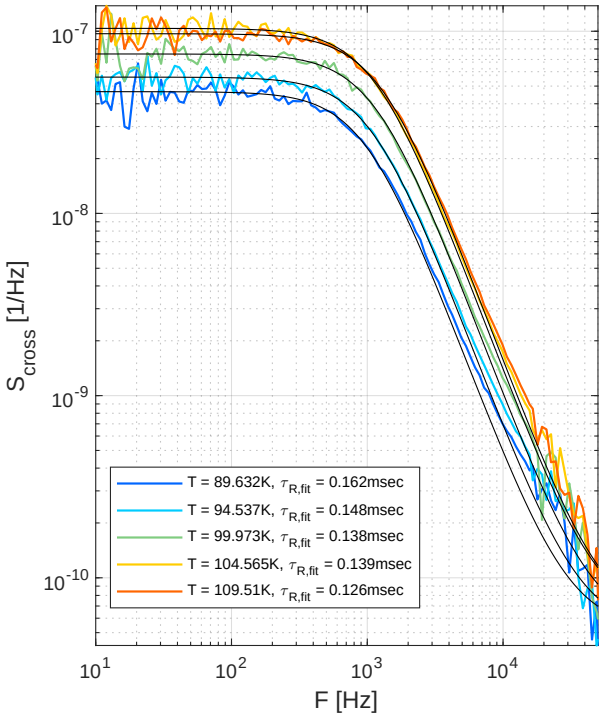

Figure 7.3: The cross PSD, S_{cross}, for multiple blackbody temperatures. The data is calculated using time domain data and is fitted by equation 7.5. The resulting fitted recombination time is shown in the legend.

constant over a narrow frequency band with center frequency f_0. We can then rearrange this to an expression for the optical coupling [66]:

$$\eta_{\text{opt}} = \frac{\int 2P_{s,f}hf\,df + \int 4\Delta P_{s,f}/\eta_{\text{pb}}\,df}{NEP^2_{\text{exp}} - \int 2P_{s,f}hf\Theta(f)O_f\,df}. \tag{7.8}$$

This is the coupling compared to a single-mode detector sensitive to 1 polarization. This means that this coupling can be larger than 1, as the absorbers in this work can couple to both polarizations and multiple modes.

7.2. Results

7.2.1. $18.5\,\mu\text{m}$ lens-absorber coupled KID on substrate

First, we performed S_{21} measurement on chip 5 from LT379. The measured and designed resonance frequencies and quality factors are added in Appendix D. The resonance frequencies of the KIDs were found to be approximately 300-400 MHz lower than designed. A possible reason for this could be that the KIDs do not have a backshort, and the backshort is expected to increase the resonance frequency.

We also found that the internal quality factor Q_i is lower than expected. It is in the order 10^3 instead of $10^5 - 10^6$. For this purpose, we performed a S_{21} measurement on chip 2, the duplicate of chip 5 without a lens array. This chip had quality factors within the expected $10^5 - 10^6$. We inspected chip 5 using an optical microscope and saw no visible damage in the readout line and the KIDs. We expect that the lens array mounting or an invisible fabrication fault is the cause of the low Q_i's for chip 2. We continued measurements with chip 2, as a piece of chip 5 was broken off, making it impossible to mount a lens array on this chip.

Single-photon counting

The first measurement that we performed was a single-photon counting experiment. In these measurements, we use the ND3 filter. The resulting time domain data for one of the measured KIDs, KID5, is shown in the left panel of figure 7.4. This KID is measured at a readout power of -102 dBm for 1 s.

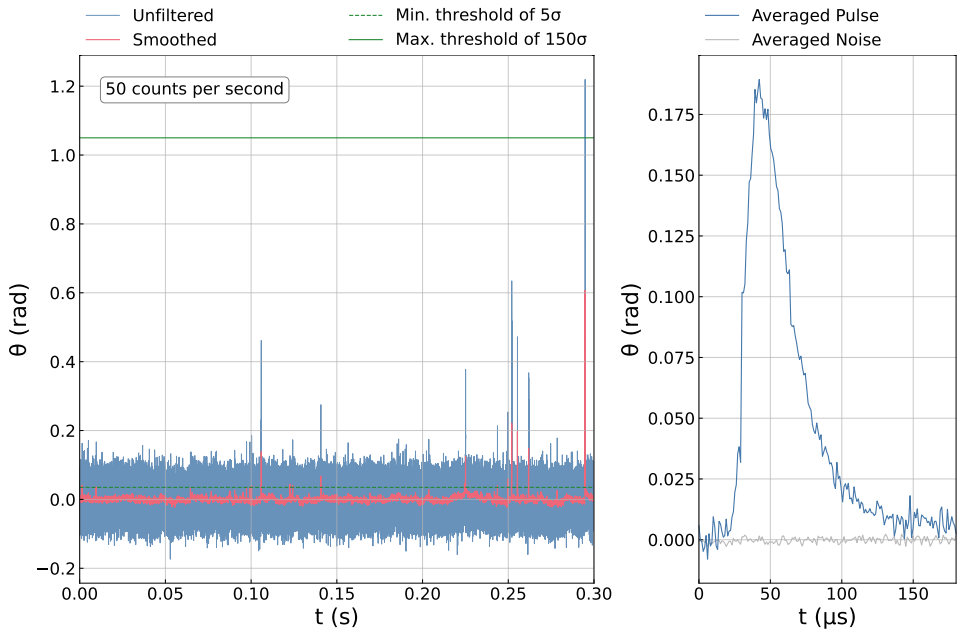

Figure 7.4: The resulting time domain data of KID 5 of chip 5 of LT379. This KID is measured for 1 s with a readout power of -102 dBm. We see photon pulses with a large spread in height in this data. **Left:** A slice of the time domain data. We smoothed the response with an exponential with $\tau_r = 80\,\mu s$. A minimum and maximum threshold for the peaks of 5σ and 150σ are used, respectively. We find photon pulses with a large spread of energy in the data. **Right:** This data set's averaged pulse and noise. The averaged pulse is the average of all pulses and not a typical pulse with average peak height in the distribution. We find the typical pulse shape of an aluminum KID. The decay is rather quick with a low τ_r.

A smoothing filter with $\tau_r = 80\,\mu s$ is used. The minimum and maximum threshold are set at 5σ and 100σ, respectively. In this time domain data, we can measure pulses, but the pulses have a very large spread in height. That we actually measure pulses can also be seen in the right panel of figure 7.4, which shows the average pulse and noise. In this figure, we can recognize the typical pulse shape in Al with a relatively sharp rise and an exponential decay. The pulse decays quickly, meaning the measured τ_r is relatively low for these KIDs.

The spread in the pulse heights can also be observed in the resulting histogram, as shown in figure 7.5. The spread in the peaks is large, resulting in a very low $R = 0.8$.

We expect that phonon losses in the substrate cause this spread. This is confirmed by the calculation of R_{phonon}, as given in equation 4.12, with a value of $J = 3.1$ for aluminum on a silicon substrate [40]. We find $R_{\text{phonon}} = 1.67$, which indeed is low enough to limit the resolving power. To test that phonon losses are indeed the cause of the low resolving power, we measure another chip with KIDs on a membrane as described in 7.2.2. We use a chip with KIDs on a membrane as they have less phonon losses a thus a lower J. Using $J = 0.38$ from [40] for Al on a 110 nm SiN membrane, we find $R_{\text{phonon}} = 3.98$. Therefore, we would expect the KIDs on membranes to have a higher resolving power.

Figure 7.5 shows that the histograms of the noise heights and the pulse heights almost overlap. As a result, it is hard to distinguish noise and pulses. It is also hard to spot cosmic rays, as there are no real outliers with high peak heights. The low value for R makes it thus hard to distinguish the pulses originating from the source from noise and cosmic radiation. This also makes it impossible to extract a valid optical coupling. Therefore, we also perform power-integrating measurements for this KID in 7.2.1.

We also found something strange during the measurements: after some time, the photons disappeared. This effect is shown in figure 7.6. The measurement parameters are equal to the measurement before in figure 7.4. However, all the photons are gone. We expect a superleak to be the cause of this. The cryostat has a known problem with Helium-3 leakage. We think that the Helium-3 is absorbing the radiation. However, we could not find literature on the exact absorption of Helium-3, so this is only a hypothesis.

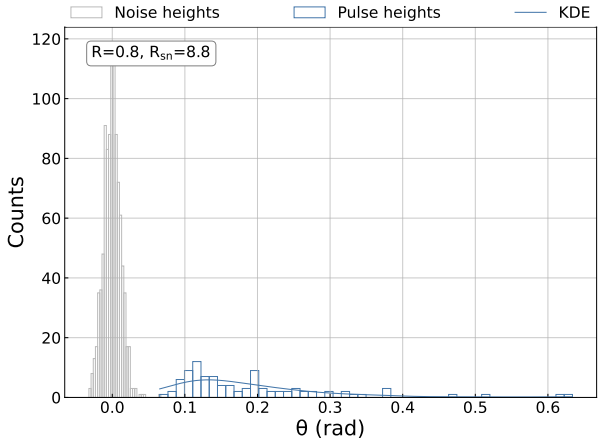

Figure 7.5: The resulting histogram of KID 5 of chip 5 of LT379. This KID is measured for 1 s with a readout power of -102 dBm. We see photon pulses with a large spread in height in this data. As a result, we have a low measured $R = 0.8$. Due to this, it is hard to distinguish the blackbody radiation from noise and cosmic hits.

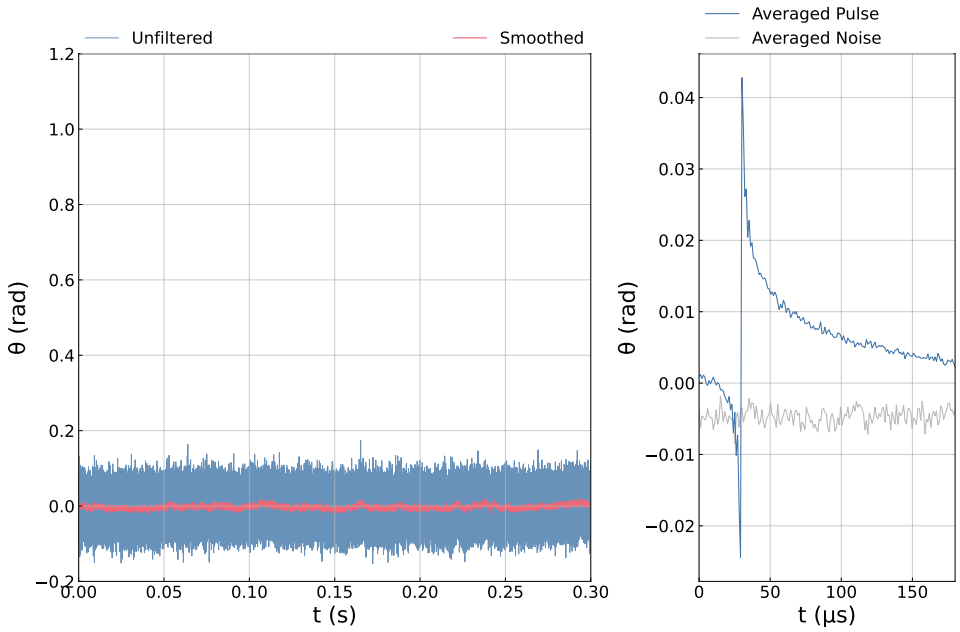

Figure 7.6: The resulting data of KID 5 of chip 5 of LT379 1 day after the previous measurement in figure 7.4. This KID is measured again for 1 s with a readout power of -102 dBm. Here, all the pulses have disappeared. We expect that absorption by Helium-3 from a superleak in the cryostat to be the cause. **Left:** A slice of the time domain data. We smoothed the response with an exponential with $\tau_r = 80\,\mu s$. We can not find any pulses in this time domain. **Right:** This data set's averaged pulse and noise. The averaged pulse is the average of all pulses and not a typical pulse with average peak height in the distribution. We do not find a typical photon pulse shape. Instead, we see a pulse shape that looks like noise spikes with first a sharp negative decay followed by a positive peak.

Power-integrating

We also performed power-integrating measurements for higher blackbody temperatures to find the optical coupling of this KID. This is done for all the KIDs to extract the optical coupling. We show the resulting NEP and η_{opt} of one KID, KID 19, in figure 7.7. The corresponding Cross PSD, including fits, is added in Appendix E. The left panel of figure 7.7 shows the phase PSD. We see 1/f TLS noise for lower frequencies. We see a white power-dependent spectrum at 2500 Hz. We assume that this is photon noise, although it is not the best sample, as there is no clear roll-off after. The middle panel of figure 7.7 shows the NEP calculated in the setup as function of absorbed power. The NEP of this KID is relatively high compared to other KIDs [12]. The right panel of figure 7.7 shows the optical coupling, which is calculated using equation 7.8, for different blackbody powers. We calculate the average optical coupling with a weighted mean, with the errors of the optical couplings as weights. The average optical coupling of this KID is found to be 1.67.

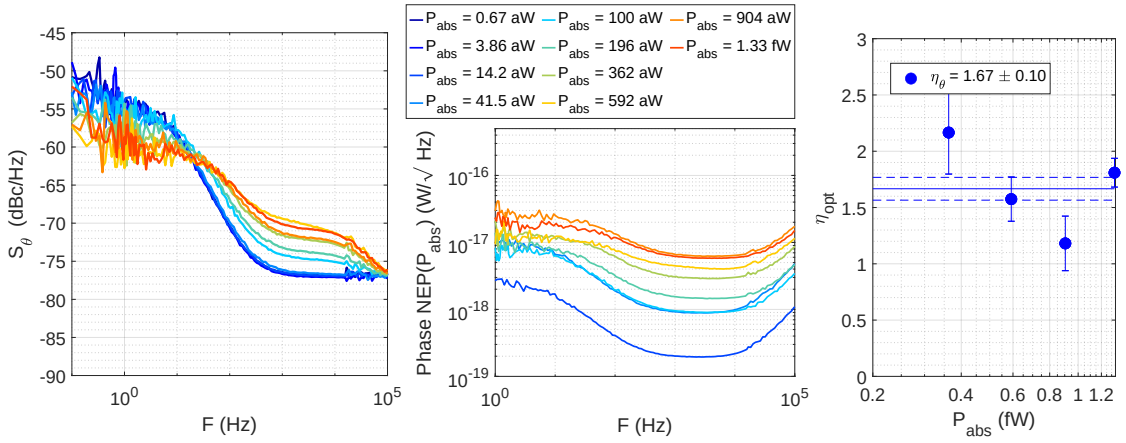

Figure 7.7: The results of the power-integrating measurement for KID 19, which is readout at -104 dBm. The legend of the center panel applies to both the left and center panels. **Left:** The phase PSD. We assume that we are photon noise limited around 2500 Hz, because the spectrum is white and power dependent at that frequency. However, it is not the best sample, as there is no clear roll-off after. **Center:** The measured NEP as a function of frequency for the different absorbed powers. **Right:** The extracted optical coupling at 2500 ± 50 Hz as function of blackbody power. We calculate the average optical coupling with a weighted mean, with the errors of the optical couplings as weights. We only use the higher powers for the fit, as these show photon noise. This coupling is slightly lower than the expected $\eta_{opt} = 1.77$, including silicon absorption.

The total overview of the optical coupling for all the measured KIDs is shown in figure 7.8. We have also plotted the expected coupling. For this, we use the values η_x=1.01 and η_y=1.06, as calculated in section 6.4. We need to sum these two to find the total expected optical coupling, as η_{opt} in equation 7.8 is calculated with respect to one polarization. Thus, we expect η_{opt}=2.07. However, we did not consider absorption in the silicon in the calculation of this coupling. We find $\eta_{opt} \approx 1.77$ with silicon absorption. This value is plotted in figure 7.8 as the expected coupling.

The expected coupling only falls within 2 of the measured KIDs error bounds. 2 KIDs are below the expected coupling, of which one is really close, and 2 KIDS have an coupling higher than the expected coupling. We do not know the exact cause of the spread of the absorption coupling. It may be that we are not using a photon-limited noise case, so equation 7.8 does not hold, and the coupling is thus not correct. This can also be seen in the left panel of figure 7.7, as there is no clear roll-off, so we are likely not completely background limited.

7.2.2. $25\,\mu\text{m}$ lens absorbed coupled KID on membrane

To test that phonon losses cause a large spread in peak heights of the previously measured chip, we also measured chip 8 of LT321. This chip also has lens-absorber coupled KIDs. The absorbers for these KIDs have been optimized for 12 THz ($25\,\mu\text{m}$) with a similar procedure as described in 3.1. The resonance frequency has been tuned with the same method as defined in section 4.1. The main difference between this chip and the chips designed in this work is that the KIDs of LT321 are made on a 150 nm SiC membrane instead of a $350\,\mu\text{m}$ Si substrate. KIDs on a membrane have fewer phonon

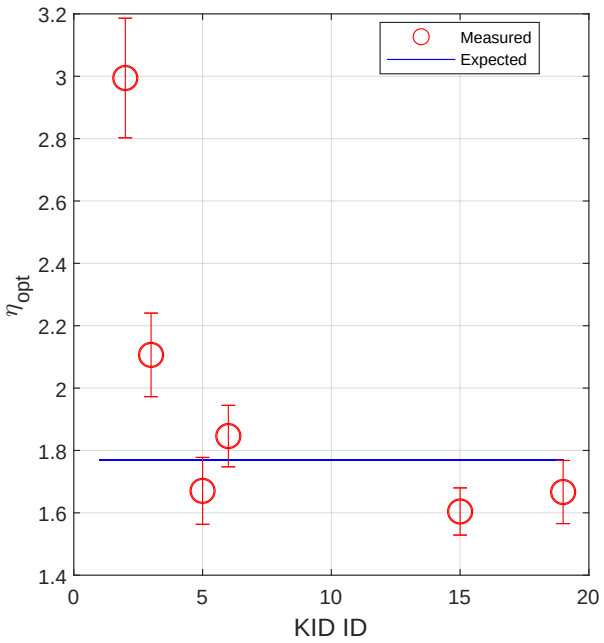

Figure 7.8: The measured couplings for all the KIDs at $f = 2500 \pm 50$ Hz of chip 5 of LT379. The expected coupling, including the absorption in silicon, is plotted as well. We see that the expected coupling matches 2 KIDS. For the other KIDs, we have 2 KIDs with too-high coupling and 2 KIDs with too-low coupling. A possible reason could be that the PSD is not photon noise limited, and equation 7.8, which is used to calculate η_{opt}, does not hold.

losses and thus a lower energy spread due to a lower value of J. J, the phonon loss factor as described in equation 4.12, is typically <0.5 on a membrane [40]. Therefore, we expect this chip to perform better in single-photon counting, i.e., it will have a higher R than the previously measured chip.

We can not accurately predict the optical coupling of this detector. The reason for this is that the unit cells are too large for the wavelength of $18.5\,\mu\text{m}$. We do not meet the requirement in equation 2.19. We are thus exciting higher-order Floquet modes. Therefore, the simulation technique used in this work is not valid, and we cannot simulate the optical coupling of this detector. Here, we will only compare the optical coupling for power-integrating and photon counting experiments.

Single-photon counting

For KID 4, we measured the response for different blackbody temperatures. The other parameters are constant: P_{read} = -104dBm, $t_{\text{measurement}} = 100$ s, the minimum threshold is 0.1 rad, and the maximum threshold is 0.3 rad. The time domain data and corresponding histograms are shown in figures 7.9 and 7.10, respectively. We see a clear rise in the counts per second until 65K. For higher temperatures, the pulses start to overlap. As a result, the resolving power drops as we can not accurately determine the peak height anymore. We also see a stagnancy in the counts per second for higher blackbody temperatures. This is because the peaks are not prominent enough anymore to fulfill the MPH requirement and are thus not counted by the algorithm. The 70 K panel of figure 7.9 shows an example of this at 0.01 s. Here, it can be seen that there are multiple peaks shortly after each other, but they are not prominent enough to be counted as photons.

The resolving power in figure 7.10 is higher than that of the substrate KIDs. The found resolving power approximately matches the expected value for R_{phonon} of 3.98 based on [40], meaning that phonons are indeed the limiting effect on the resolving power.

For these measurements, we also evaluated the optical coupling. We found the absorber power in the kid by multiplying the counts per second N_{ph} by the energy of the photons E_{ph}, i.e. $P_{abs} = N_{ph}E_{ph}$. We used a fit of equation 6.4 to find η_{opt}. As we have a relatively high resolving power and counts per second, we know that we are measuring $18.5\,\mu\text{m}$ photons. Therefore, we only integrate the power of equation 6.4 over the inband of the $18.5\,\mu\text{m}$ band pass filter, which is between $18.01\,\mu\text{m}$ and $19.68\,\mu\text{m}$.

The resulting fit of $\eta_{opt} = 4.0$ is shown in figure 7.11. We did not use the $T_{BB} = 70$ K data for this fit, as

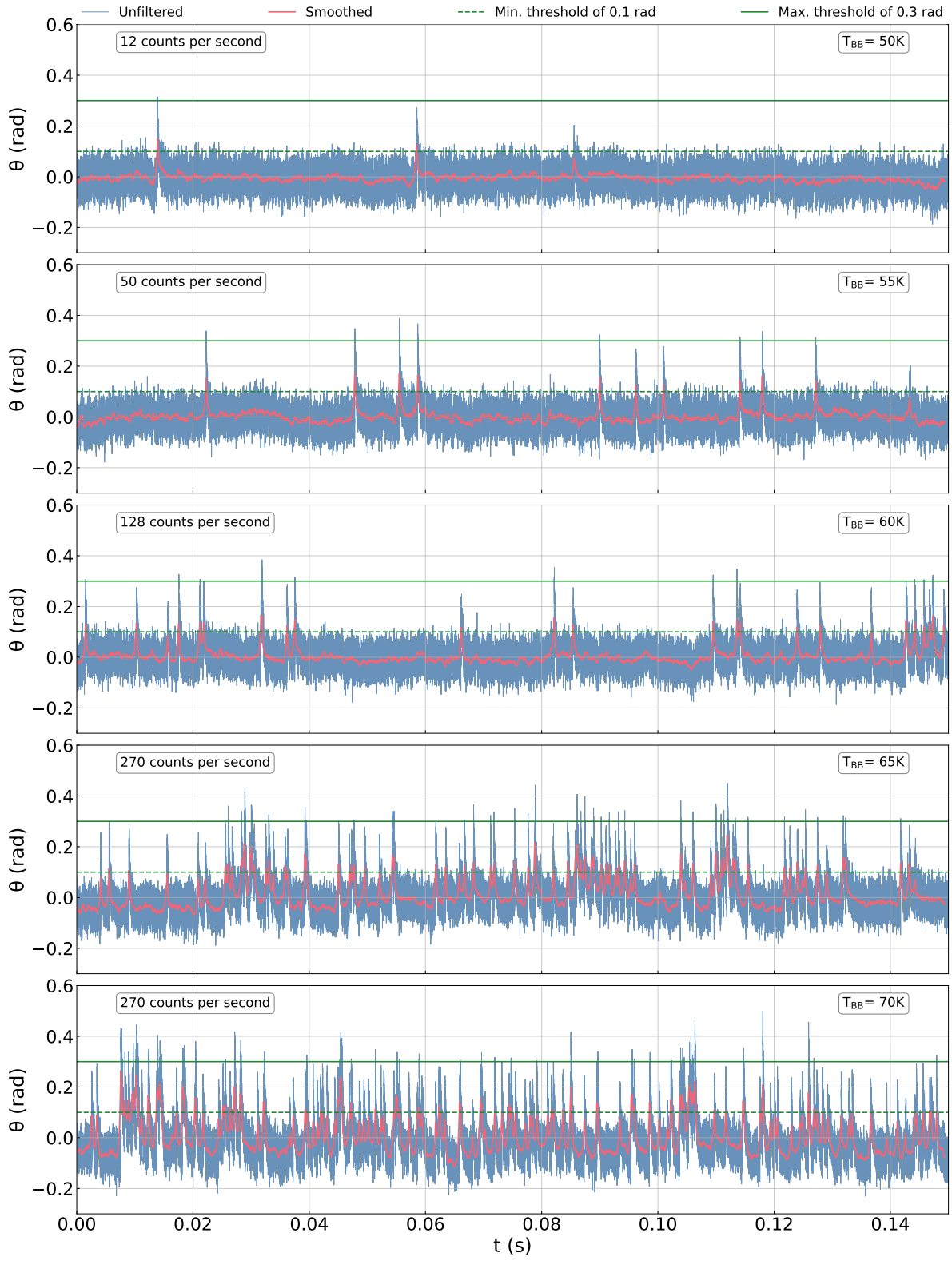

Figure 7.9: A slice of the time domain of KID 4 measured for blackbody temperatures of 50, 55, 60, 65, and 70 K. The readout power is -104dBm. Data is filtered with $\tau_r = 200\,\mu\mathrm{m}$. The measured total time is 100 seconds. The sample rate is 1 MHz. We use a minimum threshold of 0.3 rad and an exponential filter with $\tau_r = 200\,\mu\mathrm{m}$. The number of counts per second is added as insets in the panel. For this number of counts, we still consider all pulses, including overlapping pulses, if they fulfill both requirements in terms of minimum peak prominence and minimum peak height. We see a clear rise in the number of photons until 65 K. At 70 K, the pulses start to overlap. This can be seen at 0.01 s where it looks like multiple photons are absorbed shortly after each other. Due to this, they are not prominent enough to be considered as pulse and are not selected by the algorithm. The corresponding histograms are shown in 7.10.

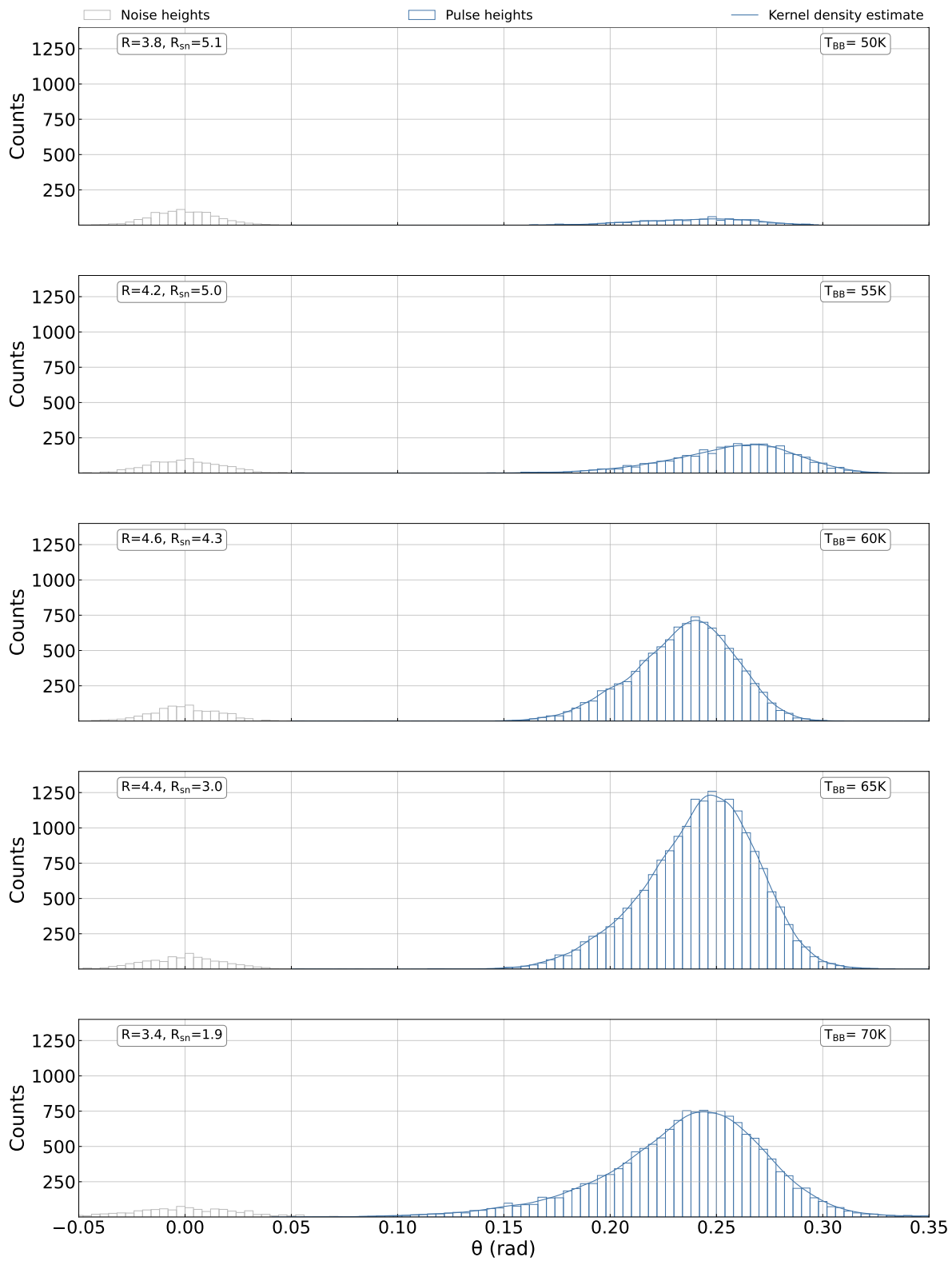

Figure 7.10: The histograms of KID 4 measured for blackbody temperature of 50,55,60,65 and 70K. The readout power is -104dBm. The measured total time is 100 seconds. The sample rate is 1 MHz. We use a minimum threshold of 0.3 rad and an exponential filter with $\tau_r = 200\,\mu\mathrm{m}$. We see a clear rise in the counts and resolving power until 65K. For 65 and 70 K, pulses overlap. As a result, we can not determine the peak heights less accurately, and thus the resolving power drops. The number of counts in the histogram also drops for overlapping pulses, as we reject the second pulse of the two pulses in a situation for the optimal filter. This is thus due to the analysis method. Figure 7.9 shows the corresponding time domain data.

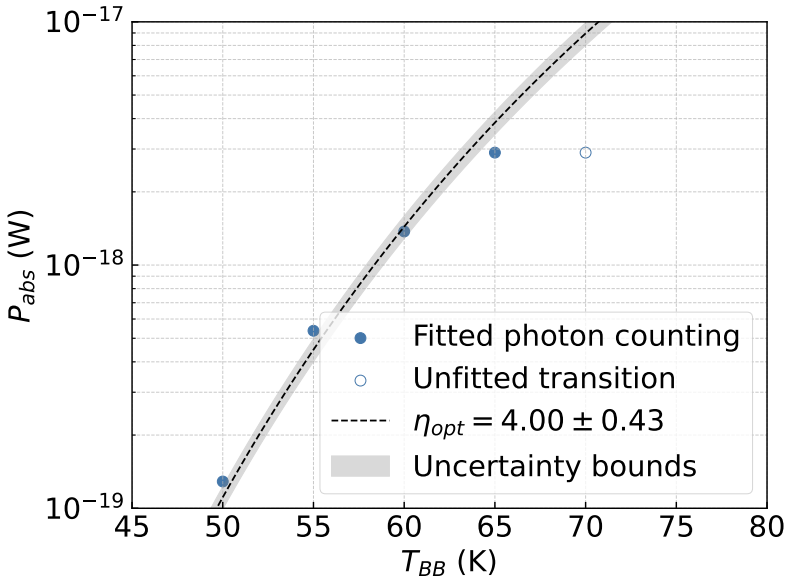

Figure 7.11: The calculated absorbed powers fitted with equation 6.4 for the in-band power of the filter stack. We do not use the data point of 70K, as this data point is in the transition area of photon counting and power-integrating. We find $\eta_{opt} = 4.0$. This is lower than the coupling from the power-integrating measurements, which is shown in figure 7.13. We believe this is due to the discreteness of photon counting, making photon counting more prone to noise or lost pulses compared to power integrating measurements.

the transition between photon counting and power-integrating is already occurring at this temperature.

Power-integrating

We performed power-integrating measurements for the KIDs of LT321. The resulting NEP and optical coupling for KID 2, readout at -99 dBm, is shown in figure 7.12. The corresponding Cross PSD, including fits, is added in Appendix E.

The NEP of the membrane KIDs is lower compared to the substrate KIDs. We also extracted an optical coupling for this KID. The optical coupling is extracted at 200 ± 50 Hz, as photon noise dominates the PSD in this range. This measurement shows an optical coupling of $\eta = 5.13 \pm 0.11$. This number is larger than 1 as the coupling is calculated with respect to the maximum absorbed power of a single-mode device, which is sensitive to 1 polarization.

η_{opt} from the single-photon counting experiments in figure 7.11 is lower than the coupling measured from the power-integrating measurements in figure 7.13. A factor that can play a role is that the highest transmission of the filters is not at $18.5\,\mu\mathrm{m}$, but at a slightly larger value of $\approx 18.7\ \mu\mathrm{m}$, such that the energy of the photons is not correct. This shift can be even larger than expected, as most filters are only characterized at room temperature. This effect is also amplified by the blackbody for lower temperatures as the blackbody radiates longer wavelengths at lower temperatures, as seen in figure 6.3. However, this effect is too small to explain the lower coupling.

Most likely, we are measuring a lower coupling for single-photon counting experiments due to the discreteness in the experiments. In photon counting, you either measure or do not measure a photon. As a result, photon counting is more prone to noise or lost pulses than power-integrating measurements. These lost pulses can be caused by the algorithm, such as a wrong minimum peak height or a wrong minimum peak prominence. This results in a lower coupling for photon counting experiments.

7.3. Measurement conclusion

The chip with lens-absorber coupled KIDs on a membrane, LT321, has an identical design procedure as the chip with lens-absorber coupled KIDs, LT379, on a substrate. The membrane chip shows a high resolving power $R \approx 4$ compared to the substrate chip, which has an $R < 1$. We attribute this to

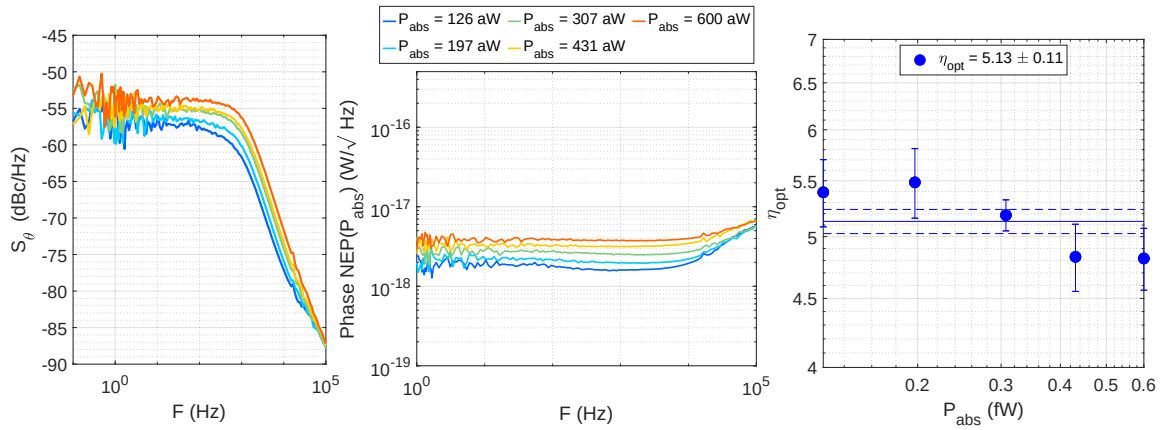

Figure 7.12: The results of the power-integrating measurement for KID 2, which is readout at -99 dBm. The legend of the center panel applies to both the left and center panels. **Left:** The phase PSD. We assume that we are photon noise limited around 200 Hz, because the spectrum is white and power dependent at that frequency with a clear roll-off after. **Center:** The measured NEP as a function of frequency for the different absorbed powers. This NEP is lower than the measured NEP of the KIDs on a substrate. **Right:** The extracted optical coupling at 200 ± 50 Hz as function of blackbody power. We calculate the average optical coupling with a weighted mean, with the errors of the optical couplings as weights. All measured powers are used for this fit, as all show photon noise.

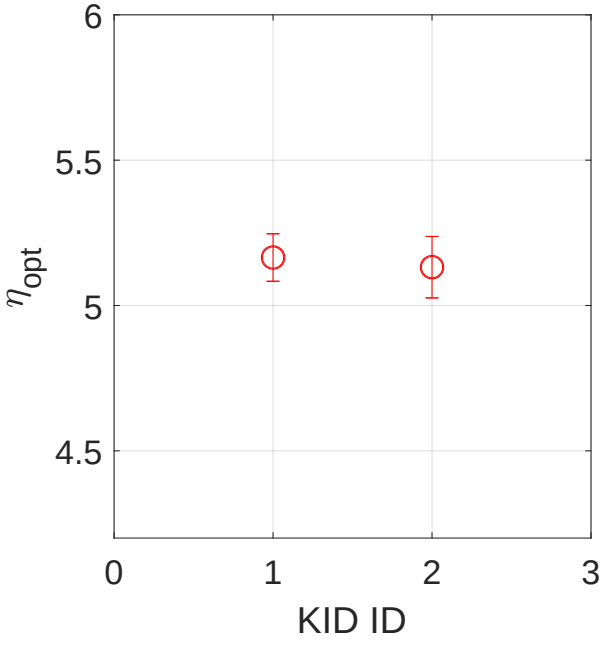

Figure 7.13: The couplings of the two KIDs measured in power-integrating measurements at $f = 200 \pm 50$ Hz of chip 8 of LT321. The expected coupling is not known as the simulation technique in this work is not valid due to excited higher-order Floquet modes.

phonon losses as we expect that $R_{\text{phonon}} = 3.98$ for the membrane KIDs and $R_{\text{phonon}} = 1.67$ for KIDs on a substrate based on similar measurements from [40].

We also calculated the optical coupling for both chips. The substrate chip showed a large spread in the couplings for different KIDs. Only 2 KIDs are within the error bounds, and one KID has an optical coupling that differs by a factor of two from the expected coupling. This is probably because we are not entirely background limited, as can be seen from the phase response in the left panel of figure 7.7, where there is no clear roll-off after the photon noise at 2500 Hz.

We can not compare the measured optical coupling of the membrane chip detectors to a simulated one, as the simulation used is not valid due to excited higher-order Floquet modes. The photon counting measurements show a lower coupling than that from power-integrating measurements. The most plausible cause is that photon counting experiments are more prone to noise and lost pulses, due to the discrete nature of photon detection.

8

Conclusion and recommendations

In this thesis, we designed two lens-absorber coupled KIDS for two wavelengths: 10 and $18.5\,\mu\mathrm{m}$. The goal during the design was to increase the optical coupling for KIDS for the mid-IR wavelengths while maintaining sensitivity. These KIDs (or their successors) could be used for mid-IR missions such as LIFE (4-$18.5\,\mu\mathrm{m}$). The aluminum absorbers have been optimized using the Floquet model in CST. We find absorption efficiencies for the TE and TM fundamental Floquet modes of up to 81% and 65% for the $18.5\,\mu\mathrm{m}$ design and the $10\,\mu\mathrm{m}$ design, respectively. After optimization of the absorber, the resonance frequency was tuned with an NbTiN CPW. A total of 4 designs have been made. Two for $18.5\,\mu\mathrm{m}$ and two for $10\,\mu\mathrm{m}$. For each wavelength, two variations have been made with a difference in the width of the absorber to reduce fabrication risks. Moreover, a varying width also means a different volume and thus noise and peak height. All the designs have been fabricated successfully.

Measurements

One of the designs for $18.5\,\mu\mathrm{m}$ with an absorber of 5 by 5 unit cells, LT379 chip 5, with widths: $w_x = 1.7\lambda f_{\#}$ and $w_x = 1.9\lambda f_{\#}$, has been measured. The KIDs on this chip showed a low resolving power: $R < 1$. As a result, it was impossible to distinguish the blackbody photons from noise and cosmic rays. We attribute this to phonon losses. This is consistent with other measurements with a similar setup in [40]. Therefore, another chip, LT321 chip 8, was measured. This chip also has lens-absorber coupled KIDs with similar fabrication and design processes, but was made on a membrane. KIDs on this chip showed relatively high resolving powers of $R \approx 4$. This matches the expected resolving power due to phonon losses of 3.98 based on [40]. We conclude that phonon losses were the main cause of the low resolving power in the KIDs made on a substrate.

The optical coupling of the absorbers designed in this thesis was calculated from the measurement. We find for the 6 KIDs efficiencies of: 1.60 ± 0.07, 1.66 ± 0.10, 1.67 ± 0.10, 1.85 ± 0.10, 2.10 ± 0.13, and 2.99 ± 0.19. This coupling is calculated with respect to the maximum power that can be absorbed in 1 spatial mode and 1 polarization. The absorber that we designed is a multi-moded device and can thus have a coupling larger than 1. We attribute the spread and the outliers in the found values to the fact that we are not totally photon noise dominated.

The found optical couplings are a reasonable match to the expected efficiency of approximately 1.77. However, this number is not optimal yet. We still lose around 40% to reflection at the lens surface and around 14% to absorption in silicon. This means that by choosing a transparent material and an anti-reflection coating, we can improve this number by almost a factor of 2. We can also improve the efficiency by including a backshort, which will improve the efficiency by approximately 30%.

We can not compare the measured optical coupling of the membrane chip detectors to a simulated one, as the simulation used is not valid due to excited higher-order Floquet modes. The measured coupling for the photon counting experiments was lower than for power integrating. We attribute this to the discreteness in the experiments. You either count a photon or you don't. As a result, photon counting experiments are more prone to noise and lost pulses. These pulses can be lost by the algorithm or the

wrong minimum peak height or minimum peak prominence.

Material tolerance of absorbers
In this work, the material tolerance of absorbers was researched. For this, the thickness and, thus, the surface impedance of the aluminum absorber was varied in an existing absorber design. The changing thickness hardly varied the absorption efficiency. This means that the absorption is mainly determined by its geometric inductance and capacitance, not material properties.

Effect of absorption due to scattering time
Similar to the material tolerance, the effect of the scattering time on the absorption efficiency was researched. This was done for a surface impedance considering scattering via the Drude model. To model the impact, τ was varied around its free electron model value of 0.15 fs for 23 nm thick aluminum. It was concluded that the scattering time does influence the absorption efficiency. However, this influence does not dominate compared to other variations, such as material thickness or resistivity uncertainties.

Effect of current inhomogeneities within absorbers on the resolving power
Local current inhomogeneities in the inductor can affect the response of KIDs if the length scale of the current inhomogeneity is larger than the distance quasiparticles can travel due to diffusion. This means that the difference in current inhomogeneity and, thus, the response can cause the resolving power to decrease. This effect was modeled as part of this work.

From this model, we conclude that inhomogeneities in absorbers do not influence the resolving power. However, an area connects the absorber to the feed, where quasiparticles can diffuse. This area has a very low current density, so quasiparticles do not contribute to the response in that area. This results in large spread of energy. Therefore, this area must be made as small as possible in future KID designs. Another option is to create an extra long and narrow line that connects the absorber to the aluminum part of the feed. The current density in this narrow line will be high. Therefore, quasiparticles can not diffuse to areas where their response is lost. This increases the efficiency and resolving power of the detector.

Backshort
The optical coupling of lens-absorbed coupled KIDs can be increased by roughly 1.3 by adding a $\lambda/4$ backing reflector. This work discussed the fabrication process of a backshort, including mask designs. These backshort designs include an etch in the silicon of the backshort chip to reduce TLS noise. However, the proposed technique using a KOH etch does not work. Therefore, a new RIE etch method was developed, resulting in fabricated backshorts for the $18.5\,\mu\mathrm{m}$ design. Future work should include these backshorts in measurements to test the effect of the backshorts.

The change of method for the backshort also means that the mask designs are incorrect. Therefore, the mask designs must be updated with new markers and dimensions for the silicon etch for the new process.

Recommendations
Membrane
The primary recommendation of this work is to focus on the design of lens-absorber coupled KIDs made on membranes for the mid-infrared due to their low phonon losses. Future work should re-optimize the absorber designs presented in this thesis for the case of a membrane.

Redesigning the lens
The lens used in this work is one previously made for 12 THz. This lens should be redesigned in future work to increase the optical coupling of the detector. The lens design should be made for use in a membrane KID design.

Backshort

The absorption efficiency can theoretically be increased by approximately 30% by adding a backshort. Future work should use a backshort to increase the absorption efficiency and measure its effect in reality.

Cryogenic Fourier transform spectrometer measurements

Other next steps can include better measurement of the optical coupling and the filter transmission. The current method extracts the optical coupling from the total KID measurement. However, this extracted efficiency is influenced by noise, phonon losses, etc. We also only know the filter transmission at room temperature, not cryogenic temperatures. Therefore, another type of measurement would be beneficial to compare the optical coupling and measure the filter transmission cryogenically.

For this purpose, a Fourier transform spectrometer (FTS) could be used with a method similar to [11]. In this work, they measured the filter transmission cryogenically using an FTS. They also measured the absorption of the absorber made on a silicon substrate. The silicon cavity under the absorber acts like a Fabry-Perot interferometer. As a result, there will be nulls and peaks in the transmission. The absorption of the absorber can be calculated from the nulls and peaks. A main advantage of this method is that it yields an absorption efficiency as a function of frequency.

New material for lens and substrate

The lens and substrate material of the KIDs presented in this thesis is silicon. This is the primary material for KIDs at SRON, which has developed fabrication processes for silicon substrates and lenses. However, silicon shows strong absorption peaks in the mid-infrared. The absorption can go up to more than 40% at $\approx 16\,\mu\mathrm{m}$. Phonons cause these, and these can thus not be removed by using higher-purity silicon. We thus need to use other materials.

Currently, there is no transparent material that covers the entire wavelength band of LIFE. In Appendix F a literature study is added on both currently used and new materials for mid-infrared. The conclusion of this research is to use the following materials within the LIFE wavelength band:

- 4-7 $\mu\mathrm{m}$: Silicon.
- 7-13 $\mu\mathrm{m}$: Germanium.
- 13-18.5 $\mu\mathrm{m}$: Diamond.

Future work should look at designing and fabricating lenses and substrates with these materials.

Matching layer

No matching layer was added to the lenses in this work. As a result, approximately 40% of the power is reflected. Future work should add a matching layer to increase the optical coupling of the detector. A feasible option is a diamond quarter-wavelength anti-reflection coating. It is discussed in the material literature study in Appendix F.

References

[1] Lee Feinberg, John Ziemer, Megan Ansdell, Julie Crooke, Courtney Dressing, Bertrand Mennesson, John O'Meara, Joshua Pepper, and Aki Roberge. "The Habitable Worlds Observatory engineering view: status, plans, and opportunities". In: *Space Telescopes and Instrumentation 2024: Optical, Infrared, and Millimeter Wave*. Vol. 13092. SPIE. 2024, pp. 511–522.

[2] B Scott Gaudi, Sara Seager, Bertrand Mennesson, Alina Kiessling, Keith Warfield, Kerri Cahoy, John T Clarke, Shawn Domagal-Goldman, Lee Feinberg, Olivier Guyon, et al. "The Habitable Exoplanet Observatory (HabEx) mission concept study final report". In: *arXiv preprint arXiv:2001.06683* (2020).

[3] LUVOIR Team et al. "The LUVOIR mission concept study final report". In: *arXiv preprint arXiv:1912.06219* (2019).

[4] Wilbert Ras. "Microwave Kinetic Inductance Detectors For The Mid-Infrared". Available online at `https://repository.tudelft.nl/islandora/object/uuid:8cf9cabb-7348-4eb6-b93e-7dde0b143091`. Master's Thesis. Delft, Netherlands: Delft University of Technology, Nov. 2022.

[5] Lisa Kaltenegger. "How to Characterize Habitable Worlds and Signs of Life". In: *Annual Review of Astronomy and Astrophysics* 55.1 (Aug. 2017), pp. 433–485. ISSN: 1545-4282. DOI: `10.1146/annurev-astro-082214-122238`. URL: `http://dx.doi.org/10.1146/annurev-astro-082214-122238`.

[6] Franck Selsis, Lisa Kaltenegger, and Jimmy Paillet. "Terrestrial exoplanets: diversity, habitability and characterization". In: *Physica Scripta* 2008.T130 (July 2008), p. 014032. DOI: `10.1088/0031-8949/2008/T130/014032`. URL: `https://dx.doi.org/10.1088/0031-8949/2008/T130/014032`.

[7] NASA. *What is an Exoplanet? Overview*. `https://exoplanets.nasa.gov/what-is-an-exoplanet/overview/`. [Online; accessed 6-June-2024]. 2024.

[8] Sascha Patrick Quanz, Marcel Ottiger, E Fontanet, Jens Kammerer, Franziska Menti, Felix Dannert, A Gheorghe, Olivier Absil, Vladimir S Airapetian, Eleonora Alei, et al. "Large Interferometer For Exoplanets (LIFE)-I. Improved exoplanet detection yield estimates for a large mid-infrared space-interferometer mission". In: *Astronomy & Astrophysics* 664 (2022), A21.

[9] Felix A Dannert, Maurice Ottiger, Sascha P Quanz, Romain Laugier, Emile Fontanet, Adrian Gheorghe, Olivier Absil, Colin Dandumont, Denis Defrère, Carlos Gascón, et al. "Large Interferometer For Exoplanets (LIFE)-II. Signal simulation, signal extraction, and fundamental exoplanet parameters from single-epoch observations". In: *Astronomy & Astrophysics* 664 (2022), A22.

[10] Peter K Day, Henry G LeDuc, Benjamin A Mazin, Anastasios Vayonakis, and Jonas Zmuidzinas. "A broadband superconducting detector suitable for use in large arrays". In: *Nature* 425.6960 (2003), pp. 817–821.

[11] Peter K. Day, Nicholas F. Cothard, Christopher Albert, Logan Foote, Elijah Kane, Byeong H. Eom, Ritoban Basu Thakur, Reinier M. J. Janssen, Andrew Beyer, Pierre Echternach, Sven van Berkel, Steven Hailey-Dunsheath, Thomas R. Stevenson, Shahab Dabironezare, Jochem J. A. Baselmans, Jason Glenn, C. Matt Bradford, and Henry G. Leduc. *A 25-micron single photon sensitive kinetic inductance detector*. 2024. arXiv: `2404.10246 [astro-ph.IM]`. URL: `https://arxiv.org/abs/2404.10246`.

[12] JJA Baselmans, F Facchin, A Pascual Laguna, J Bueno, DJ Thoen, V Murugesan, Nuria Llombart, and PJ De Visser. "Ultra-sensitive THz microwave kinetic inductance detectors for future space telescopes". In: *Astronomy & Astrophysics* 665 (2022), A17.

[13] Kevin Kouwenhoven, Daniel Fan, Enrico Biancalani, Steven AH De Rooij, Tawab Karim, Carlas S Smith, Vignesh Murugesan, David J Thoen, Jochem JA Baselmans, and Pieter J De Visser. "Resolving power of visible-to-near-infrared hybrid β-Ta/Nb-Ti-N kinetic inductance detectors". In: *Physical Review Applied* 19.3 (2023), p. 034007.

[14] Mohanakrishna Ranganathan, Adrian M. Glauser, Thomas Birbacher, Adrian A. Gheorghe, and Sascha P. Quanz. “The Nulling Interferometer Cryogenic Experiment: I”. In: *Optical and Infrared Interferometry and Imaging VIII*. Ed. by Antoine Mérand, Stephanie Sallum, and Joel Sanchez-Bermudez. Vol. 12183. International Society for Optics and Photonics. SPIE, 2022, p. 121830L. DOI: 10.1117/12.2629514. URL: https://doi.org/10.1117/12.2629514.

[15] D. Roos. “Design of Lens-Absorber Coupled Microwave Kinetic Inductance Detectors at 1.5 THz and Evaluation of their Quasi-Optical Coupling for Far-Infrared Spectroscopic Astronomical Observations”. Master thesis. Delft University of Technology, 2024. URL: http://resolver.tudelft.nl/uuid:92a1267c-5e3b-4f33-9e92-d242a9466bee.

[16] Pieter Jan de Visser. “Quasiparticle dynamics in aluminium superconducting microwave resonators”. Ph.D. Thesis. Delft, The Netherlands: Technische Universiteit Delft, Mar. 2014. DOI: 10.4233/uuid:eae4c9fc-f90d-4c12-a878-8428ee4adb4c.

[17] Jacques I. Pankove and David A. Kiewit. “Optical Processes in Semiconductors”. In: *Journal of The Electrochemical Society* 119.5 (May 1972), 156Ca. DOI: 10.1149/1.2404256. URL: https://dx.doi.org/10.1149/1.2404256.

[18] Kevin Kouwenhoven. “Visible to Near-Infrared Kinetic Inductance Detectors”. PhD thesis. Delft University of Technology, 2025.

[19] Cornelis Jacobus Gorter and Hendrik Casimir. “On supraconductivity I”. In: *Physica* 1.1-6 (1934), pp. 306–320.

[20] D. C. Mattis and J. Bardeen. “Theory of the Anomalous Skin Effect in Normal and Superconducting Metals”. In: *Phys. Rev.* 111 (2 July 1958), pp. 412–417. DOI: 10.1103/PhysRev.111.412. URL: https://link.aps.org/doi/10.1103/PhysRev.111.412.

[21] R Barends. “Photon-detecting superconducting resonators”. Undefined/Unknown. Dissertation (TU Delft). Delft University of Technology, 2009. ISBN: 978-90-8593-052-5.

[22] Jiansong Gao, J Zmuidzinas, A Vayonakis, P Day, B Mazin, and H Leduc. “Equivalence of the effects on the complex conductivity of superconductor due to temperature change and external pair breaking”. In: *Journal of Low Temperature Physics* 151.1 (2008), pp. 557–563.

[23] AR Kerr. “Surface impedance of superconductors and normal conductors in EM simulators”. In: *MMA Memo* 21.245 (1999), pp. 1–17.

[24] Paul Drude. “Zur elektronentheorie der metalle; II. Teil. galvanomagnetische und thermomagnetische effecte”. In: *Annalen der physik* 308.11 (1900), pp. 369–402.

[25] Paul Drude. “Zur elektronentheorie der metalle”. In: *Annalen der Physik* 312.3 (1902), pp. 687–692.

[26] Steven H Simon. *The Oxford solid state basics*. OUP Oxford, 2013.

[27] Logan Foote, Chris Albert, Ritoban Basu Thakur, Nicholas Cothard, Peter Day, Steven Hailey-Dunsheath, Pierre Echternach, Byeong Ho Eom, Reinier M. Janssen, Elijah Kane, Henry Leduc, Lun-Jun Liu, Hien Nguyen, Jason Glenn, Charles Bradford, and Jonas Zmuidzinas. “Highly sensitive far-IR KIDs for PRIMA: optical characterization of a 25-micron array”. In: *Millimeter, Submillimeter, and Far-Infrared Detectors and Instrumentation for Astronomy XII*. Ed. by Jonas Zmuidzinas and Jian-Rong Gao. Vol. 13102. International Society for Optics and Photonics. SPIE, 2024, p. 131020D. DOI: 10.1117/12.3020228. URL: https://doi.org/10.1117/12.3020228.

[28] Beatriz Blazquez, Nuria Llombart, Daniele Cavallo, Angelo Freni, and Andrea Neto. “A rigorous equivalent network for linearly polarized THz absorbers”. In: *IEEE Transactions on Antennas and Propagation* 62.10 (2014), pp. 5077–5088.

[29] Dassault Systèmes. *CST Studio Suite 2022*. https://www.3ds.com/products-services/simulia/products/cst-studio-suite/. Electromagnetic simulation software, accessed July, 2024. 2022.

[30] Nuria Llombart, Beatriz Blázquez, Angelo Freni, and Andrea Neto. “Fourier optics for the analysis of distributed absorbers under THz focusing systems”. In: *IEEE Transactions on Terahertz Science and Technology* 5.4 (2015), pp. 573–583.

[31] Nuria Llombart, Shahab Oddin Dabironezare, Giorgio Carluccio, Angelo Freni, and Andrea Neto. “Reception Power Pattern of Distributed Absorbers in Focal Plane Arrays: A Fourier Optics Analysis”. In: *IEEE Transactions on Antennas and Propagation* 66.11 (2018), pp. 5990–6002. DOI: 10.1109/TAP.2018.2862359.

[32] A. Neto, N. Llombart, and D. Cavallo. *Figure from notes from EE4725 Quasi optical systems Course*. TU Delft MSc course.

[33] D. Cavallo. “Connected array antennas : analysis and design”. English. Phd Thesis 1 (Research TU/e / Graduation TU/e). Electrical Engineering, 2011. ISBN: 978-94-6191-035-6. DOI: 10.6100/IR719461.

[34] Kristen Rohlfs and Thomas L Wilson. *Tools of radio astronomy*. Springer Science & Business Media, 2013.

[35] Steven B Kaplan, CC Chi, DN Langenberg, Jhy-Jiun Chang, S Jafarey, and DJ Scalapino. “Quasiparticle and phonon lifetimes in superconductors”. In: *Physical Review B* 14.11 (1976), p. 4854.

[36] A. Megrant, C. Neill, R. Barends, B. Chiaro, Yu Chen, L. Feigl, J. Kelly, Erik Lucero, Matteo Mariantoni, P. J. J. O’Malley, D. Sank, A. Vainsencher, J. Wenner, T. C. White, Y. Yin, J. Zhao, C. J. Palmstrøm, John M. Martinis, and A. N. Cleland. “Planar superconducting resonators with internal quality factors above one million”. In: *Applied Physics Letters* 100.11 (Mar. 2012). ISSN: 1077-3118. DOI: 10.1063/1.3693409. URL: http://dx.doi.org/10.1063/1.3693409.

[37] A. Endo and J.J.A. Baselmans. *EE4745 Superconducting Astronomical Instrumentation Course notes*. TU Delft MSc course.

[38] A. G. Kozorezov, A. F. Volkov, J. K. Wigmore, A. Peacock, A. Poelaert, and R. den Hartog. “Quasiparticle-phonon downconversion in nonequilibrium superconductors”. In: *Phys. Rev. B* 61 (17 May 2000), pp. 11807–11819. DOI: 10.1103/PhysRevB.61.11807. URL: https://link.aps.org/doi/10.1103/PhysRevB.61.11807.

[39] Aaron Dantuma. “Pushing the fano limit”. Bachelor’s Thesis. Delft, Netherlands: Delft University of Technology, Jan. 2024.

[40] Pieter J De Visser, Steven AH De Rooij, Vignesh Murugesan, David J Thoen, and Jochem JA Baselmans. “Phonon-trapping-enhanced energy resolution in superconducting single-photon detectors”. In: *Physical Review Applied* 16.3 (2021), p. 034051.

[41] Tejas Guruswamy, David J Goldie, and Stafford Withington. “Quasiparticle generation efficiency in superconducting thin films”. In: *Superconductor Science and Technology* 27.5 (2014), p. 055012.

[42] Pieter J de Visser, JJA Baselmans, Pascale Diener, SJC Yates, A Endo, and TM Klapwijk. “Number fluctuations of sparse quasiparticles in a superconductor”. In: *Physical review letters* 106.16 (2011), p. 167004.

[43] Ugo Fano. “Ionization yield of radiations. II. The fluctuations of the number of ions”. In: *Physical Review* 72.1 (1947), p. 26.

[44] AG Kozorezov, JK Wigmore, D Martin, P Verhoeve, and A Peacock. “Electron energy downconversion in thin superconducting films”. In: *Physical Review B—Condensed Matter and Materials Physics* 75.9 (2007), p. 094513.

[45] Clemens Müller, Jared H Cole, and Jürgen Lisenfeld. “Towards understanding two-level-systems in amorphous solids: insights from quantum circuits”. In: *Reports on Progress in Physics* 82.12 (2019), p. 124501.

[46] Werner Karl-Gustav Daalman. *Noise and loss in superconducting resonators*. MSc. thesis, Delft University of Technology. 2014.

[47] Jochem Baselmans. Personal communication-2024.

[48] SA Hähnle. “Superconducting Integrated Circuits at Sub-millimeter Wavelengths”. PhD thesis. Delft University of Technology, 2021.

[49] David M Pozar. *Microwave engineering: theory and techniques*. John wiley & sons, 2021.

[50] Steven A. H. de Rooij, Remko Fermin, Kevin Kouwenhoven, Tonny Coppens, Vignesh Murugesan, David J. Thoen, Jan Aarts, Jochem J. A. Baselmans, and Pieter J. de Visser. *Recombination of localized quasiparticles in disordered superconductors*. 2024. arXiv: 2410.18802 [cond-mat.supr-con]. URL: https://arxiv.org/abs/2410.18802.

[51] John R Clem and Karl K Berggren. "Geometry-dependent critical currents in superconducting nanocircuits". In: *Physical Review B—Condensed Matter and Materials Physics* 84.17 (2011), p. 174510.

[52] H. L. Hortensius, E. F. C. Driessen, T. M. Klapwijk, K. K. Berggren, and J. R. Clem. "Critical-current reduction in thin superconducting wires due to current crowding". In: *Applied Physics Letters* 100.18 (Apr. 2012). ISSN: 1077-3118. DOI: 10.1063/1.4711217. URL: http://dx.doi.org/10.1063/1.4711217.

[53] Joseph W Goodman. *Introduction to Fourier optics*. Roberts and Company publishers, 2005.

[54] Jochem JA Baselmans, J Bueno, Stephen JC Yates, O Yurduseven, Nuria Llombart, K Karatsu, AM Baryshev, L Ferrari, A Endo, DJ Thoen, et al. "A kilo-pixel imaging system for future space based far-infrared observatories using microwave kinetic inductance detectors". In: *Astronomy & Astrophysics* 601 (2017), A89.

[55] Tonny Coppens. Personal communication-2025.

[56] I A Kaplunov, A I Kolesnikov, G I Kropotov, and V E Rogalin. "Optical Properties of Single-Crystal Germanium in the THz Range". In: *Optics and Spectroscopy* 126.3 (2019), pp. 271–274. DOI: 10.1134/S0030400X19030093.

[57] A Deneuville, D Tanner, and PH Holloway. "Optical constants of ZnSe in the far infrared". In: *Physical review B* 43.8 (1991), p. 6544.

[58] Constantine A Balanis. *Balanis' Advanced Engineering Electromagnetics*. John Wiley & Sons, 2024.

[59] Daan Roos. Personal communication-2025.

[60] Kent David Irwin. *Phonon-mediated particle detection using superconducting tungsten transition-edge sensors*. Stanford University, 1995.

[61] P. Welch. "The use of fast Fourier transform for the estimation of power spectra: A method based on time averaging over short, modified periodograms". In: *IEEE Transactions on Audio and Electroacoustics* 15.2 (1967), pp. 70–73. DOI: 10.1109/TAU.1967.1161901.

[62] David W Scott. *Multivariate density estimation: theory, practice, and visualization*. John Wiley & Sons, 2015.

[63] SH Moseley, John C Mather, and Dan McCammon. "Thermal detectors as x-ray spectrometers". In: *Journal of Applied Physics* 56.5 (1984), pp. 1257–1262.

[64] Megan Elizabeth Eckart. "Measurements of X-ray selected agn and novel superconducting X-ray detectors". PhD thesis. California Institute of Technology, 2007.

[65] Robert W. Boyd. "Photon bunching and the photon-noise-limited performance of infrared detectors". In: *Infrared Physics* 22.3 (1982), pp. 157–162. ISSN: 0020-0891. DOI: https://doi.org/10.1016/0020-0891(82)90034-3. URL: https://www.sciencedirect.com/science/article/pii/0020089182900343.

[66] Lorenza Ferrari, Ozan Yurduseven, Nuria Llombart, Stephen JC Yates, Juan Bueno, Vignesh Murugesan, David J Thoen, Akira Endo, Andrey M Baryshev, and Jochem JA Baselmans. "Antenna coupled MKID performance verification at 850 GHz for large format astrophysics arrays". In: *IEEE Transactions on Terahertz Science and Technology* 8.1 (2017), pp. 127–139.

[67] Stefan Verheul. "Ultra High Sensitivity Microwave Kinetic Inductance Detectors". Available online at https://repository.tudelft.nl/record/uuid:f1ee6108-c165-49da-b63e-daeeb0550570. Master's Thesis. Delft, Netherlands: Delft University of Technology, July 2019.

[68] Christopher K Walker. *Terahertz astronomy*. Crc Press, 2015.

[69] Katie Walker. *Advantages of Silicon for Mid-Wave Infrared Windows*. Novus Light Technologies Today, Accessed: 2024-10-01. 2024. URL: https://www.novuslight.com/advantages-of-silicon-for-mid-wave-infrared-windows_N3441.html.

[70] Edward J Wollack, Giuseppe Cataldo, Kevin H Miller, and Manuel A Quijada. “Infrared properties of high-purity silicon”. In: *Optics Letters* 45.17 (2020), pp. 4935–4938.

[71] Topsil Semiconductor Materials A/S. *Application Note: High Transmission Silicon (HiTran^{TM}) for Infrared Optical Applications*. Accessed: 2024-10-22. Oct. 2013. URL: https://www.topsil.com/wp-content/uploads/2023/05/hitran_application_note_october2013.pdf.

[72] Advanced Coating. *Advanced Coating Parylene Brochure*. Accessed: 2024-10-01. 2021. URL: https://f.hubspotusercontent20.net/hubfs/2001372/Advanced%20Coating%20Parylene%20Brochure%20Aug2021.pdf.

[73] Yongqian Li, Lei Su, Chen Shou, Chunmeng Yu, Jinjun Deng, and Yu Fang. “Surface-enhanced molecular spectroscopy (SEMS) based on perfect-absorber metamaterials in the mid-infrared”. In: *Scientific reports* 3.1 (2013), p. 2865.

[74] Frederick Wooten. *Optical properties of solids*. Citeseer, 1972.

[75] Juan Bueno, Sjoerd Bosma, Tobias Bußkamp-Alda, Maria Alonso-delPino, and Nuria Llombart. “Lossless Matching Layer for Silicon Lens Arrays at 500 GHz Using Laser Ablated Structures”. In: *IEEE Transactions on Terahertz Science and Technology* 12.6 (2022), pp. 667–672. DOI: 10.1109/TTHZ.2022.3202031.

[76] Edmund Optics. *Potassium Bromide (KBr) Windows*. Accessed: 2024-10-01. 2024. URL: https://www.edmundoptics.com/f/potassium-bromide-kbr-windows/14168/.

[77] Edmund Optics. *Sodium Chloride (NaCl) Windows*. Accessed: 2024-10-01. 2024. URL: https://www.edmundoptics.com/f/sodium-chloride-nacl-windows/14170/.

[78] STScI JWST User Documentation. *JWST Mid-Infrared Instrument (MIRI)*. Accessed: 2024-10-01. 2024. URL: https://jwst-docs.stsci.edu/jwst-mid-infrared-instrument#gsc.tab=0.

[79] Edmund Optics. *25.4mm Dia. x 200mm FL, 8-12um AR Coated, ISP Optics Zinc Selenide (ZnSe) PCX Lens*. Accessed: 2024-10-01. 2024. URL: https://www.edmundoptics.com/p/254mm-dia-x-200mm-fl-8-12m-ar-coated-isp-optics-zinc-selenide-znse-pcx-lens/50537/.

[80] Edmund Optics. *Germanium Meniscus Lenses*. Accessed: 2024-10-01. 2024. URL: https://www.edmundoptics.com/f/germanium-meniscus-lenses-d6a8f38e/14775/.

[81] Edmund Optics. *Germanium Plano-Convex (PCX) Lenses*. Accessed: 2024-10-01. 2024. URL: https://www.edmundoptics.com/f/germanium-plano-convex-pcx-lenses/14233/.

[82] HH Li. “Refractive index of silicon and germanium and its wavelength and temperature derivatives”. In: *Journal of Physical and Chemical Reference Data* 9.3 (1980), pp. 561–658.

[83] Coherent. *Polycrystalline CVD Diamond Datasheet*. Accessed: 2024-10-01. 2024. URL: https://www.coherent.com/content/dam/coherent/site/en/resources/datasheet/optics/polycrystalline-cvd-diamond-ds.pdf.

[84] Tydex Optics. *Diamond-Like Carbon (DLC) Coatings*. Accessed: 2024-10-01. 2024. URL: https://www.tydexoptics.com/optical_coatings/dlc/.

[85] Thorlabs. *Polycrystalline CVD Diamond Windows*. Accessed: 2024-10-08. 2024. URL: https://www.thorlabs.com/newgrouppage9.cfm?objectgroup_id=15962.

[86] Edmund Optics. *Diamond-Like Carbon (DLC) Coatings*. Accessed: 2024-10-01. 2024. URL: https://www.edmundoptics.com/capabilities/precision-optics/capabilities/diamond-like-carbon-coatings/.

Acknowledgments

First and foremost, I would like to thank Pieter and Kevin for supervising me throughout this thesis. Pieter, your sarcasm and directness often made me laugh, especially during the review process. This was a unique way to keep things sharp and entertaining. Thank you for that. I also appreciated your constant availability. We even exchanged emails during the Christmas holiday and on Saturday nights, which speaks volumes.

Kevin, your suggestion to write the thesis as if I were explaining it to my past self was incredibly helpful. Thank you for supporting me during this project and answering my many questions. Also, thank you for teaching me something about birds along the way. I wish you the best of luck with your postdoc on mid-IR KIDs. I am sure it will lead to exciting results!

A special thanks to Jochem for sharing his enthusiasm and deep knowledge about Kinetic Inductance Detectors. I want to thank Shahab for explaining the fundamentals of electromagnetics and CST. Appreciation also goes to Daan and Wilbert, my predecessors, whose experience and assistance helped clarify questions that arose along the way. In particular, Daan's help with simulating the absorber performance was really valuable.

I am also grateful to Dimitry, Daniela, Martijn, Tonny, and David for fabricating the KIDs. Your expertise and assistance were crucial in bringing my design from a few pixels on a screen to a detector in real life.

Thanks to the THz group for being so friendly and open and allowing me to organize the Christmas dinner. It was a pleasure to be part of such a welcoming group. Special thanks to my office mates: Peijun, Tom, Marick, and Jurre for their laughs, many coffees, and support I had throughout this journey.

I would also like to thank my friends from Nieuw-Vennep and Delft and my housemates for their support and friendship. Your enthusiasm and many questions about my project made me even more curious and motivated for this project.

Last, but not least, I want to thank my girlfriend Iris and my parents, Anjo and Frederike. Your constant support during this thesis and throughout my life means a lot. I honestly could not have done this without you.

P.C.J.A. van Zweeden
Delft, April 2025

A

Co-planar waveguide characteristic impedance and phase velocity derivation

The following expressions will be used in the derivation:

- $K(\cdot)$ represents the complete elliptic integral of the first kind,
- μ_0 is the permeability of free space,
- ϵ_0 is the permittivity of free space,
- ϵ_r is the relative permittivity of the material,
- S is the gap width
- W is the width of the strip.

The formulae for inductance and capacitance per unit length are given as:

$$L_{g,l} = \frac{\mu_0}{4} \cdot \frac{K\left(\sqrt{1-k^2}\right)}{K(k)} \tag{A.1}$$

$$C_l = 4\epsilon_0\epsilon_{\text{eff}} \cdot \frac{K(k)}{K\left(\sqrt{1-k^2}\right)}, \tag{A.2}$$

where:

$$k = \frac{S}{S+2W}, \tag{A.3}$$

and the effective permittivity is:

$$\epsilon_{\text{eff}} = \frac{1+\epsilon_r}{2}. \tag{A.4}$$

The kinetic inductance of the material is given as sheet kinetic inductance. Via the following geometric contributions, it can be converted to its respective kinetic inductance per unit length. This gives the following expression for the central line:

$$L_{k,c,l} = L_{k,s} \cdot g_c \tag{A.5}$$

With the following expression for the geometric contribution factor for the central plane:

$$g_c = \frac{1}{4S(1-k^2)K^2(k)} \left[\pi + \ln\left(\frac{4\pi S}{d}\right) - k \ln\left(\frac{1+k}{1-k}\right) \right], \tag{A.6}$$

The resulting equation for the ground planes is:

$$L_{k,gp,l} = L_{k,s} \cdot g_g \tag{A.7}$$

With the following expression for the geometric contribution factor for the ground planes:

$$g_g = \frac{k}{4S(1-k^2)K^2(k)} \left[\pi + \ln\left(\frac{4\pi(S+2W)}{d}\right) - \frac{1}{k} \ln\left(\frac{1+k}{1-k}\right) \right]. \tag{A.8}$$

The total kinetic inductance per unit length is then given as the sum of the two:

$$L_{k,l} = L_{k,s} \cdot (g_g + g_c) \tag{A.9}$$

Summing the geometric inductance per unit length and the kinetic inductance per unit length gives the total inductance per unit length of the CPW:

$$L_l = L_{g,l} + L_{k,l} \tag{A.10}$$

Then the characteristic impedance for the CPW can be calculated:

$$Z_{CPW} = \sqrt{\frac{L_l}{C_l}} \tag{A.11}$$

Finally, using the capacitance and inductance per unit length, the phase velocity can be calculated:

$$v_{\text{phase}} = \sqrt{\frac{1}{L_l C_l}} \tag{A.12}$$

B

Kinetic inductance fraction derivation

The kinetic inductance fraction is defined as[16]:

$$\alpha_k = \frac{L_k}{L} = \frac{L_k}{L_g + L_k} = \frac{L - L_g}{L} \tag{B.1}$$

In this equation L_k is the kinetic inductance and L_g is the geometric inductance (the inductance of the structure as PEC). The resonators have one open and one closed end and are thus $\lambda/4$ resonators. Now, the resonance frequencies of a PEC structure and Al structure can be written as functions of the inductance L (or geometric inductance L_g) and capacitance C:

$$f_{Al} = \frac{1}{4l\sqrt{LC}} \tag{B.2}$$

$$f_{PEC} = \frac{1}{4l\sqrt{L_g C}}. \tag{B.3}$$

These can be rewritten to expressions for L and L_g:

$$L_t = \frac{1}{C[4lf_{Al}]^2} \tag{B.4}$$

$$L_g = \frac{1}{C[4lf_{PEC}]^2} \tag{B.5}$$

These expressions can then be substituted into the expression for α_k. This can be done and then simplified to find that α_k is only a function of the resonance frequencies of Al and PEC:

$$\alpha_k = \frac{\frac{1}{C[4lf_{Al}]^2} - \frac{1}{C[4lf_{PEC}]^2}}{\frac{1}{C[4lf_{Al}]^2}} \tag{B.6}$$

$$\alpha_k = \frac{\frac{1}{f_{Al}^2} - \frac{1}{f_{PEC}^2}}{\frac{1}{f_{Al}^2}} \tag{B.7}$$

$$\alpha_k = 1 - \left[\frac{f_{Al}}{f_{PEC}}\right]^2 \tag{B.8}$$

C

Perturbation theory

The specific perturbation theory, in this case, is the cavity perturbation theory. It uses a perturbation to a cavity resonator with volume V_0 and surface S_0. The derivation starts with two situations. The first is the unperturbed situation of a resonator at resonance frequency shown in the left part (a) and the perturbed situation which is shown on the right (b) in figure C.1[49]. The perturbation is added by adding $\Delta\epsilon$ and $\Delta\mu$ to ϵ and μ respectively, which changes the fields from $\bar{E}_0$ and $\bar{H}_0$ to $\bar{E}$ and $\bar{H}$. This also changes the resonance frequency from ω_0 in the unperturbed situation to ω in the perturbed situation.

For both situations, the curl of the fields of the Maxwell equation can be written down as[49]:

$$\nabla \times \bar{E}_0 = -j\omega_0\mu\bar{H}_0, \tag{C.1}$$
$$\nabla \times \bar{H}_0 = j\omega_0\epsilon\bar{E}_0, \tag{C.2}$$
$$\tag{C.3}$$

for the unperturbed situation. Similarly, the curls for the perturbed situation are:

$$\nabla \times \bar{E} = -j\omega(\mu + \Delta\mu)\bar{H}, \tag{C.4}$$
$$\nabla \times \bar{H} = j\omega(\epsilon + \Delta\epsilon)\bar{E}. \tag{C.5}$$

Pozar[49] derived a change in resonance frequency $\omega - \omega_0$ from these Maxwell equations by using a combination of vector identities and the divergence theorem:

$$\frac{\omega - \omega_0}{\omega_0} \simeq -\frac{\int_{V_0} \left(\Delta\epsilon|\bar{E}_0|^2 + \Delta\mu|\bar{H}_0|^2\right) dv}{\int_{V_0} \left(\epsilon|\bar{E}_0|^2 + \mu|\bar{H}_0|^2\right) dv}. \tag{C.6}$$

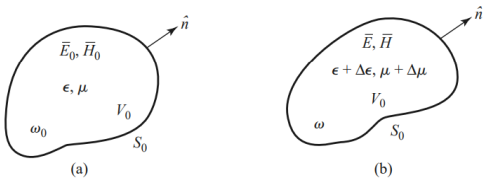

Figure C.1: The material changes due to a perturbation in the material. With this perturbation, the current dependent response can be derived. **Panel a:** shows the original cavity with its parameters. **Panel b** shows the perturbed cavity with its new permittivity, permeability, fields and resonance frequency. Figure adapted from Pozar[49].

The expression for the energy stored, W_e, in the electric field is $W_e = \int_{V_0} \epsilon \left|\bar{E}_0\right|^2$ and the expression for the energy stored in the magnetic field, W_m, is $W_m = \int_{V_0} \mu \left|\bar{H}_0\right|^2 V_0$. If we substitute these expressions in equation C.6, then the following expression is found:

$$\frac{\omega - \omega_0}{\omega_0} = \frac{\Delta W_m - \Delta W_e}{W_m + W_e}. \tag{C.7}$$

D

Measured Resonances and Quality Factors

This chapter contains the results of the S_{21} VNA scan of LT379 chip 5. We have a yield of 22/25 KIDs. Figure D.1 shows the measured and designed resonance frequencies. We see that all the KIDs are shifted downwards. We attribute this shift to the absence of the backshort, which was included in the simulations and is expected to increase the resonance frequencies. Figure D.2 shows the measured and designed quality factors. All the quality factors are lower than expected. Especially, the internal Q_i's are very low in the order of 10^3 instead of the expected $10^5 - 10^6$. We do not know the possible cause of this as there is no visible damage on the chip. We think that it has something to do with lens mounting, as another identical measured chip showed Q_i's in the expected order of $10^5 - 10^6$.

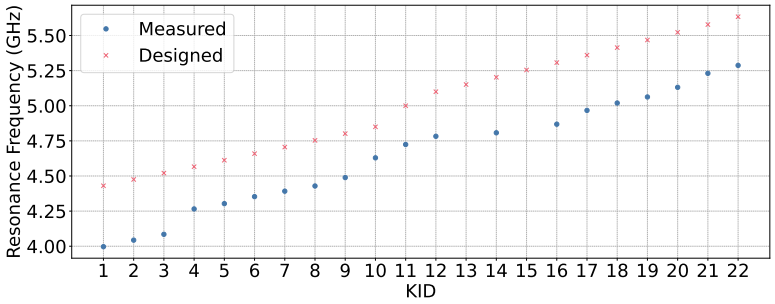

Figure D.1: The measured and designed resonance frequencies of all KIDs of chip 5 of LT379. We see that all are shifted downwards. We attribute this to the absence of the backshort, which was considered in the simulations and is expected to increase the resonance frequency.

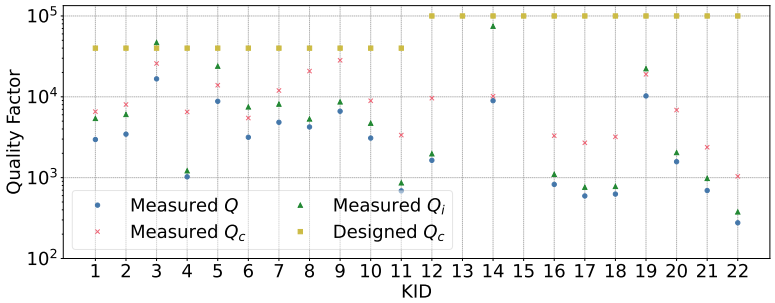

Figure D.2: The measured and designed quality factors of all KIDs of chip 5 of LT379. All the Q_i are lower than expected. We expect that this is due to the lens mounting, as we measured another identical chip without a lens array, and this chip showed the expected Q_i's of the order $10^5 - 10^6$.

E

Fitted Cross PSDs

This chapter contains the cross PSDs of one KID for each measured chip. The cross PSD of LT379 chip 5 KID 4 is shown in figure E.1 and the cross PSD of LT321 chip 8 KID 2 is shown in figure E.2.

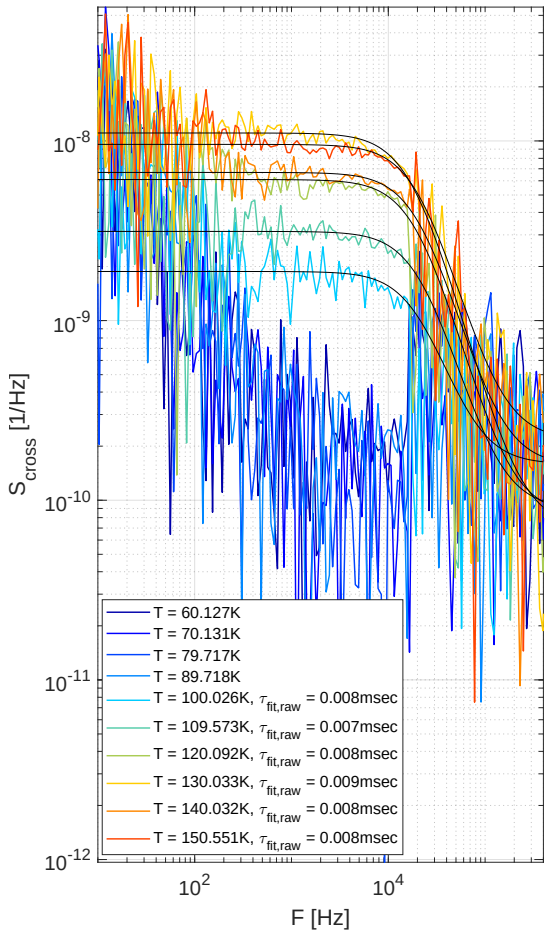

Figure E.1: The cross PSD of KID 19 of LT379 chip 5, made on a substrate. This KID is measured with a readout power of -104 dBm. We can see for T > 100K photon noise. We can recognize this by the white spectrum and the roll-off due to the recombination time. We do not see photon noise for the lower blackbody powers. We also see 1/f noise for lower frequencies. This is TLS noise.

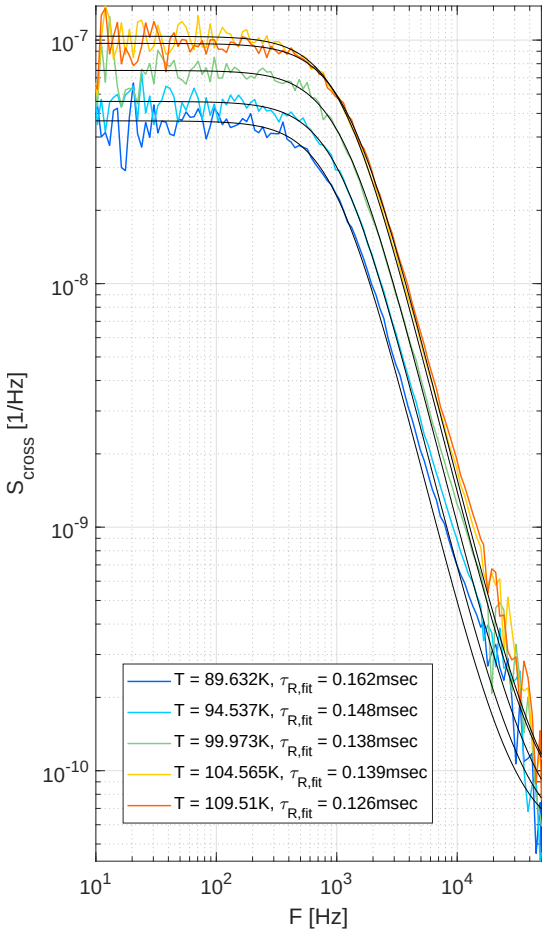

Figure E.2: The cross PSD of KID 2 of chip 8 of LT321, the chip made on a membrane. This KID is measured with a readout power of -99 dBm. Here, we see a white spectrum followed by a roll-off due to the recombination time, thus photon noise for all blackbody powers.

F

Mid-infrared substrate and lens materials

This Appendix contains a literature study of materials for the substrate and lenses of KIDs. This chapter starts with an overview of materials used in the designs of lens-absorber coupled KIDs with a similar frequency and the problems with these materials. After this, new possible materials are discussed with their respective pro's and cons. The chapter ends with a short conclusion on the materials that should be researched further.

F.1. Material requirements

Almost all astronomical sources are very faint. Therefore, one wants to capture all the radiation of these sources without many losses. In the current designs, we lose around 15% power due to absorption in the lens and substrate. This results in one of the requirements for materials for lenses and substrates having an absorption coefficient that is as low as possible.

The material needs to be mechanically strong as well, especially for the substrate of the KIDs. Another requirement can be found in thermal expansion. If the materials have a thermal expansion coefficient that differs a lot from either each other or the holder, then there will be a high risk of breaking during cooling.

The main difference in requirements between both the substrate and the lens can be found in machining. A lens needs to be made to a certain shape to focus the radiation. Therefore, the material of the lens needs to be machinable or easy to shape during fabrication. This requirement does not apply to substrates as this is a slab.

Lenses typically have an anti-reflection coating on their surface. Without an anti-reflection coating there would be a large mismatch in refractive index (or equivalently impedance) between the lens and free space. This would result in the reflection of a large portion of the incoming radiation. The anti-reflection coating needs to have a refractive index as close to $\sqrt{n_{\text{lens}} n_0}$ as possible to minimize reflections [68]. This is an additional requirement for anti-reflection coating. The other requirements are the same as for a lens except for machining in some cases.

F.2. Materials currently used

This section contains a small overview of the material used for the substrate, lenses, and anti-reflection coatings of absorber KID designs for nearby frequencies.

F.2.1. Silicon

At SRON, we typically use silicon (Si) for both the lens and the substrate due to its mechanical strength, low thermal expansion, and high refractive index [69]. However, there is one big problem with Si for the mid-IR wavelengths and that is the absorption in the material.

For this thesis, the absorption of mid-IR radiation was calculated using measurement data for high-purity Si from [70]. [70] contains the measurement of the imaginary part of the refractive index κ, from which the absorption can be calculated:

$$\frac{P_{out}}{P_{in}} = 1 - e^{-4\kappa\pi\tilde{\nu}d}. \tag{F.1}$$

Here κ is the imaginary part of the refractive index, $\tilde{\nu}$ is the wavenumber and d is the thickness of the material. The absorption was calculated for the thicknesses of a recently developed SRON lens (1.07mm) and MKID substrate ($350\,\mu\mathrm{m}$). The result is shown in figure F.1. In the figure, it can be seen that especially the absorption peak at $16\,\mu\mathrm{m}$ is problematic. There is no data available for $\lambda < 10\,\mu\mathrm{m}$.

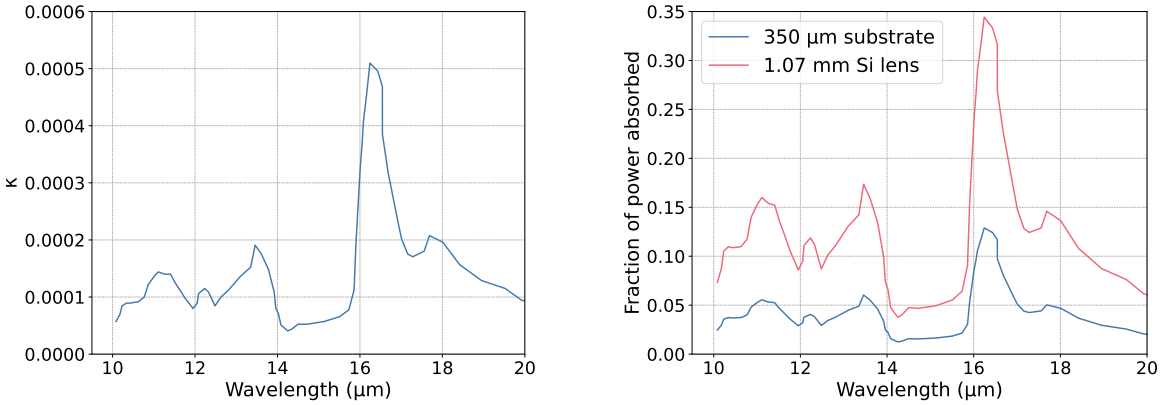

Figure F.1: The imaginary part of the refractive index of Si at 10 K with a resistivity of $30 - 40\ \mathrm{k\Omega cm}$ with the respective absorption in a lens and substrate. This data does not cover the whole wavelength range of the LIFE mission. **Left:** The imaginary part of the refractive index K [70].**Right:** The absorption for radiation for a lens with $d = 1.07$ mm and substrate with $d = 0.35$ mm.

One important notion is that the quality of the Si in Wollack et al. is better than the quality of the lenses used by SRON. The usual measurement for the quality of a dielectric is the resistivity ρ [Ω m]. A higher resistivity means fewer impurities in the dielectric and, thus, higher quality.

Previous lenses of SRON were made with Si with $\rho = 10 - 20\ \mathrm{k\Omega cm}$. The research of Wollack et al. [70] used Si with a resistivity ρ of $30 - 40\ \mathrm{k\Omega cm}$. However, for the wavelengths of our interest we do not expect that the absorption depends on the resistivity as phonons are the origin of all absorption peaks. The causes of absorption in high-purity Si found by Wollack et al. are shown in figure F.2. The figure shows that all the important absorption peaks within the infrared are caused by phonons except for 2 peaks. This is backed by the data from the industrial high-purity Si manufacturer Topsil. Their measurements of the transmission of high-purity Si and low(er) purity Si are shown in figure F.3. Only a few absorption peaks can be removed by using higher purity Si, with the most prominent one being at circa $9 - 9.5\mu\mathrm{m}$. This shows that phonons are indeed the dominant absorption mechanism.

F.2.2. Parylene C

A material used as a quarter wavelength anti-reflection coating in the visible domain and for higher wavelength ($200\,\mu\mathrm{m}$-1mm) is Parylene C. It has a refractive index of circa 1.6 [72] and is thus a good match between free space ($n = 1$) and Si ($n \approx 3.41$). However, for our current application, it has two downsides. The first one is the large absorption in our wavelength range. This is calculated using data from Li et al. [73]. This data contains measurements of the permittivity ϵ. Using the following relation: $\kappa = \frac{1}{\sqrt{2}} \cdot \sqrt{\sqrt{\Re(\epsilon)^2 + \Im(\epsilon)^2} - \Re(\epsilon)}$ [74] and equation F.1, the absortion in Parylene C can be calculated. The resulting absorption is shown in figure F.4.

The second disadvantage is the thermal expansion coefficient [72] of Parylene C, which differs from Si. The mechanical stress that can be built up due to the different changes in dimensions can break the Si lens.

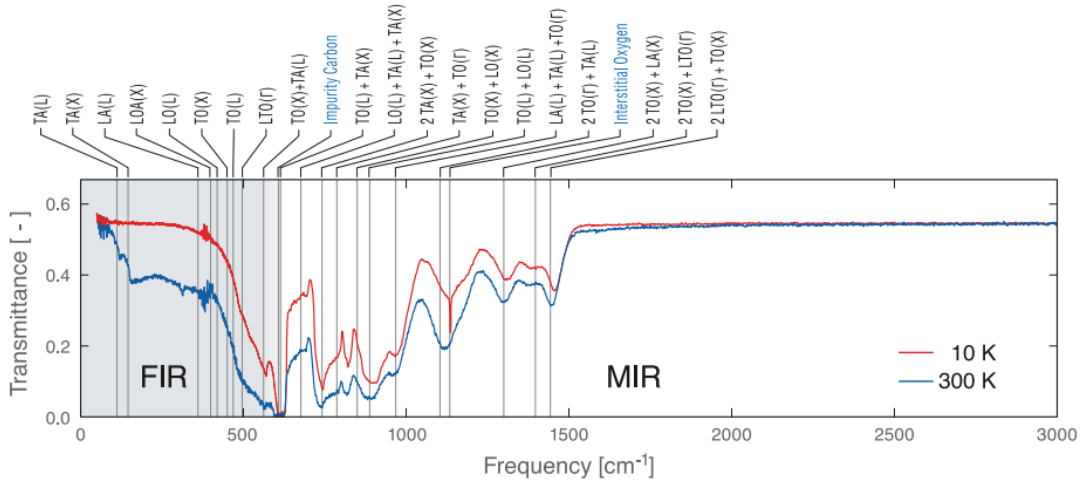

Figure F.2: The transmission of high-purity Si ($\rho = 30 - 40k\Omega cm$) slab of circa 10 mm measured in a Fourier spectrometer. The measurements are performed for 2 temperatures: 10K and 300K. The absorption sources are shown in the top of the figure. Almost absorption peaks are caused by phonons. Figure adapted from Wollack et al. [70].

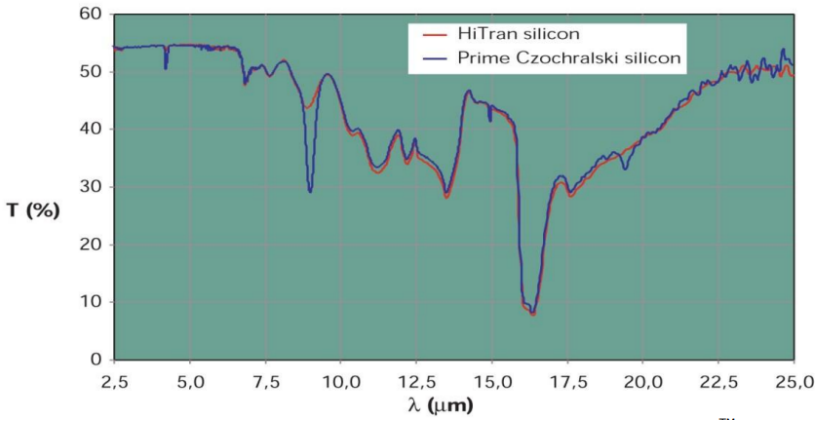

Figure F.3: Transmission from Topsil for (high purity) 2.2 mm polished HiTran^{TM} Si and (lower purity) 2.0 mm polished prime Czochralski Si. Both materials are uncoated. Oxygen concentrations for prime Czochralski Si and HiTran^{TM} Si are 6×10^{17} cm^{-3} and 5×10^{15} cm^{-3}, respectively. Figure is adapted from Topsil [71].

F.2.3. Frusta layer

Another option for anti-reflection coating is the frusta layer [75]. Technically, it is not a material but a technique. It can be seen as an impedance-matching layer between the lens and free space. Frusta layers consist of pyramid-like structures on top of the lens made from the same substrate. To create this, the lens is manufactured thicker than needed. This extra thickness corresponds to the height of the Frusta layer. Then, using laser ablation, the pyramids are created. As a result, there is no 'hard' interface between free space in the lens. We thus have a gradually changing impedance from the characteristic free space impedance to the characteristic impedance of the lens, resulting in low reflection and high transmission. An example is shown in figure F.5 [75].

Frusta layers have shown to be efficient for Si in the THz range [75]. An advantage is Frusta layers have a relatively large bandwidth compared to $\lambda/4$ anti-reflection coatings [75]. There are also no problems with thermal expansion as it is made from the same substrate as the lens. The major disadvantage is the relative complexity, both in terms of design and simulation, compared to $\lambda/4$ anti-reflection coatings. This technique is currently limited by the maximum size of the laser, which is a few micron, which corresponds to Frusta layers for a few THz [75].

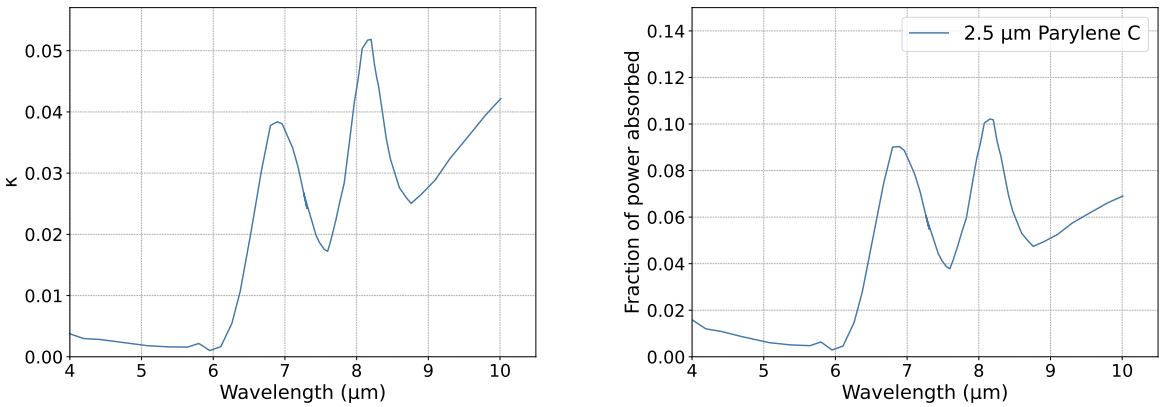

Figure F.4: The imaginary part of the refractive index κ of parylene C at 273 K ρ with the respective absorption in a lens and substrate. This data does not cover the whole wavelength range of the LIFE mission. **Left:** The imaginary part of the refractive index K [73].**Right:** The absorption for radiation for quarter wavelength anti-reflection coating for $\lambda = 10\,\mu\mathrm{m}$.

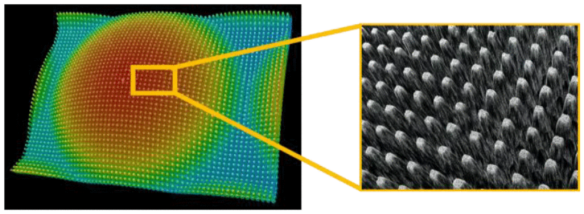

Figure F.5: A Frusta layer made for a Si lens by the Terahertz Sensing group [75]. The Frusta layer is made in the same substrate as the Si lens with a laser ablation technique.

F.3. New materials for mid-IR

In this section, new potential materials will be discussed. These materials are commercially available as lenses or windows. Some materials have disadvantages that make them impractical. Examples are salts, such as Sodium Chloride and Potassium Bromide. These salts are are hygroscopic. Therefore, one must choose an AR coating that protects the salts from water [76] [77]. Another option that is often used for windows is Zinc Selenide or the very similar Zinc Sulfide, which is used in the James Webb Space Telescope (JWST) [78]). However, both materials are toxic and scratchable [79]. This is not a problem for JWST as it is used as a window. However, we we will use it as a part of a detector that is fabricated in a cleanroom and tested in a measurement setup. This leaves us with three viable options that will be discussed: germanium and two forms of synthetic diamond.

Germanium

One of the industrially available options is Germanium (Ge). It is used between 2-16 µm with very high transmission (almost 100 % with AR coating) [80]. It is thus only feasible for part of the wavelengths of LIFE. It is chemically non-reactive, non-hygroscopic, and mechanically strong [81]. Ge has a high refractive index of 4 [82]. It is the material used in the mid-IR instrument of the JWST [78].

Ge has two disadvantages. Firstly, there is a shortage of Ge at the time of writing, resulting in high delivery times and prices. Secondly, it has a high relative change of the refractive index as a function of temperature: $\frac{dn}{dT} = 3.96 \cdot 10^{-4}\mathrm{K}^{-1}$ [69], which should not be a problem if the temperature is stable and the correct refractive index for that temperature is used.

Synthetic diamond

Another material that can be used as a lens is polycrystalline CVD diamond. The material is a diamond and, therefore, mechanically strong with a high thermal conductivity [83]. It has a refractive index between 1.95 [84] -2.38 [85]. It has a high transmission between 8 µm and 25 µm with an absorption coefficient of 0.07 cm^{-1} at $10.6\,\mu\mathrm{m}$.

One disadvantage is the machining of the material. Currently, almost no commercial companies makes

diamond microlens arrays. However, it is commercially available in the form of quarter wavelength anti-reflection coatings for Si and Ge lenses [86], reaching almost 100 $\%$ transmission. Another disadvantage can be found in the high price of diamonds.

F.4. Proposed materials for LIFE

The wavelength range of LIFE is relatively large. As a result, it is not possible to make an optical system that can function efficiently for the whole band. Therefore,the wavelength range will be split into different wavelength bands. Each wavelength band will have its own optical system and detector array. This is also advantageous for the KIDs, allowing us to use different materials for the different wavelength bands.

The final decision on the wavelength bands was not made at the time of writing. Internal discussions discussed 3-4 wavelength bands, which is assumed in this thesis. The material choice for the substrate and lenses for the KIDs on the LIFE mission will presumably be this or similar:

- 4-7 $\mu\mathrm{m}$: Si with diamond quarter wavelength coating.
- 7-13 $\mu\mathrm{m}$: Ge with diamond quarter wavelength coating.
- 13-18.5 $\mu\mathrm{m}$: Diamond with a quarter wavelength coating.

From these materials, Si has been used by the group extensively. Therefore, the material properties are already known. Ge and diamond had not been used by the group before. From literature studies, we can understand the optical properties, but more research needs to be done. This can be done with Fourier transform spectroscopy.